BEYOND CONVENTIONAL DFT CATALYSIS: MECHANOCHEMISTRY AND SOLID REDUCTANTS

Bruna Sánchez Pladevall

UNIVERSITAT
ROVIRA i VIRGILI

Beyond conventional DFT catalysis: Mechanochemistry and solid reductants

---

BRUNA SÁNCHEZ PLADEVALL

DOCTORAL THESIS

2021

Bruna Sánchez Pladevall

Beyond conventional DFT catalysis: Mechanochemistry and solid reductants

DOCTORAL THESIS

Supervised by Prof. Feliu Maseras Cuní

Institute of Chemical Research of Catalonia

ICIQ Institut Català d'Investigació Química

UNIVERSITAT ROVIRA i VIRGILI

Tarragona 2021

ICIQ - Institut Català d'Investigació Química

Avgda, Països Catalans 16,

43007 Tarragona (Spain)

Prof. Feliu Maseras Cuní, Group Leader at the Institute of Chemical Research of Catalonia,

I STATE that the present study, entitled " Beyond conventional DFT homogeneous catalysis: Mechanochemistry and solid reductants " presented by Bruna Sánchez Pladevall for the award of the degree of Doctor, has been carried out under my supervision in my group at the Institute of Chemical Research of Catalonia and that it fulfills all the requirements to be eligible for the International Doctor Distinction.

Tarragona, August 31st, 2021

Doctoral Thesis Supervisor

Prof. Feliu Maseras Cuní

Acknowledgments

I want to thank my supervisor, Prof. Feliu Maseras for giving me the opportunity to carry out the PhD in his group and also his support and advice during these years. I would also like to thank the group membres. Finally I would like to thank my mother, the only way I got here today is her constant support, love and understanding.

Finally, I would like to thank the financial supporters involved in the development of the presented work:

ICIQ Institut Català d'Investigació Química

GOBIERNO DE ESPAÑA MINISTERIO DE CIENCIA E INNOVACIÓN

Generalitat de Catalunya
Departament d'Innovació, Universitats i Empresa

List of publications

"Understanding Ball Milling Mechanochemical Processes with DFT Calculations and Microkinetic Modeling"

Pladevall, B.S.; de Aguirre, A.; Maseras, F.; Martín, M. *ChemSusChem* **2021**, 14, 2763-2768.

Table of Contents

Abstract

Computational chemistry has been established as a crucial tool for the understanding of chemical reactivity and is driving catalysis towards a more rational design approach. The constant development and the increasing sophistication of experiments has raised numerous challenges for the computational chemists, who seek methods to deal with such complex transformations. In this context, systems located on the frontier of homogeneous and heterogeneous worlds are gaining importance, as they permit the combination of the best features of each area. From a theoretical perspective, homogeneous and heterogeneous reactions are modelled through substantially different approaches. There is thus an increasing need to investigate the most suitable manner to model these types of systems.

We focused our attention on the application of homogeneous methods to the exploration of mechanochemistry and reactions involving the use of solid reductants. In the course of this thesis, the reader will be driven through a general introduction and a theoretical background followed by three main research chapters and a general conclusion section. Herein we will briefly summarise the content of each section in the manuscript.

The *General Introduction* provides insights on the differences and similitudes between homogeneous and heterogeneous reactions as well as the systems located in the frontier of the two disciplines.

The *Theoretical Background* describes the less-common computational methodologies that have been applied to model the different systems under study. Techniques employed for the calculation of Standard Reduction Potentials (SRP) or the construction of volcano plots are addressed among others.

Chapter I is centred on the development of a computational approach for the rationalisation of ball milling mechanochemical processes. Different hypotheses are examined through the study of three simple organic reactions which serve as validation for the proposed strategies. The combination of standard DFT tools together with microkinetic models proved to be crucial for the proper modelling of these systems because they permit the incorporation of the mechanochemical medium and concentrations.

Chapter II provides a full mechanistic picture of a nickel-catalyzed reductive cross coupling of aryl halides with monofluoroalkyl halides. The mechanistic investigation is performed in an iterative manner, combining energy profiles with microkinetic models. This strategy enables to discard the conventional reductive coupling mechanism and supports an alternative substrate radical trapping path, without metal participation in the carbon-carbon formation step.

Chapter III reveals the full energy profile for a cross-coupling reaction under reductive conditions. The solid reductant is explicitly incorporated in the mechanism and happens to play a key role in multiple reaction steps, from the ligand exchange to the transmetalation, clarifying the individual properties that make this metal a great fit for this transformation.

Finally, the thesis finishes with the *General Conclusions*, which outline the main results of each chapter and provide a more general summary of the learnings gained through this research effort.

General Introduction

Catalysis is a steadily growing field which is crucial to address emerging requirements from society. The importance of catalysis is not new, as the "Haber-Bosch" process for ammonia production revolutionized the agriculture in the early 1900s,[1] but it has increased throughout the years with achievements such as a higher conversion rate from crude oil to fuel or better-quality bulk and fine chemical products at lower cost (Figure 1). [2] Indeed, nowadays more than 90% of chemicals produced are manufactured with the aid of catalytic processes.[3]

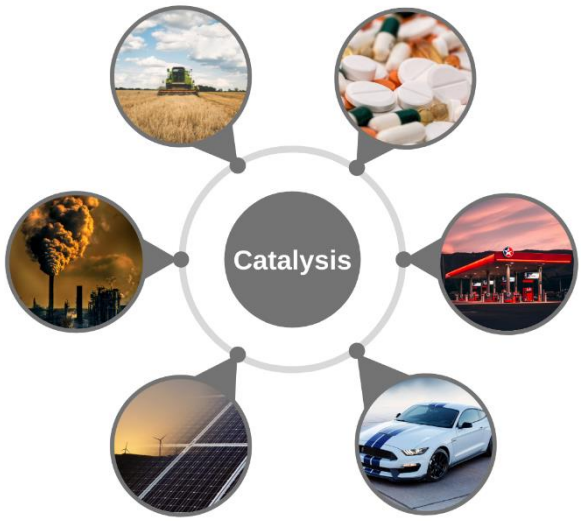

Figure 1. Examples of applications of catalysis.

Despite the undisputable success and impact on society of catalysis, there is still margin for improvement. The underlying multidisciplinary nature of

1 Humphreys, J.; Lan, R.; Tao, S. Adv. Energy Sust. Res., **2021**, 2(1), 2000043.

2 Moulijn, J. A.; van Leeuwen, P.W.N.M.; van Santen, R. A. (Eds.). (**1993**). Catalysis: An Integrated Approach to Homogeneous, Heterogeneous and Industrial Catalysis. Elsevier Science Publishers B.V.

3 Sci, C.; Vries, J. G. De; Jackson, S. D. Catal. Sci. Technol., **2012**, 2, 2009.

catalysis is a limitation for the further advancement of the field. For example, homogeneous and heterogeneous catalysis, which are the two sides of the same coin, have been developed independently for years. Whereas homogeneous catalysis is mostly studied by the organic chemistry community, heterogeneous catalysis has been investigated mostly through chemical engineering and physical chemistry.[4]

Table 1 shows some of the most important features that differentiate homogeneous and heterogeneous catalysis. On one hand, the easy and cheap recovery, high thermal stability, and high activity makes heterogeneous catalysts highly advantageous for large scale industrial processes. However, it reaches its highest efficiency when applied to the synthesis of rather simple molecules, such as ethanol or ammonia, and is not appropriate for the synthesis of complex molecules such as those used in the pharmaceutical industry because of the harsh conditions usually involved. In contrast, homogeneous catalysis is especially appropriate for fine synthesis, as it can promote high selective transformations and enable access to highly complex molecules. Homogeneous catalysis otherwise struggles for large scale applications due to limited thermal stability and the expensive catalyst recovery processes.[5]

Overall, homogeneous and heterogeneous catalysis are complementary disciplines: the weak points of homogeneous catalysis are the strong points of heterogeneous catalysis and *vice versa*. Thus, the combination of their characteristics would create a perfect synergia achieving the ideal catalyst: cheap, stable, active, selective and with access to high molecular complexity.

4 Can, L.; Yan, L. (Eds.). (**2014**). *Bridging Heterogeneous and Homogeneous Catalysis: Concepts, Strategies, and Applications*. Wiley-VCH Verlag GmbH & Co. KGaA.

5 Farnetti, E.; Monte, R. Di; Kašpar, J. (**1999**). *Inorganic and Bio-Inorganic Chemistry (Vol. II, Homogeneous and Heterogeneous Catalysis)*. Encyclopedia of Life Support Systems (EOLSS).

Table 1. Comparison of the advantages and disadvantages of homo and heterogeneous catalysis.

Property	Homogeneous catalysis	Heterogeneous catalysis
Catalyst recovery	Difficult and expensive	Easy and cheap
Thermal stability	Poor	Good
Activity	Moderate	High
Selectivity	Relatively easy	Relatively difficult
Molecular complexity	High	Low
Catalyst modification	Easy	Difficult

Research on heterogeneous systems started decades before the study of homogeneous catalysed reactions. However, even with this chronological disadvantage, homogeneous reactions are by far better understood. In fact, they often present a shorter time span between the development of novel catalytic systems and the rationalisation of their reaction mechanisms.[6] This is largely due to the presence of highly effective methods (in particular spectroscopic) to detect intermediates which combined with the simplicity and reproducibility of homogeneous systems,[7] leads to a "facile" elucidation of their reaction mechanisms. Although the extraction of detailed mechanistic information is easier in homogeneous systems, there are still several issues that need to be addressed such as the detection of subproducts as well as the characterisation of short-lived species and side reactions.[8]

6 Luberoff, B. J. (**1974**). *Homogeneous Catalysis*. Americal Chemical Society.

7 Di Cicco A.; Giuli G., Trapananti A. (Eds.). *Synchrotron Radiation Science and Applications.* (**2021**). Springer Proceedings in Physics, vol 220. Springer, Cham.

8 (a) Gascon, J.; Aktay, U.; Hernández-Alonso, M. D.; van Klink, G. P. M.; Kapteijn, F. *J. Catal.* **2009**, 261(b) Stephen, A.; Hashmi, K. *Angew. Chem., Int. Ed.* **2010**, 49 (31), 5232−5241. (c) Blackburn, J.M.; Roizen, J.L. *Science*, **2018**, 362 (6411), 157-158. (d) de Salinas, S.M.; Sanjosé-Orduna, J.; Odena, C.; Barranco, S.; Benet-Buchholz, J.; Pérez-Temprano, M.H. Angew. Chem. Int. Ed. **2020**, 59(15), 6239-6243.

The obtention of detailed mechanistic understanding of catalytic systems is central to draw trends and predict reactivity, which allows the development of new catalysts following a "rational design" strategy.[9] In this regard, computational chemistry can assist the characterisation of atomic structures as well as the elucidation of reaction mechanisms, providing a cheap and easy methodology to aid the catalyst design (Scheme 1).[10]

Although computational modelling exhibits an enormous potential to critically influence the catalysis community by assisting the rational design and speeding up the catalyst discovery, its impact significantly depends on the accuracy of the predictions. In both homogeneous and heterogeneous communities, density functional theory (DFT) has been established as the standard method for the simulation of catalytic systems, as it often provides the best compromise between accuracy and computational cost.[11]

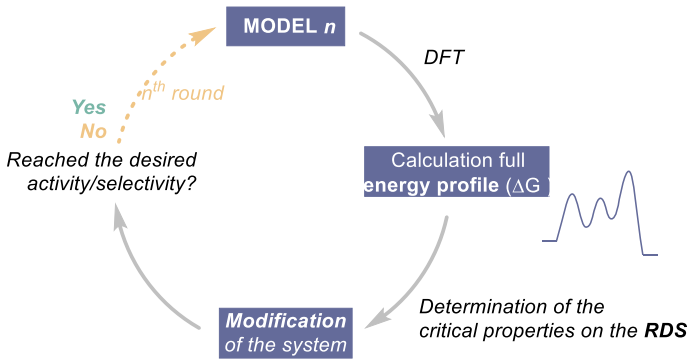

Scheme 1. Workflow for the rational design of new catalysts by applying modifications to the actual system.

9 (a) Baiker, A. *J. Mol. Catal. A: Chem*. **2000**, 163 (1−2), 205−220. (b) Nørskov, J. K.; Bligaard, T.; Rossmeisl, J.; Christensen, C. H. *Nat. Chem.* **2009**, 1 (1), 37−46. (c) Costentin, C.; Robert, M.; Savéant, J. M. *Acc. Chem. Res*. **2015**, 48 (12), 2996−3006. (d) Funes-Ardoiz, I.; Schoenebeck, F. *Chem*. **2020**, 6(8), 1845-2124.

10 Falivene, L.; Kozlov, S. M.; Cavallo, L. *ACS Catal*., **2018**, 8, 5637−5656.

11 Qi, S.C.; Hayashi, J.I; Zhang, L. ***RSC Adv*. 2016, 6,** 77375-77395.

The computational modelling of homogeneous and heterogeneous systems is fundamentally different, and the reactivity is rationalized analysing completely different properties. Whereas in homogeneous catalysis the methods are designed for the study of steric[12] and electronic factors[13] of the ligand as well as the analysis of frontier orbitals (HOMO/LUMO);[14] in heterogeneous systems the key concepts are the band gap[15] or the binding strength.[16] Owing to the inherent differences on the properties studied and the nature of the transformations, the methods employed to simulate the catalytic cycles differ between homogeneous and heterogeneous systems.

In homogeneous catalysis the reaction is studied between isolated molecules (unique active site), with the electron density described through localized basis functions centred at the atomic nuclei, these functions being either gaussians or Slater-type orbitals. In heterogeneous catalysis, the surface reaction (multiple active sites) requires often the implementation of periodic boundary conditions, and the electron density is described by planar waves. Despite the difference between the methodologies, the challenges they face are somehow comparable. We discuss below what we consider the six main issues on static calculations for homogeneous[17] and heterogeneous[18] catalysis: (i) electronic structure

12 Tolman, C. A. *Chem. Rev*. **1977**, 77 (3), 313−348.

13 Clarke, M.L.; Frew, J.J.R. (2009) In Organometallic Chemistry Vol. 35. The Royal Society of Chemistry. pp.19–46.

14 Fukui, K.; Yonezawa, T.; Shingu, H. A. *J. Chem. Phys*. **1952**, 20, 722− 725.

15 (a)Newns, D. M. *Phys. Rev*. **1969**, 178 (3), 1123−1135. (b) Bligaard, T.; Nørskov, J. K. *Electrochim. Acta* **2007**, 52 (18), 5512−5516.

16 (a) Abild-Pedersen, F.; Greeley, J.; Studt, F.; Rossmeisl, J.; Munter, T. R.; Moses, P. G.; Skúlason, E.; Bligaard, T.; Nørskov, J. K. *Phys. Rev. Lett.* **2007**, 99, 16105. (b) Montemore, M. M.; Medlin, J. W. *Catal. Sci. Technol*. **2014**, 4, 3748−3761.

17 Harvey, J.N.; Himo, F.; Maseras, F.; Perrin, L. *ACS Catal*., **2019**, 9, 6803-6813.

18 López, N.; Almora-Barrios, N.; Carchini, G.; Piotr, B.; Bellarosa, L.; Garcia-Muelas, R.; Novell-Leruth, G.; García-Mota, M. *Catal. Sci. Technol*., **2012**, 2, 2405–2417.

method, (ii) microkinetic studies, (iii) conformational complexity, (iv) structural model, (v) selectivity, and (vi) solvation effects.

(i) Electronic structure method

The area of electronic structure methods has experienced an enormous progress over the past decades. The theory has evolved from Hartree-Fock-based methods, where one has to compute the wave function, which depends of 3N dimensions (N being the number of electrons); to Density Functional Theory (DFT), where one has to compute only the toal density, depending on 3 dimensions (Equation 1). DFT has a more efficient scaling of the computational cost with respect to the size of the system, which makes it the method of choice for most practical applications, even if its application to small systems requiring high accuracy is still disputed.

$$E_{DFT} = F[\rho(x, y, z)] \quad (1)$$

The functional F consists of different parts, involving kinetic energy, nucleus-electron repulsion and electron-electron repulsion. The key complexity is in the electron—electron part, specifically in the exchange-correlation term. This term is often divided into two parts ($E_c[\rho]$ and $E_{xc}[\rho]$); the specific expression for this functional constitutes the great challenge of DFT approaches.[19] Over the last decades, significant improvements have been done on different approaches to solve them, achieving major developments going from the "Hartree world" towards the "Chemical accuracy" as exemplified in the Jacob's ladder proposed by Perdew some years ago (Figure 2).[20]

19 Sholl, D.S.; Steckel, J.A. (2009). *Density Functional Theory: A Practical Introduction*. Wiley-VCH Verlag GmbH & Co. KGaA.

20 Perdew J.P.; Schmidt, K. *AIP Conf. Proc.*, **2001**, 577, 1.

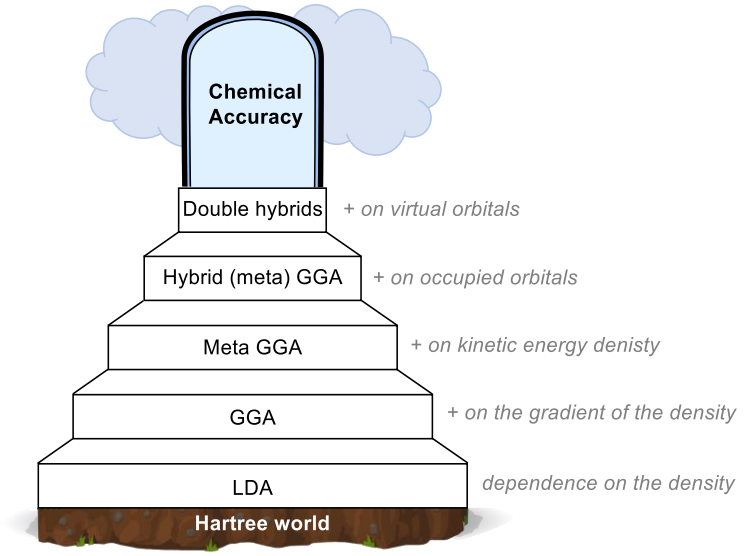

Figure 2. Representation of the Jacob's Ladder; path from the "Hartree world" towards the "chemical accuracy" through the development of more accurate exchange correlation density functional.

The selection of method is decisive to obtain reliable results and needs to present a good compromise between the accuracy and the computational effort.[21] In the last two decades, it has been recognized that previous functionals presented a significant shortcoming in the poor description of van der Waals (vdW) interactions.[22] The proper description of vdW terms gains importance upon increasing the size of the systems. An elegant solution has been found with the introduction of Grimme dispersion.

21 Schwabe, T.; Grimme, S. *Acc. Chem. Res.* **2008**, 41(4), 569-579.

22 (a) Jones, R.O. *Rev. Mod. Phys.* **2015**, 87, 897–923. (b) Cohen, A.J.; Mori-Sánchez, P.; Yang, W. *Chem. Rev.* **2021**, 112, 289–320.

Another intrinsic problem of pure DFT methods is the self-interaction error (SIE).[23] This error arises due to the nature of the E_{xc} term, which implies a non-zero interaction between the electron and its own density, which is an artifact. The introduction of a part of Hartree-Fock exchange (hybrid functionals) helps reduce this error.

It is worth mentioning that the last rungs of the ladder, corresponding to the double hybrid also called non-local functionals are still far to be fully optimised and do not represent the current common choice.[24] Instead, more recent developments seem to focus on high parameterizations (M06 family) and range-separated functionals.

(ii) Kinetic studies

The implementation of kinetic studies is highly desirable for both homogeneous[25] and heterogeneous[26] systems because it allows a more detailed description of the reaction conditions providing a simpler link between theory and experiments. However, the application of microkinetic models in both disciplines suffer from accuracy problems. This is because minor changes on the energetic profile arising upon the use of approximate methods for the calculation of reaction energies result into drastic changes on the rate constant of a reaction (Scheme 2)**¡Error! No se encuentra el origen de la referencia.**. Thus, the level of accuracy gains importance upon the application of microkinetic models.

23 Bao, Gagliardi, Truhlar*J. Phys. Chem. Lett*.**2018**, *9*, 2353. (b) Sharkas, K.; Wagle, K.; Santra, B.; Akter, S.; Zope, R.R.; Baruah, T.; Jackson, K.A.; Perdew, J.P.; Peralta, J.E. *PNAS*, **2021**, 117(21), 11283-11288.

24 Martin, J.M.L; Santra, G. *Isr. J. Chem*. **2020**, 60, 1-19.

25 Besora, M.; Maseras, F. Microkinetic Modeling in Homogeneous Catalysis. *WIREs Comput. Mol. Sci*. **2018**, 8, e1372.

26 Sabbe, M.K.; Reyniers M.F.; Reuter, K. *Catal. Sci. Technol*., **2012**, 2(10), 2010-2024.

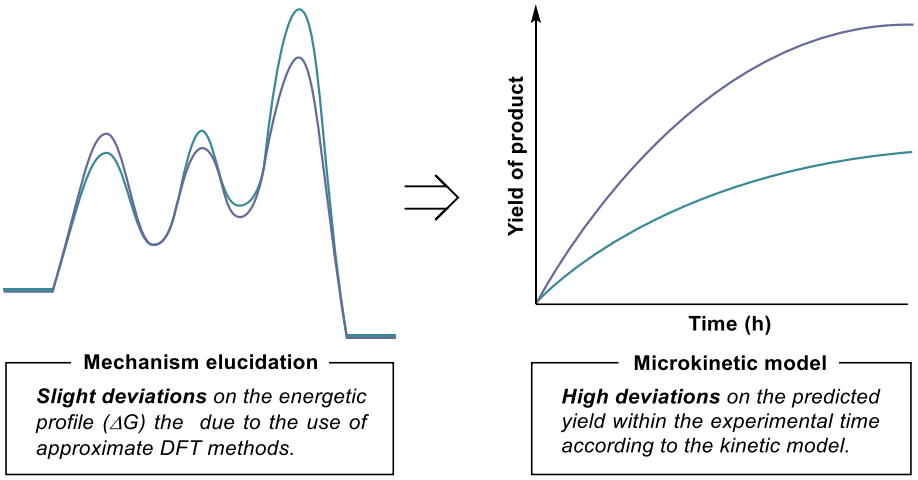

Scheme 2. Effect of slight deviations on the activation energies when they are translated into microkinetic models.

(iii) Conformational complexity

The conformational complexity issues are predominant in homogeneous catalysis. The common use of bulky ligands to achieve effective and selective transformations implies a high conformational flexibility and the error bar associated with the conformer choice can be significantly large leading to misleading results. For example, Munkerup *et al*., performed a case study on pincer ligands containing phosphine groups, and found deviations up to 8.6 kcal/mol between the global minimum and the higher local minimum on the metal complexes investigated (Scheme 3).[27] The conformational search can be very tedious and time-consuming, in particular with big systems i.e., the amount of conformers increase exponentially with the number of atoms. The need to investigate all the conformational space, leads to highly complex studies even on simple mechanisms. Besides, in some cases is extremely

27 Munkerup, K.; Thulin, M.; Tan, D.; Lim, X.; Lee, R.; Huang, K. *J. Saudi Chem. Soc.* **2019**, 23(8), 1206–1218.

difficult to confirm that the lowest energy conformer found is the global minimum hampering the reliability on the results.

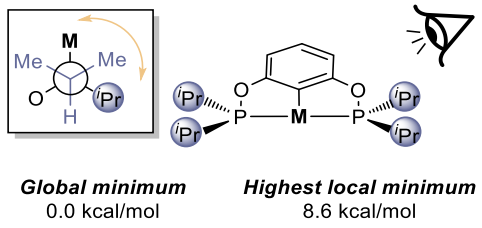

Scheme 3. Representation of two potential error sources in the choice of the microscopic model in homogeneous catalysis.

In heterogeneous catalysis, problems arising from conformational complexity have increased over the last decades due to the introduction of more complex molecules with more than one functional group. In these situations, there are multiple adsorption configurations that have to be investigated, and of course, this variability opens up a higher number of plausible reaction paths, forcing the conductance of a conformational search.[28] Still, the problems related to conformational analysis in heterogeneous catalysis are substantially minor in comparison to homogeneous catalysis.

(iv) Structural model

Another crucial effect appears upon the selection of the structural model of the real system. In homogeneous catalysis this includes both the simplification of the ligand to reduce computational cost and the treatment of small ions that are gained/lost by the system (Scheme 4). For example, there is a big discussion on the proper modelling of a mechanism involving the uptake of a proton. The

28 Torres, D.; Lopez, N.; Illas F.; Lambert, R.M. *Angew. Chem., Int. Ed.*, **2007**, 46, 2055–2058.

system could be reproduced following any of the equations shown in Scheme 4, leading to completely different results.

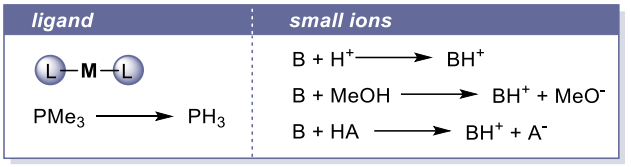

Scheme 4. Representation of two potential error sources in the choice of the microscopic model in homogeneous catalysis.

In heterogeneous catalysis, the choice of the structural model is related to the modification of cell parameters, in particular the volume and the number of surface layers.[29] The increase of both the volume of the cell or the number of layers results into a higher number of plane waves; thus, we want to find a good compromise to avoid high computational cost. First, if the cell is small, there might not be enough separation between the molecules adsorbed or between the surfaces (Scheme 5, middle) when the unit cell is replicated. When this happen there appear self-interactions within two subsequent cells, *i.e.*, the molecules or surfaces in each cell interact with themselves in the neighbouring cell, leading to unrealistic representations associated with high errors.[30] A similar situation arises if the number of surface layers is too big for the selected cell.[31] However, it is important to mention that the number of surface layers affects the properties of the material, therefore, again one must find a good compromise between accuracy and computational cost.

29 Liu, Y.; Zheng, G.; Letov, N.; Zhao, Y.F. *J. Mech. Des.* **2021**, 143(4), 040803.

30 Hammer, B.; Nørskov, J.K. *Adv. Catal.* **2000**, 45, 71-129.

31 Suchorski, Y.; Rupprechter, G. *Catal. Lett.* **2018**, 148, 2947-2956.

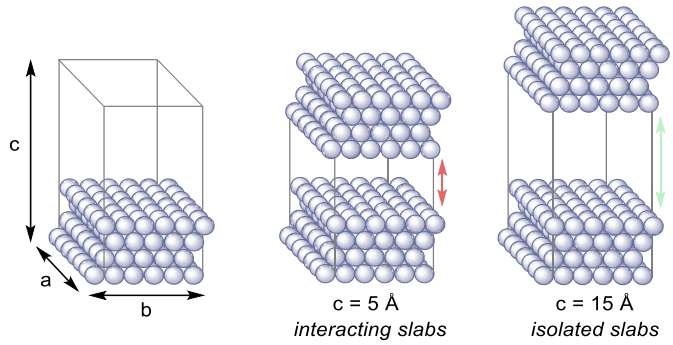

Scheme 5. Representation of the self-interactions between the surface layers due to the wrong selection of the size of the unit cell.

(v) Selectivity

The complexities on the theoretical determination of selectivity are similar for both homogeneous[32] and heterogeneous[33] systems. The energy difference on the selectivity determining step (Scheme 6) tends to be very small, thus, an error of few kcal/mol can lead to catastrophic results, *i.e.*, prediction of the opposite selectivity. If we combine this source of error with the above-mentioned conformational issues, it can result extremely difficult to do a proper characterization of this type of systems.

32 Liao, R.-Z.; Santoro, S.; Gotsev, M.; Marcelli, T.; Himo, F. *ACS Catal*. **2016**, 6, 1165−1171. (b) Menezes da Silva, V.H.; Morgon, N-H.; Correia, C.R.D.; Braga, A.A.C. *J. Org. Chem*. **2019**, 869, 5e15.

33 (a) Frei, M.S.; Mondelli, C.; García-Muelas, R.; Morales-Vidal, J.; Philipp, M.; Safonova, O.V.; López, N.; Stewart, J.A.; Ferré, D.C.; Pérez-Ramírez, J. *Nat. Commun.* **2021**, 12, 1960. (b) Roeder, G.J.; Ray, K.H.; Yang, G.; Bauer, T.J.; Haller, G.L.; Batista, V.S.; Barath, E. *ACS Catal*. **2021**, 11(9), 5405-5415.

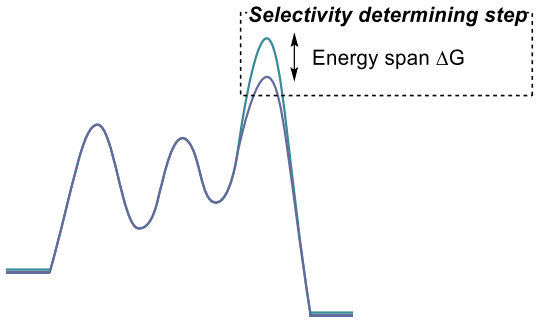

Scheme 6. Representation of the small energy difference in the selectivity determining steps.

(vi) Solvation effects.

Another parameter that induces considerable effects on both homogeneous and heterogeneous systems is the solvent.[34] Indeed, from an experimental perspective, the choice of solvent can dramatically influence the conversion or selectivity of a transformation.[35] Thus, when performing a computational analysis, it is crucial to introduce a good description of the solvation effects. In heterogeneous catalysis, the solvent is only required in those transformations involving a solid-liquid interface. The implementation of solvation effects in periodic systems has suffered a considerable growth on the last decades,[36] however, the lack of systematic studies hampers the rationalization of solvation effects.[37] Even worse, the application of solvent requires an extremely high computational cost, most of the heterogeneous studies are performed in gas phase. By contrast, the inclusion of solvent effects in homogeneous catalysis is widely spread; almost all the mechanistic investigations include either

34 Reichardt, C. (**2003**). *Solvents and Solvent Effects in Organic Chemistry*. Wiley-VCH Verlag GmbH & Co. KGaA.

35 Dyson, P.J.; Jessop, P.G. *Catal. Sci. Technol*. **2016**, 6, 3302-3316.

36 Garcia-Ratés, M.; López, N. *J. Chem. Theory Comput*. **2016**, 12, 1331−1341.

37 J. Tomasi, B. Mennucci and R. Cammi, *Chem. Rev*., **2005**, 105, 2999–3093.

implicit[38] or explicit[39] solvation (Scheme 7). Implicit methods employ a continuum model in which the solvent is represented as a cavity with determinate features.[40] Although these approximate methods perform extremely well, with errors of around 1 kcal/mol for neutral and only few kcal/mol for ionic species, there are some limitations that must be considered. These solvation treatments are parametrized to reproduce Gibbs free energies, thus the separate treatment of enthalpy values is not straightforward. More critically, these methods do not allow the participation of solvent molecules in the reaction. The natural solution is the use of explicit solvation methods, where a certain number of solvent molecules are introduced in the calculation. The explicit treatment with a large number of solvent molecules is highly appealing because it could provide an accurate description of the system at the microscopic level.[41] However, it would requires the use of molecular dynamics, with a whole new level of complexity and computational cost.

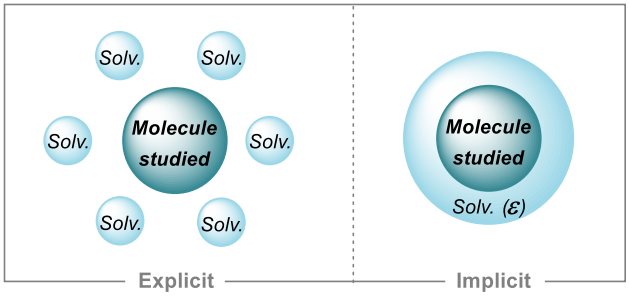

Scheme 7. Examples of factors delimiting the accuracy of DFT computations in homogeneous catalysis and heterogeneous.

38 Álvarez, M.; Besora, M.; Molina, F.; Maseras, F.; Belderrain, T.R. *J. Am. Chem. Soc*. **2021**, 143(12), 4837-4843.

39 Boereboom, J.M.; Fleurat-Lessard, P.; Bulo, R.E. *J. Chem. Theory. Comput.* **2018**, 14(4), 1841.1852.

40 J. Tomasi, B. Mennucci and R. Cammi, *Chem. Rev.*, **2005**, 105, 2999–3093.

41 Varghese, J.J.; Mushrif, S.H. *React. Chem. Eng.* **2019**, 4, 165-206.

Systems in the frontier between homogeneous and heterogeneous worlds

In principle, the differences between homogeneous and heterogeneous systems are clear. However, in real systems, these two disciplines are separated by a fine line.[42] Indeed, researchers are pushing the boundaries developing systems that account the best properties of each discipline. For example, over the last years, several studies have been performed on the anchoring of homogeneous catalysts,[43] decoration of nanoparticles with surface modifiers,[44] single atom catalysis,[45] and other novel catalytic systems such as metal organic frameworks (MOFs)[46] or covalent organic frameworks (COFs).[47]

Apart from these engineered systems, there are other types of reactions that happen to be in the frontier between both homogeneous and heterogeneous worlds. The computational modelling of these scenarios may imply the consideration of molecular and periodic features. Hence, once again, we face the drawbacks of the frontier between both disciplines.

42 (a) Corma, A. *Catal. Rev.* **2004**, 46(3) 369-417. (b) Maganas, D.; Trunsche, A.; Schlögl, R.; Neese, F. *Faraday Discuss.* **2016**, 188, 181-197.

43 (a) Cole-Hamilton, D.J. *Science* **2003**, 299(5613), 1702-1706. (b) Kisszékely, P.; Nagy, S.; Feher, Z.; Huszthy, P. *Chemistry* **2020**, *2*(3), 742-758.

44 Ortuño, M.A.; López, N. *Catal. Sci. Technol.* **2019**, 9, 5173–5185.

45 Mitchell, S.; Vorobyeva, E.; Pérez-Ramirez, J. *Angew. Chem. Int. Ed*. **2018**, 57(47), 15316 – 15329.

46 (a) Bernales, V.; Ortuño, M.A.; Truhlar, D.G.; Cramer, C.J.; Gagliardi, L. *ACS Cent. Sci.* **2018**, 4(1), 5-19. (b) McCarver, G.A.; Rajeshkumar, T.; Vogiatzis, K.D. *Coord. Chem. Rev.* **2021**, 436, 213777.

47 (a) Altaf, A.; Baig, N.; Sohail, M.; Sher, M.; Ul-Hamid, A. Altaf, M. *Mater. Today Commun.* **2021**, 28, 102612. (b) Ahmed, I.; Jhung, S.H. *Coord. Chem. Rev*. **2021**, 441, 213989.

In some cases, we face a situation in which a homogeneous-like reaction involves either a change of state *e.g.*, precipitation of a salt as driving force for a reaction,[48] or it involves, at least, one solid reagent. There is the even less defined case of mechanochemical reactions; those transformations activated by mechanical means.[49]

Mechanochemistry encompasses a wide range of processes with completely different foundations, thereby constituting an extremely interdisciplinary field. For example, any conceivable combination of two chemical states can be found in a mechanochemical transformations.[50] Herein we will only comment on those mechanochemical reactions involving at least, one solid reagent.

The presence of a solid usually comes accompanied by periodic properties that must be considered. However, the application of a mechanical force leads to a deformation of the solid which can result into the creation of defects, the complete amorphization and in some cases, the formation of pseudo-fluids.[57] Therefore, each mechanochemical system must be treated as an independent entity, to allow an individual analysis of the effect of the solid structure to the reaction outcome. Then, considering the properties under study, the type of material and the mechanochemical process used, one has to select the best

48 López-Resano, S.; de Salinas, S. M.; Garcés-Pineda, F. A.; Moneo-Corcuera, A., Galán-Mascarós, J. R.; Maseras, F.; Pérez-Temprano, M.H. *Angew. Chem. Int. Ed.* **2021**, 60, 11217-11221.

49 For a comprehensive review see: (a) James, S.L.; Adams, C.J.; Bolm, C.; Braga, D.; Collier P.; Friščić, T.; Grepioni, F.; Harris, K.D.M.; Hyett G.; Jones, W.; Krebs, A.; Mack, J.; Maini, L.; Guy Orpen, A.; Parkin, I.P.; Shearouse, W.C.; Steedk, J.W.; Waddelli, D.C. *Chem. Soc. Rev.*, **2012**, 41, 413–447. (b) Boldyreva, E. *Chem. Soc. Rev.*, **2013**,42, 7719-7738. (c) Leininger, S.E.; Narayan, K.; Deutsch, C.; O'Brien, E.P.; *Biochemistry* **2019**, 58, 4657−4666. (d) Fiss, B.G.; Richard, A.J.; Douglas, G.; Kojic, M.; Friščić, T. *Chem. Soc. Rev.* **2021**, 50(14), 8279-8318.

50 (a) Bolm, C.; Hernández, J.G. *Angew. Chem. Int. Ed*. **2019**, 58, 3285-3299. (b) Tan, D.; García, F. Chem. Soc. Rev. 2019, 48(8), 2274-2292.

computational treatment; either homogeneous or heterogeneous. Of course, this is complementary to the inclusion of the force, which must be done through the application of special treatments.[51]

For example, heterogeneous models are employed to model mechanochemical processes related to the reproduction of Atomic Force Microscopy (AFM) experiments,[52] and more generally, reactions involving a metallic surface submitted to force, or friction.[53] Other specific examples where plane waves have been applied are the investigation of hydrostatic-pressure driven redox reactions in metalorganic chalcogenides reported by Melosh and co-workers,[54] or the study of thermomechanical properties of plastic crystals presented by Naumov and co-workers.[55] On the other hand, homogeneous techniques are typically employed for the investigation of the mechanical stress in organic and organometallic systems,[56] as well as in the field of polymer mechanochemistry.[57]

51 Ribas-Arino J. Marx, D. *Chem. Rev*. **2012**, 112, 5412–5487.

52 Microscopy, F.; Force, K. P.; Liljeroth, P. *ACS Nano* 2018, 12, 6, 5274–5283.

53 Zhang, Y.; Wang, Y.; Jing-tao, L.; Brandbyge, M.; Berndt, R. *Angew. Chem. Int. Ed.* **2017**, 111, 11769–11773.

54 Yan, H.; Yang, F.; Pan, D.; Lin, Y.; Hohman, J. N.; Solis-Ibarra, D.; Li, F.H.; Dahl, J.E.P.; Carlson, R.M.K.; Tkachenko, B.A.; Fokin, A.A.; Schreiner, P.R.; Galli, G.; Mao, W.L.; Shen, Z.X.; Melosh, N.A. *Nature*, **2018**, 554(7693), 505–510.

55 Commins, P.; Hu, Q.; Ahmed, E.; Karothu, D. P. *J. Am. Chem. Soc.* **2020**, 142(25), 11219-11231.

56 (a) Krupička, M; Dopieralski, P.; Marx, D. *Angew. Chem. Int. Ed*. **2017**, 56, 7745-7749. (b) Sha, Y.; Zhang, Y.; Xy, E.; Wang, Z.; Zhu, T.; Craig, S.L.; Tang, C. Tang, C. *ACS Macro Lett*. **2018**, 7, 1174−1179. (c) Bettens, T.; Alonso, M.; Geerlings, P.; Proft, F.D. *Chem. Sci*. **2020**, 11,1431.

57 Akbulatov, S.; Tian, Y.; Huang, Z.; Kucharski, T.J.; Yand, Q.Z.; Boulatov, R. *Science* 2017, 357, 299–303. (b) Klein, I.M.; Husic, C.C.; Kovács, D.P.; Choquette, N.J.; Robb, M.J. *J. Am. Chem. Soc.* **2020**, 142, 38, 16364–16381.

Another common situation is to deal with a mixture of homogeneous and heterogeneous processes in the same transformation. This is the case of those homogeneous reactions involving the presence of a solid oxidant or reductant. These hybrid systems involve one transformation on the solution phase and a redox reaction originated in the surface of the solid. Generally, the redox process is disregarded since the barrier of the step is negligible in comparison to the rate determining step (RDS), specifically, in those reactions where the metal is employed to form the active species.[58] However, in some cases, such as reductive couplings, were the reductant rules the whole process, this species should not be overlooked. In this regard, the characterisation of the redox process with heterogeneous methods is not feasible due to the high complex molecular systems that encompass these transformations, which would imply enormous computational cost. Therefore, they are either approximated through homogeneous methods[59] or using alternative strategies such as thermodynamic cycles.[60]

58 Moncomble, A.; Le Floch, P.; Gosmini C. *Chem. Eur. J.*, **2009**, 15, 4770-4774. (b) Li, Z.; Jiang, Y.; Fu, Y. *Chem. Eur. J.*, **2012**, 18, 4345-4357.

59 (a) Jiang, F.; Ren, Q. *J. Organomet. Chem*. **2014**, 757, 72-78. (b) Ren, Q.; Zhang, D.; Zheng, L. *J. Organomet. Chem*. **2021**.

60 (a) Shimodaira, Y.; Miura, T.; Kudo, A.; Kobayashi, H. *J. Chem. Theory Comput*., **2007**, 3(3), 789-795. (b) Funes-Ardoiz, I.; Maseras, F. *ChemPhysChem*, **2019**, 20(1), 159–162.

General Objectives

The investigation of systems which are in the frontier between homogeneous and heterogeneous catalysis requires the construction of bridges between the two worlds. This constitutes a significant challenge for the community working on catalysis which has to be solved to achieve the full potential of these new systems. Thus, there is a growing need to improve the mechanistic understanding, and computational chemistry can play an important role.

The main objective of this thesis is to explore to what extend methods commonly employed for the study of homogeneous reactions can be applied to systems located in the "limbo" between homogeneous and heterogeneous fields. Specifically, our attention has been directed towards mechanochemical reactions and mostly homogeneous reactions with participation of solid reductants. To this end, each chapter has been devoted to the study of one or several transformation(s) within these categories.

Chapter I is focused on the development of a methodology to model a specific type of mechanochemistry: ball-milling reactions.

Chapter II is centred on the characterisation of the mechanism of a reductive coupling transformation.

Chapter III is related to the investigation of a cross-coupling reaction under reductive conditions.

Each chapter of this PhD thesis contains an objectives section in which a more detailed description is provided.

UNIVERSITAT ROVIRA I VIRGILI
BEYOND CONVENTIONAL DFT CATALYSIS: MECHANOCHEMISTRY AND SOLID REDUCTANTS
Bruna Sánchez Pladevall

Theoretical background

UNIVERSITAT ROVIRA I VIRGILI
BEYOND CONVENTIONAL DFT CATALYSIS: MECHANOCHEMISTRY AND SOLID REDUCTANTS
Bruna Sánchez Pladevall

In this chapter we present a brief discussion of some aspects of the methods that have been applied in the different chapters and which may be not of a widespread use among the computational homogeneous catalysis community.

1. Microkinetic modeling

Computational chemistry is a well-established field that has aided the mechanistic understanding of a wide range of processes. Computational methods have indeed become a strategic tool for rational design to achieve a cleaner and economically affordable chemistry. However, computational chemistry has become so efficient in reproducing free energies, that a further step seems possible in the reproduction of experimental data. Traditionally, computational chemists have used free energy profiles to investigate chemical reactivity, while experimental chemists typically report reaction times and yields and, in the case of kinetic studies, the evolution of concentrations over time.

The traditional approach in computational homogeneous catalysis for the last decades has been to make an implicit qualitative connection between free energy barriers and the efficiency of a process: reactions with barriers up to 20 kcal/mol are considered fast at room temperature, and those up to 30 kcal/mol are considered feasible upon temperature increase. These simple guidelines have been sufficient in many cases and have brought computational chemistry to its current prominent role. However, for complex systems where several competing pathways can be found, and/or where concentrations play a crucial role, the rationalisation of the reaction outcome with only energetic parameters is not sufficient. For example, the selectivity of a system can be extremely affected by concentration if the competing processes present different molecularities.[1]

1 Besora, M.; Maseras, D. *WIREs Comput Mol Sci*. **2018**, e1372.

In these situations, microkinetic modelling emerges as the perfect bridge between computational and experimental data because it allows the direct connection of the computed free energies, with rate constants and consequently, with experimental times and yields. The use of microkinetic models has proved to be a reliable tool for the connection of theory and experiments and is becoming increasingly applied to the study of homogeneous,[2] heterogeneous[3] and biological[4] processes. Below we will briefly go through the main concepts involved in microkinetic modelling focusing on homogeneous processes.

Consider the following chemical reaction: $aA + bB \rightleftharpoons cC + dD$, the expression of the rate law, is depicted in Equation 1.

$$rate = \frac{1}{c}\frac{d[C]}{dt} = \frac{1}{d}\frac{d[D]}{dt} = -\frac{1}{a}\frac{d[A]}{dt} = -\frac{1}{b}\frac{d[B]}{dt} = k[A]^x[B]^y \qquad (1)$$

where k is the rate constant of the transformation, and *x*, *y* are the rate orders.

The rate law accounts for all the elementary steps within a chemical reaction, providing a relationship between concentration and time. Since in most homogeneous transformations the mechanism involves multiple steps, the reaction rate law will be conformed by the set of elementary steps that contribute to the overall kinetic scenario. The microkinetic model allows to put

2 (a) Sameera, W.M.C; Maseras, F. *WIREs Comput. Mol. Sci*. **2012**, 2, 375–385. (b) Santoro, S.; Kalek, M.; Huang, G.; Himo, F. *Acc. Chem. Res*. **2016**, 49, 1006–1018. (c) Brezny, A.C.; Landis, C.R. *ACS Catal.* 2019, 9(3), 2501–2513. (d) Darù, A.; Hu, X.; Harvey, J.N. *ACS Omega* 2020, 5(3), 1586–1594.

3 (a) Maestri, M.; *Chem. Commun.,* **2017**, 53, 10244-10254. (b) Mao, Y., Wang, H. F., & Hu, P. *WIREs Comput. Mol. Sci.*, **2017**, 7, e1321. (c) Ding, Y.; Xu, Y.; Song, Y.; Guo, C.; Hu, P. *J. Phys. Chem. C* 2019, 123(45) 27594–27602. (d) Ishikaea, A.; Tateyama, Y. *ACS Catal.* 2021, 11(5), 2691–2700.

4 Slusarczyk, A. L.; Lin, A.; Weiss, R. *Nat. Rev. Genet*. **2012**, 13, 406–420.

all this processes together, obtaining a theoretical definition of the kinetics of the process.

The application of a microkinetic model is simple: first, we compute the complete mechanistic picture of the reaction (including side reactions). Then, we convert the energetic profile into a reaction network with only the relevant elementary steps. Finally, we compute the associated rate constants (k_1 and k_{-1}) for each step.

It is important to mention here that when rate constants have concentration units, we must be careful with the reference state. Most computational packages provide free energies in ideal gas conditions. These means, a temperature of 298 K and a pressure of 1 atm, which corresponds to a reference state concentation of 0.0487 M. As most homogeneous catalysis reactions are carried out in solution, the reference state should be 1 M. This fact does not have any effect to first order reactions since the dimensions of the rate constant (s^{-1}) do not account for concentration. But the rate of reactions with order two or higher will be altered upon the modification of the reference state.

The reference state can be converted into the 1 M solution standard state, through the application of an additive term of 1.89 kcal/mol for reactions at 298 K. This value is obtained with Equation 2. Notice that it has to be recomputed depending on the temperature of the specific transformation.[5]

$$\Delta G_M = -RT\ ln\left(\frac{1/_{24}M}{1M}\right) \quad (2)$$

For the sake of simplicity, in this thesis this conversion has been done through the application of the GoodVibes program[6] developed by Dr. Funes-Ardoiz (former member of our group). One feature of the program is to recompute all

5 Jensen, J. H. (2010) *Molecular Modeling Basis*, CRC Press: Boca Raton, Finland, pp. 74.

6 I. Funes-Ardoiz, R. S. Paton, GoodVibes: GoodVibes v1.0.1. Zenodo.

the partition functions allowing to modify the temperature or concentration of the system, thus, enabling the modification of the reference state as well as the introduction of the operando temperature.

Once we have corrected the reference state and accounted for the reaction temperature, we can apply the Eyring-Polanyi equation[7] which links the free energy barrier of a reaction with its rate constant (Equation 3).

$$k = \frac{\kappa k_B T}{h} e^{\frac{\Delta G^{\ddagger}}{RT}} \quad (3)$$

where k is the rate constant, κ the transmission factor, k_B the Boltzman's constant, T the temperature, h the Planck's constant, $\Delta G^{\ddagger}$ the activation energy, and R the ideal gas constant. The transmission factor was assumed to be 1 in all cases.

For most of the processes, $\Delta G^{\ddagger}$ is obtained through the calculation of the transition state, however, in homogeneous systems, it is typical to have some steps with no barrier in the potential energy surface, which are ruled by coordination/decoordination processes. Those reactions are governed by diffusion and its barrier can be approximated with the Stokes-Einstein equation with the Smoluchowski formulation (Equation 4).[8]

$$k_D = \frac{8 k_B T}{3 \eta} \quad (4)$$

where k_D is the rate constant for the dissociation procedure, k_B the Boltzmann constant, T the temperature and η the viscosity.

Once we have collected the full set of rate constants, we can define a system of differential equations that will tell us the evolution of concentrations through time. This mathematical model can be applied through a variety of software

7 Eyring, H. *J. Chem. Phys*. **1935**, 3, 107.

8 Rush, L. E.; Pringle, P. G.; Harvey, J. N. *Angew. Chem. Int. Ed*. **2014**, 53, 8672–8676.

packages specifically designed for this purpose. In the projects developed in this thesis, we have employed COPASI 4.22,[9] however there are other alternatives such Acuchem[10] or Tenua.[11] The use of this mathematical model provides the evolution of the initial concentrations over the desired timelapse. Besides, we can extract predicted conversions and reaction times, enabling a direct link between computations and experimental data.

2. Cluster continuum model

The use of continuum solvent models is the most widely extended methodology for the introduction of solvent into DFT calculations due to their broad applicability and reduced computational cost. However, in some specific situations, there is a need to introduce explicit solvent molecules in the calculation, e.g., when the solvent acts as ligand to the metal center, when it is required as proton shuttle, etc. In such cases, a hybrid model is the most common choice: the continuum solvent model is combined with explicit solvent molecules introduced as another discrete substrate. The application of a hybrid model presents a major drawback; the unrealistic consideration of the solvent as an independent non-interacting entity is translated into a systematic error on the DFT calculations.

The problematic nature of hybrid solvent models is constituted by two main error sources. First, an intrinsic error of the DFT method which, at once, is composed by diverse terms: (i) overestimation of the entropy of the solvent molecules because the Gibbs energy contributions from the solvation procedure are included in the potential energy of the system, (ii) neglection of interactions between explicit and implicit solvent molecules, and (iii) counterpoise error.

9 Hoops, S.; Sahle, S.; Gauges, R.; Lee, C.; Pahle, J.; Simus, N.; Singhal, M.; Xu, L.; Mendes P.; Kumer, U.; *Bioinformatics*, **2006**, 22, 3067-3074.

10 Braun, W.; Herron, J. T.; Kahaner, D. K. *Int. J. Chem. Kinet.* **1998**, 20, 51–62.

11 Wachsstock, D. (2007). Tenua: The kinetics simulator for java.

These error sources are extremely difficult to assess since they arise from the nature of the implicit/explicit models.

The second error source resides on the transfer of a solvent molecule from the bulk of solvent to the active centre. The proper treatment of this process is crucial for the correct reproduction of a specific system. One approach, which is extensively used, yet not elegant, is the consideration of the necessary explicit solvent molecules in all the energetic profile.[12] In this manner, part of this systematic error is present throughout the whole mechanism, and therefore cancelled. However, the proper introduction of this model implies a huge computational time, due to the conformational search required to define the most stable adducts. Besides, in cases where the solvent molecules must be in a specific disposition only in some intermediates, e.g., as proton shuttle in a transition state, the rest of intermediates are reproduced with an extra-stabilization. This arises from the interactions between the substrates and the solvent molecules and can be specifically notorious upon the use of protic solvents. Finally, this approach does not allow the consideration of the concentrations of reactants and solvent, which is crucial in those systems where it is necessary to apply a microkinetic model.

An alternative approach, which we believe that, up until now, is the best methodology to solve the aforementioned error, is the use of a cluster continuum model i.e., the explicit solvent molecule is subtracted from a cluster that represents the bulk.[13] Consider Equation 5, where $(Solv)_n$ represents the

12 (a) I. Yildiz, *J. Phys. Chem. A*, **2016**, 120 (20), 3683-3692. (b) S. Kirmizialtin, B. S. Yildiz, I. Yildiz, *J. Phys. Org. Chem*. **2017**, e3711, 1-10.

13 (a) Pliego, J. R.; Riveros, J. M. *J. Phys. Chem. A* **2001**, *105*, 7241-7247. (b) Bryantsev, V. S.; Diallo, M. S.; Goddard III, W. A. *J. Phys. Chem. B* **2008**, *112*, 9709-9719. (c) Marenich, A. V.; Ding, W.; Cramer, C. J.; Truhlar, D. G. *J. Phys. Chem. Lett.* **2012**, *3*, 1437-1442. (d) Ho, J.; Ertem, M. Z. *J. Phys. Chem. B* **2016**, *120*, 1319-1329. (e) Tomaník, L.; Muchová, E.; Slavíeček, P. *Phys. Chem. Chem. Phys.*, **2020**, **22**, 22357-22368.

bulk of the solvent as a cluster of a given number of molecules, n, and x the number of molecules released from the cluster.

$$(Solv)_n \xrightarrow{\Delta G_1} x\,Solv + (Solv)_{n-x} \quad (5)$$

From a physical perspective, this process should not represent any modification of the global free energy of the system since the bulk is infinitely large with respect to a punctual molecule. However, the release of an isolated molecule results in a negative ΔG_1 when computed through DFT techniques due to the contribution of the punctual solvent molecule to the free energy of the system. In the cluster continuum model, the energy difference obtained for Equation 5 can be used to correct the error associated to the transfer of a solvent molecule from the bulk to the active center (AC). The process is presented in Equation 6.

$$AC + (Solv)_n \xrightarrow{\Delta G_2} AC(Solv)_n \quad (6)$$

Therefore, in this approach both equations will be summed, giving a corrected definition of the system, represented by ΔG_3 (Equations 7 and 8):

$$\Delta G_3 = \Delta G_1 + \Delta G_2 \quad (7)$$

$$AC + (Solv)_n \xrightarrow{\Delta G_3} AC(Solv)_n + (Solv)_{n-x} \quad (8)$$

The implementation of this approach implies a practical problem: the representation of the process with a finite cluster implies a substantial variation of ΔG_1 upon the number of molecules considered *i.e.*, the larger the cluster, the closer to real system and the more accurate description of the process. The consideration of more molecules, and the subsequent reduction of the error, in the cluster brings us to an asymptotic value, which can be interpreted as the intrinsic error of hybrid methods outlined above (Scheme 1).

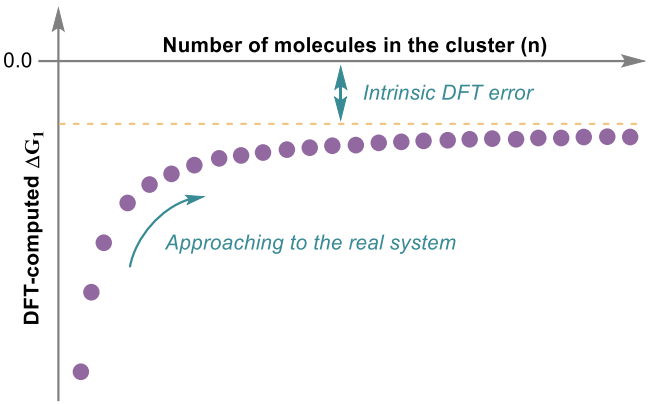

Scheme 1. Reduction of the error on the continuum cluster model upon the increase of number of molecules in the cluster (n).

Overall, the application of the cluster continuum model allows the correction of the error associated to the transfer of a solvent molecule from the bulk to the active centre. The method provides in our opinion the best approximation that we can apply when hybrid solvation is required. This treatment has been applied in *Chapter I*, when analyzing the synthesis of 2,4-dinitrophenylhidrazones.

3. Standard Reduction Potential

The Standard Reduction Potential (SRP) is the thermodynamic parameter that captures the tendency of a determinate chemical species to gain or lose electrons (Equation 9). It is a highly important value in many fields because it allows the determination of the stability of a compound in specific conditions as well as the prediction of the evolution of a redox reaction.

$$Ox^{m} + e^{-} \rightarrow Red^{m-1} \quad (9)$$

The theoretical calculation of SRP is accomplished through the application of thermodynamic cycles which permit the decomposition of the target reaction into different steps, achieving a simplified approach for the calculation of the

parameter based on the sum of all the contributions.[14] There are several variations of these thermodynamic cycles focused on the determination of redox processes that occur exclusively in solution.[15] However, it was not until 2007, that Kobayashi and co-workers developed the first strategy to compute SRP of reactions involving solid species.[16] The authors derived a thermodynamic cycle for the conversion of a solid specie to the solvated metal ion based on the Born-Haber cycle. The decomposition of the process leads to the thermodynamic cycle shown in Scheme .

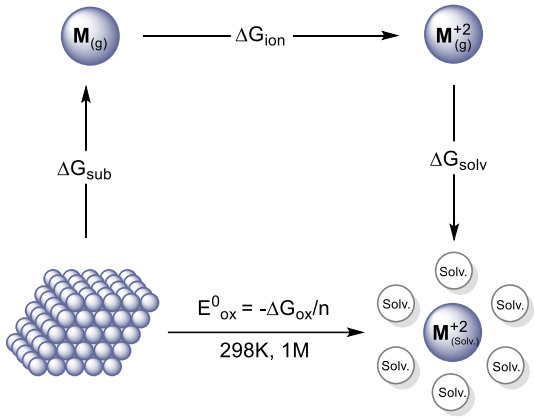

Scheme 2. Thermodynamic cycle based on the Born-Haber cycle employed to compute the SRP of diverse metals.

In line with this decomposition of the oxidation process, the SRP of the metallic species can be approximated through the sum of the free energies of sublimation (ΔG_{sub}), ionization (ΔG_{ion}), and solvation (ΔG_{solv}) as depicted in Equation 10. The first term, ΔG_{sub}, which refers to the energy of the sublimation

14 Arumugam, K.; Becker, U. *Minerals* **2014**, 4, 345-387.

15 (a) Winget, P.; Weber, E. J.; Cramer, C. J.; Truhlar, D. G. *Phys. Chem. Chem. Phys*. **2000**, 2, 1231-1239. (b) Marenich, A. V.; Ho, J.; Coote, M. L.; Cramer, C. J.; Truhlar, D. G. *Phys. Chem. Chem. Phys.* **2014**, 16, 15068-15106.

16 Shimodaira, Y.; Miura, T.; Kudo, A.; Kobayashi, H. *J. Chem. Theory Comput*., **2007**, 3(3), 789-795.

from solid to gas, is equivalent to the cohesive energy (CE). This value would need to be evaluated through the difference between a bulk solid (periodic system) and an isolated atom. To avoid this calculation, the authors took the experimental value from the work by Friesner and co-workers.[17] The second term, ΔG_{ion}, which refers to the ionization energy, has been mostly obtained through calculations, however, for some of the metals the calculated ionization energies were underestimated, therefore the authors used the experimental value.[18] Finally, the energy of solvation, ΔG_{solv}, is calculated through molecular models; the solvent is introduced in an indirect manner through the application of a self-consistent reaction field method (PCM).

$$E_{red}^{0} = -E_{ox}^{0} = \frac{-\Delta G_{ox}^{0}}{n} = \Delta G_{sub}^{0} + \Delta G_{ion}^{0} + \Delta G_{solv}^{0} \qquad (10)$$

The methodology reproduces the SRP of 16 metals with a standard deviation of 0.20-0.23V, which are fairly good errors. However, there is still room for improvement, specifically, a more accurate evaluation of the entropy contribution in both the cohesive and ionization energy is required.

In 2018, our group reported a reviewed strategy focused on solving these issues.[19] We identified a systematic error towards a more positive potentials which was attributed to the lack of entropic contributions. Therefore, entropy corrections were introduced to both the cohesive and ionization energies leading to revised values: ΔG_{sub}^{corr} and ΔG_{ion}^{corr}. Our method achieves an improvement of the systematic error achieving a decrease of the absolute error from 0.23V to 0.04V, which is below 1 kcal/mol. This optimized strategy has been used for the calculation of all the redox steps involving solids throughout the manuscript (*Chapters II and III*).

17 Baik, M-H.; Friesner, R. A. *J. Phys. Chem. A* **2002**, 106, 7407.

18 Han, W.-G.; Liu, T.; Lovell, T.; Noodleman, L. *Inorg. Chem*. **2006**, 45, 8533.

19 Funes-Ardoiz, I.; Maseras, F. *ChemPhysChem*, **2019**, 20(1), 159–162.

4. Volcano plots

In the last decades, the field of catalyst design has experienced a shift from trial-and-error approaches to the development of predictive tools which allow the screening of a great amount of potential catalysts in a significantly faster and effective manner. One of these tools, namely volcano plots, will be introduced in the following section.

From the Sabatier principle to predictive volcano plots

Since the beginning of the 20th century, the Sabatier principle has been employed to qualitatively describe the optimal catalyst in heterogeneous systems.[20] This principle states that to achieve high catalytic activity, the substrate-catalyst interactions should be neither too strong nor too week. If the binding is too weak there will be difficulties in binding the reactant with the catalyst and thus, no reaction will take place. Otherwise, if the binding is overly strong, there will be difficulties in releasing the product leading to lower activity (

Figure **3**, left). This picture has been widely used to rationalize trends in heterogeneous catalysis.[21] However, its qualitative nature implies a lack of predictive power and cannot be used to design rules.[22]

One of the biggest challenges to translate the Sabatier principle into a quantitative tool is the definition of a suitable quantity to describe the relevant "bond strength". In a real system there can be hundreds of variables that could be used to describe a reaction. However, visualizing trends with more than 3

20 Sabatier, P. (1920). La catalyse en chimie organique. In Librairie Polytechnique.

21 Che, M. *Catal. Today*, **2013**, 218, 162–171.

22 Medford, A. J.; Vojvodic, A.; Hummelshøj, J. S.; Voss, J.; Abild-Pedersen, F.; Studt, F.; Bligaard, T.; Nilsson, A.; Nørskov, J. K. *J. Catal*., **2015**, 328, 36–42.

dimensions is a harsh task, hence we must reduce the dimensionality of the problem.

It has been found that energies of reaction intermediates and transition states within a particular reaction are dependent on each other. This implies the existence of scaling relations which express the full mechanistic picture as a function of a single (or a few) reactivity descriptor(s). That means all the species involved in a particular reaction mechanism will ideally scale linearly with some physical or chemical property that correctly describes the reaction system.

The most common way of building linear scaling relations (LSRs) is through energy-based descriptors *i.e.,* the properties of the system can be represented as a function of the relative energy of one or more key intermediates. The scaling relations obtained can then be used to identify the relevant parameters that determine the activity and selectivity (by analyzing the key intermediates). This is used as basis to construct other reactivity descriptors, which comprise the relevant properties in the mechanistic scenario.[23]

Overall, LSRs allow to express the energies of all the intermediates and transition states as a function of one or few descriptor(s), leading to a more manageable and easier way to visualize the problem. This allows the projection of a whole transformation in terms of the performance of the chemical reaction as function of the selected descriptor(s). Such representation usually gives rise to a volcano-shaped plot in which the top corresponds to a balanced interaction, and thus the region in which a high catalytic activity is expected. This constitutes in fact, a quantitative representation of the Sabatier principle (Figure 3). Upon the construction of these volcano plots, we obtain a predictive method,

23 Zhao, Z. J.; Liu, S.; Zha, S.; Cheng, D.; Studt, F.; Henkelman, G.; Gong, J. *Nat. Rev. Mat*., **2019**, 4(12), 792–804.

in which just with the calculation of the descriptor, we will be able to determine the performance of a selected catalyst.

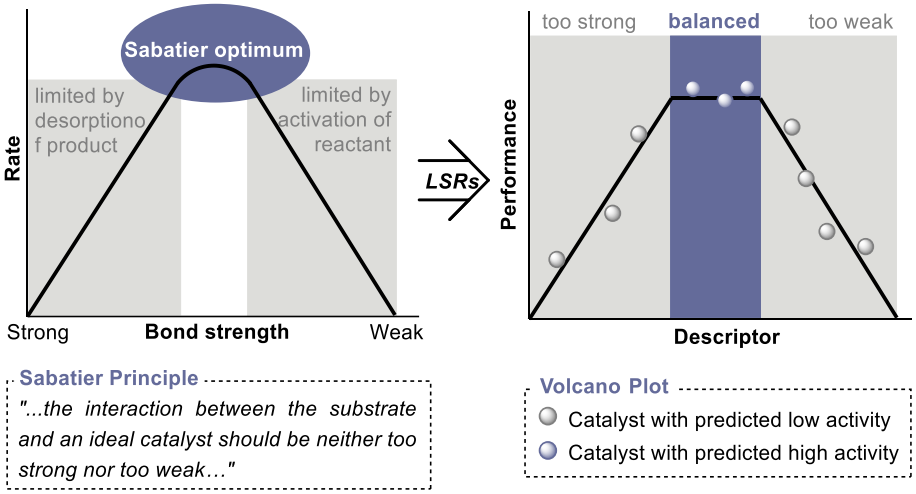

Figure 3. Conversion of the qualitative Sabatier principle (left) to the quantitative volcano plots (right) through the application of linear scaling relationships (LSRs).

Volcano plots in homogeneous catalysis

Volcano plots have been extensively used in electrocatalysis and heterogeneous catalysis.[24] In 2008, Swiegers hypothetically proposed the application of this tool to homogeneous catalysis.[25] However, it was not until 2015 when the Corminboeuf group successfully built the first volcano plot for a Suzuki-

24 (a) Parsons, R. *Trans. Faraday Soc.*, **1958**, 54, 105. (b) Trasatti, S. *J. Electroanal. Chem. Interfacial Electrochem*. **1972**, 39, 163. (c) Nørskov, J.K.; Bligaard, T.; Rossmeisl, J.; Christensen, C.H. *Nat. Chem*. **2009**, 1, 37.

25 Swiegers, G. F. (2008). Synergy in Heterogeneous, Homogeneous, and Enzymatic Catalysis. The "Ideal" Catalyst. Mechanical Catalysis: Methods of Enzymatic, Homogeneous, and Heterogeneous Catalysis, 181–207.

Miyaura coupling.[26] Their work succeeded in reproducing the trends in this system becoming the proof-of-principle that volcano plots (formerly only used in the heterogeneous community) can be translated to homogeneous systems.

Since then, several theoretical refinements have been developed, ranging from the construction of kinetic volcanos[27] to the incorporation of big data and machine learning[28] aiding to the creation of unified pictures of diverse homogeneous systems. Although the field is still in his infancy, it has demonstrated a promising potential to become an outstanding tool for the identification of promising catalysts in homogeneous systems.[29]

Construction of a volcano plot

The process of building a volcano plot is depicted in Figure **4**4. First, we must elucidate the reaction mechanism and compute it for a set of selected systems. In homogeneous chemistry this typically involves a modification on the ligand, however, we can tune other factors depending on what we want to study, *e.g.*, modification of the substrate to study the scope of the reaction.[30] We must perform a deep study of the reaction mechanism as a wrong description of the reaction pathway precludes the linear relationship between the energies of the intermediates or with any other physical and chemical property.

Once we have computed the reaction mechanism for our set of systems we must find the optimal descriptor to derive the LSRs. As mentioned above, this is generally an energy-based descriptor, *i.e.*, the energy of a key intermediate is used to represent the system (the energy of intermediate 1 in Figure 4).

26 Busch, M.; Wodrich, M. D.; Corminboeuf, C. *Chemical Science*, **2015**, 6(12), 6754–6761.

27 Wodrich, M. D.; Busch, M.; Corminboeuf, C. *Chemical Science*, **2016**, 7(9), 5723–5735.

28 Meyer, B.; Sawatlon, B.; Heinen, S.; Von Lilienfeld, O. A.; Corminboeuf, C. *Chemical Science*, **2018**, 9(35), 7069–7077.

29 Anand, M.; Nørskov, J. K. *ACS Catalysis*, **2020**, 10(1), 336–345.

30 Sawatlon, B.; Wodrich, M. D.; Corminboeuf, C. *Org. Lett.*, **2020**, 22(20), 7936–7941.

However, it can also be any other physical or chemical property relevant to our system.

Having established the scaling relations, we are able to describe any reaction energy as a function of the selected descriptor. Thus, we can obtain theoretical reaction free energies for each step of the reaction purely depending on the value of the descriptor. The next step is to plot the linear functions derived from the LSRs versus the catalytic activity of the different catalysts. This is, in the case of a thermodynamic picture of our reaction the thermodynamically least favorable step. In the case of a kinetic picture, this would be the highest activation energy. In the example of Figure 4 we have assumed a purely thermodynamic perspective, thus the catalyst performance is represented by the potential determining step -ΔG(pds). The superposition of all the functions in a single plot leads to overlapping lines. The lower laying lines (those representing the higher energy determining step) are the ones used to construct our volcano (Figure 4, bottom).

With the volcano plot in hand, we can now predict the activity of any other catalyst by computing our descriptor variable. The value of the descriptor for a new compound determines the position of the metal in the *x*-axis of the volcano (Figure 4, New Cat.). We can then project the target on the *y*-axis until the delimiting slope. The value obtained for the *y*-axis corresponds to the energy of the potential determining step of the catalyst. Thus, we can identify promising catalysts (those falling into the plateau of the volcano) and analyse their characteristics to perform a rational design for other potentially good candidates.

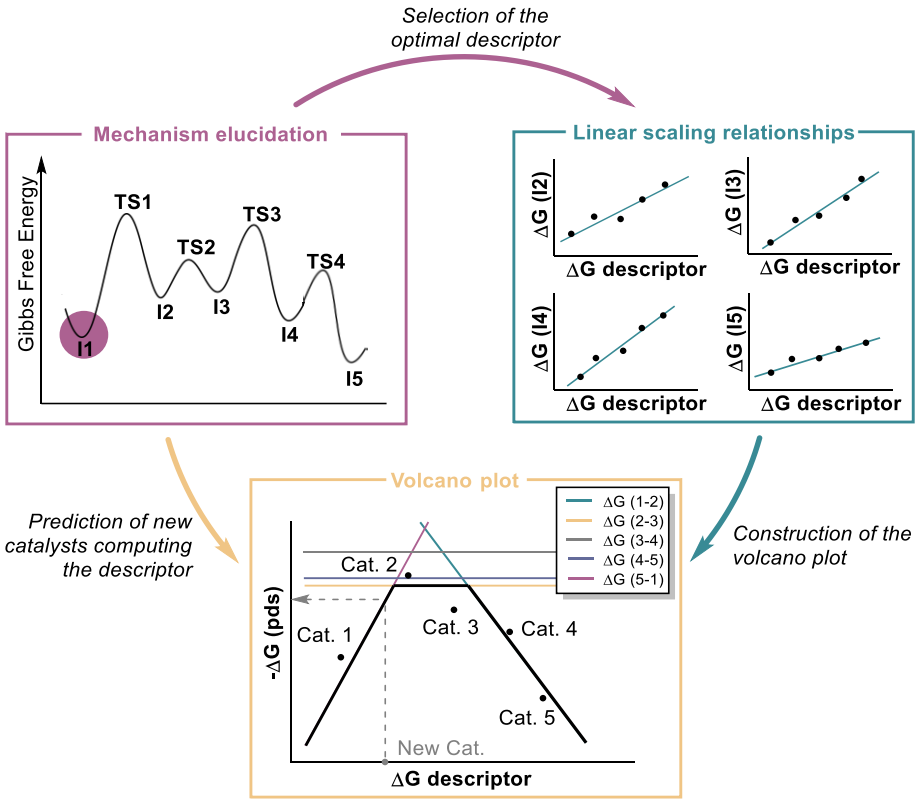

Figure 4. Steps required for the construction of a volcano plot.

Chapter I. Understanding Ball-milling Processes with DFT Calculations and Microkinetic Modelling

UNIVERSITAT ROVIRA I VIRGILI
BEYOND CONVENTIONAL DFT CATALYSIS: MECHANOCHEMISTRY AND SOLID REDUCTANTS
Bruna Sánchez Pladevall

1. Introduction

Chemical reactions induced by the absorption of mechanical energy may be the first chemical reactions carried out by humankind throughout history, even before than thermally activated reactions. Already in the stone age, mortars and pestles were used to prepare pigments and medicines, even if the eventual chemical changes were not conscious.[1] Obviously, these hypothesis about ancient chemistry are mere speculation; the first ever reference of mechanically activated reactions appeared in 315 B.C. in the book "Περὶ λίθων" (On Stones) by Theophrastus of Eresus.[2] However, there is no other detailed historical information on how these reactions were initiated or if they were extensively used or not. Indeed, it was not until almost 2000 years later, in the 19th century, where the first systematic investigations on the were reported by Michael Faraday, Matthew Carey Lea and Walthère Spring.[3] These reactions were further named by Ostwald as "mechanochemistry" and included as the fourth type of chemical activation together with thermochemistry, electrochemistry, and photochemistry.[4]

The term mechanochemistry has been widely employed for all those reactions induced by mechanical force albeit other terms, such as tribochemistry, referring to more specific reactivity, were also used.[5] Indeed, the terminology is among the primary reasons for the slow development of the field. Each of the numerous disciplines working on mechanochemistry applies different

1 Takacs, L. Chem. Soc. Rev., **2013**, 42, 7649-7659.

2 Takacs, L. *J. Met*. **2000**, 52, 12.

3 (a) Faraday, M. *Q. J. Sci., Lit., Arts*. **1820**, 8, 374. (b) Lea, M.C. *Br. J. Photogr*. **1866**, 13, 84. (c) Spring, W. *Bull. Acad. R. Med. Belg*. **1880**, 49(2), 323. (d) Lea, M.C. *Am. J. Sci*. **1892**, 43(3), 527.

4 Ostwald, W. *Handbuch der Alemanien Chemie.* Akademische Verlagsgesellschaft mbH: Leipzig,Germany, **1919**.

5 Carlton, H.; Huitink, D.; Liang, H. *Lubricants*, **2020**, 8, 87-108.

vocabulary, leading to confusion among the community, which makes things especially difficult for newcomers into the field.[6]

The unclear terminology surrounding mechanochemical reactions is justifiable by the large number of variables involved on force activated reactions, which, moreover, are mostly system dependent. This, combined with the interdisciplinary nature of the field, induces difficulties on the classification of mechanochemical reactions. We have collected in Scheme 1 an overview of different divisions of mechanochemical reactions that are commonly found in the literature. Note, that the classification presented here is, to some extent, subjective and might disagree with some publications.

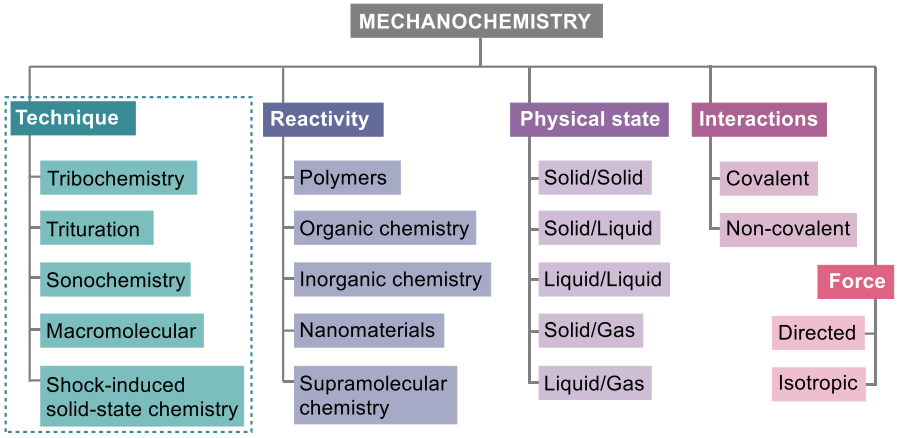

Scheme 1. Division of mechanochemistry according to the techniques, reactivity, the physical state, the type of interaction broken, and the nature of the force.

The main division that one must consider when talking about mechanochemical reactions is the type of technique[7] employed: (i) tribochemistry, reactions

6 Michalchuk, A. A. L.; Boldyreva, E. V.; Belenguer, A. M.; Emmerling, F.; Mackenzie, K. J. *Front. Chem.* **2021**, 9, 685789.

7 Suslick, K.S. Faraday Discuss.,**2014**, 170,411–422

induced by surface friction, (ii) trituration, including all type of grinding and milling techniques, (iii) sonochemistry, those reactions activated through sound, (iv) macromolecular, referring from single molecule Atomic Force Microscopy (AFM) to breakage of polymer chains and conformational alteration, and (v) shock-induced solid-state chemistry, reactions induced by compression.

For each of these techniques one has to consider many other aspects. First, the reactivity under study,[8] there is a huge difference between polymerization and inorganic reactions. The second aspect is the physical state,[9] the presence of solid, liquid or gas reagents can strongly influence the reactivity, for instance through the importance of diffusion events. Then the type of interactions that are broken,[10] covalent bonds usually require multinano-Newton forces or non-covalent interactions such as hydrogen-bonding, imply subnano-Newton forces. Finally, the nature of the force,[11] either directional or isotropic.

Each mechanochemical technique has specific characteristics, as well as a range of features that can be tuned. For example, sonochemistry could be included in the isotropic force type, however, it can take place in all the physical states involving at least one liquid reagent and can be used to break both covalent and non-covalent interactions.

All the above-mentioned issues hamper the obtention of a unified picture of mechanochemical reactions. In this regard, the theoretical understanding can assist the rationalisation of this reactivity. Herein we will provide a brief explanation on the most important theoretical models for the calculation of

8 Tan, D.; García, F. Chem. Soc. Rev., **2019**, 48, 2274--2292

9 Michalchuk, A. A. L.; Boldyreva, E. V.; Belenguer, A. M.; Emmerling, F.; Mackenzie, K. J. *Front. Chem*. **2021**, 9, 685789.

10 Neill, R.T.O.; Boulatov, R. *Nat. Rev. Chem.* **2021**, 5, 148-167.

11 Makarov, D.E. *J. Chem. Phys*. **2016**, 144, 030901.

mechanochemical reactions. For a more throughout discussion, the reader is referred to general reviews found in reference [12].

The first ever theoretical rationalisation of mechanochemical reactions was proposed by Kauzmann and Eyring in 1940.[13] They introduced an extension of the transition state theory (TST) to account for the effect of an external constant force. The force is included as a component F which acts in a determinate distance of the reaction coordinate $\Delta\xi$ and that lowers the total activation energy (Equation 1).

$$\Delta G^{\ddagger}_{Bell}(F_0) = \Delta G^{\ddagger}(F_0 = 0) - F_0\Delta\xi \quad (1)$$

where $\Delta G^{\ddagger}$ is the activation energy in absence of an external force. The applied external force can be modelled as a Morse potential of the dissociation of a chemical bond (Scheme 2). The external force moves the bond away from equilibrium (stretched bond), obtaining a lower dissociation energy. This simple concept was further refined and its usually referred as the Bell model.[14]

12 (a) Beyer, M.K.; Clausen-Schaumann, H. *Chem. Rev.* **2005**, 105, 2921–2948. (b) Ribas-Arino J. Marx, D. *Chem. Rev*. **2012**, 112, 5412–5487. (c) Kochhar, G.S.; Heverly-Coulson, G.S.; Mosey, N.J. (**2015**) In *Polymer Mechanochemistry*, (pp. 37–96), Ed. Springer International Publishing, Cham. Theoretical Approaches for Understanding the Interplay Between Stress and Chemical Reactivity. (d) Stauch T. Dreuw, A. *Chem. Rev. 2016*, 116, 14137–14180.

13 Kauzmann, W.; Eyring, H. *J. Am. Chem. Soc*. **1940**, 62, 3113

14 Bell, G. I. *Science* **1978**, 200, 618.

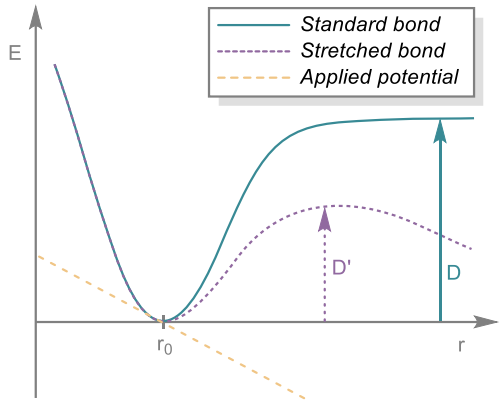

Scheme 2. Representation of a Morse type potential for a standard bond (turquoise) and a stretched bond (purple) created by the application of a force (yellow).

The assumption of a linear dependance of the activation energy with the force employed in the Bell model fails when we are in a high force regime. In those cases, the reduction of the activation energy due to the force is overestimated. This issue was more accurately addressed in the extended Bell theory (EBT), where higher order effects on the activation energy were considered.[15] However, to accurately describe high force regimes it is necessary to introduce distortions on the geometry of molecules due to the external force.

The titled potential energy profile model (t-PEP)[16] was the first strategy in introducing, albeit in an approximate manner, the distortion of molecular geometries. In a way similar to the Bell theory, the t-PEP model considers the effect of the force on a single reaction coordinate, ξ. However, in this case, the effect of the external force is incorporated in a more elaborated manner: a distortion of the reaction coordinate. From a mathematical point of view this

15 Konda, S.S.M.; Brantley, J.N.; Bielawski, C.W.; Makarov, D.E. *J. Chem. Phys*. **2011**, 135, 164103.

16 Evans E.; Ritchie, K. *Biophys. J*. **1997**, 72, 1541–1555.

can be described as shown in Equation 2, the full derivation of the equation can be found in reference 12b.

$$\Delta G^{\ddagger}_{t-PEP}(F_0) = \Delta G^{\ddagger}(F_0 = 0) - \int_0^{F_0} \Delta\xi \, dF \qquad (2)$$

This model can be graphically represented as shown in Scheme 3. The modified $\Delta G^{\ddagger}$ for the t-PEP model consists in a force-free activation energy that is obtained upon the projection of the reactant and transition state on the distorted tilted PEP.

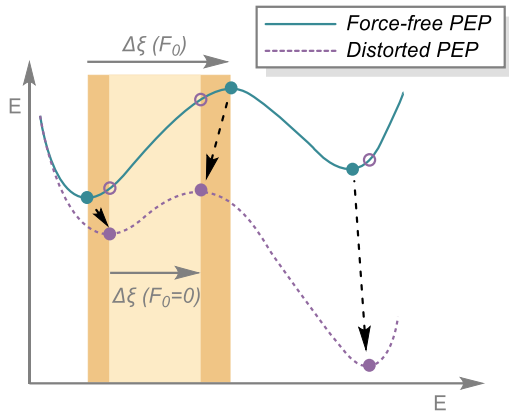

Scheme 3. Representation of the effect of an external force to the energetic profile in accordance with the t-PEP model.

The t-PEP is an effective model for those reactions that can be described within a single dimension. However, the method is not able to describe a multidimensional deformation of the Potential Energy Surface (PES). In those reactions where a one-dimensional treatment is not sufficient, the t-PEP model is doomed to fail. The limitations of the above-mentioned methods motivated the development of first-principle models, which can be generally divided on *isometric* and *isotensional* approaches. Both approaches describe an idealised situation in which either the bond distance is fixed and the force is the variable measured (*isometric*) or *vice versa* (*isotensional*). Both methods have been

widely used, separately or combined, to describe mechanochemical reactions and their use is still active in the field.[17]

The *isometric* category is represented by the Constrained Geometries Simulate External Force (COGEF) method.[18] This approach is based on the calculation of a series of constrained optimizations (with a fixed bond distance), which conform a strained PES. Then, one can explore the amount of force required to perform a specific elongation of the bond and thus evaluate the mechanical strength of a bond.

For the case of the *isotensional* strategies, several approaches have been developed,[19] the principal ones being the Force-Modified Potential Energy Surface (FMPES)[20] and the External Force is Explicitly Included (EFEI).[21] Although they present slight differences, both are built on the so-called the *force-transformed potential energy surfaces* formalism. This formalism is based on the application of an external force in a multidimensional space, which is represented as a series of unit vectors for the number of atoms experiencing the force (Equation 3).

$$F^{ext} = \sum_{i=1}^{N} F_0 n_i \qquad (3)$$

17 (a) Dopierlaski, P.; Ribas-Arino, J.; Anjukandi, P.; Krupicka, M.; Marx, D. *Nat. Chem.* **2017**, 9, 164.

18 M. K. Beyer, J. Chem. Phys., 112, 7307–7312 (**2000**). The Mechanical Strength of a Covalent Bond Calculated by Density Functional Theory.

19 Ong, M. T.; Leiding, J.; Tao, H.; Virshup, A. M.; Martinez, T. J. J. Am. Chem. Soc. 2009, 131, 6377. (b) Wolinski, K.; Baker, J. Mol. Phys. 2009, 107, 2403. (c) K. Wolinski and J. Baker, Mol. Phys., 108, 1845–1856 (2010). Geometry Optimization in the Presence of External Forces: A Theoretical Model for Enforced Structural Changes in Molecules.

20 M. T. Ong, J. Leiding, H. Tao, A. M. Virshup, and T. J. Martínez, J. Am. Chem. Soc., 131, 6377–6379 (2009). First Principles Dynamics and Minimum Energy Pathways for Mechanochemical Ring Opening of Cyclobutene.

21 Ribas-Arino, J.; Shiga, M.; Marx, D. Angew. Chem., Int. Ed. 2009, 48, 4190.

Where the unit vector n_i is defined between a specific atom *i*, denoted as attachment point (AP), and a fixed point in the space, named pulling point (PP) as shown in Equation 4.

$$n_i = \frac{R_i^{PP} - R_i^{AP}}{\|R_i^{PP} - R_i^{AP}\|} \quad (4)$$

These first-principle methods have been further combined with ab initio molecular dynamics to include finite-temperature effects and thus to free energies.[22] However, these advanced methods are outside the scope of the chapter and will not be discussed here. Overall, all the strategies described above, have been applied to a wide range of mechanochemical systems leading to a better understanding of this reactivity.

It is important to mention here that in contrast to other activation modes represented by a scalar magnitude, such a temperature, the mechanical force is a vector. Therefore, the computational treatment of the mechanical input is straightforward for those mechanochemical reactions involving a directional force. Indeed, the above-described techniques are perfect for this purpose. However, when dealing with reactions induced by an isotropic force, the treatment becomes more complex since we should represent as many vectors as possible directions the force can take, which is by far bigger that what we can assume. This is the case of ball milling reactions, a specific class within the trituration type, which is the most employed in synthesis for its simplicity and versatility.[23]

22 Marx, D.; Hutter, J. (2009) *Ab Initio Molecular Dynamics: Basic Theory and Advanced Methods*, Cambridge University Press: Cambridge.

23 For comprehensive reviews in the topic see: (a) James, S.L.; Adams, C.J.; Bolm, C.; Braga, D.; Collier P.; Friščić, T.; Grepioni, F.; Harris, K.D.M.; Hyett G.; Jones, W.; Krebs, A.; Mack, J.; Maini, L.; Guy Orpen, A.; Parkin, I.P.; Shearouse, W.C.; Steedk, J.W.; Waddelli, D.C. *Chem. Soc. Rev*., **2012**, 41, 413–447. (b) Boldyreva, E. *Chem. Soc. Rev.*,

As other mechanochemical techniques, ball milling reactions are affected by a wide range of variables.[24] Whereas in some cases the different parameters can be used to tune the reactivity, in other situations they might impede the reproducibility of the results. For example, the equipment is usually not standardised; the material employed can affect the kinetic energy of the collisions and in some cases, it can dramatically alter the outcome of the reaction due to leaching of metal ions that lead to uncontrolled catalysis inside the milling jar.[25] Apart from the milling equipment it is important to bear in mind the operating conditions; the frequency employed,[26] the ball-to-reagent ratio[27] and the use of LAG auxiliaries,[28] since all of these parameters can also have a wide impact on reactivity.

Since ball-milling reactions are used mostly for synthesis, they tend to be compared with solution chemistry. [29] In this regard there is an extended disagreement within the community; some advocate for the enormous differences between the methods, others focus on the similarities. To shed light

---

2013,42, 7719-7738. (c) Tan, D.; Friščić, T. *EurJOC*, **2018**, 1, 18-33. (d) Leonardi, M.; Villacampa, M.; Menéndez, J. C. *Chemical Science*. **2018**, 9, 2042.

24 Tan, D.; García, F. *Chem. Soc. Rev*., **2019**, 48, 2274-2292.

25 Andersen, J.M.; Mack, J. Chem. Sci. **2017**, 8, 5447.

26 (a) McKissic, K.S.; Caruso, J.T.; Blairb, R.G.; Mack, J. *Green Chem.* **2014**, 16, 1628. (b) Schmidt, R.; Burmeister, C.F.; Baláž§, M.; Kwade, A.; Stolle, A. *Org. Process Res. Dev*. **2015**, 19(3), 427. (c) Julien, P.A. ; Malvestiti, I. ; Friščić, T. *Beilstein J. Org. Chem*. **2017**, 13, 2160. -actualitzar

27 Kulla, H.; Fisher, F.; Benemann, S.; Rademann, K.; Emmerling, F. *CrystEngComm,* **2017**, 19, 3902-3907.

28 (a) Bowmaker, G.A. *Chem. Commun*., **2013**, 49, 334-348. (b) Konnert, L.; Dimassi, M.; Gonnet, L.; Lamaty, F.; Martinez, J.; Colacino, E. *RSC Adv*. **2016**, 6, 36978. (c) Howard, J. L. ; Sagatov, Y. ; Repusseau, L. ; Schotten, C. ; Browne, D.L. *Green Chem.* **2017**,19, 2798.

29 (a) Hernández, J.G.; Bolm, C. *J. Org. Chem.* **2017**, 82, 8, 4007–4019 (b) Howard, J.L.; Cao, Q.; Browne, D.L. *Chem. Sci*. **2018**, 9, 3080-3094.

on this issue, it is necessary to gain more insights on ball-milling reaction mechanisms. In this sense, experimental chemistry has provided extremely useful information through both *in situ* and *ex situ* monitoring techniques.[30] The most widely applied methods have been powder X-ray diffraction (PXRD), infrared (IR) and Raman spectroscopy. X-ray diffraction is used for the characterisation of crystalline powders; the technique allows the determination of structures without the need to grow diffraction-quality crystals.[31] However, the partial amorphization usually associated to the grinding process usually precludes the use of PXRD techniques in ball-milling reactions, specifically for organic synthesis. In these cases, IR, and Raman spectroscopy are employed. These techniques permit the identification of covalent bond scission/formation. Moreover, they are available in most laboratories and thus, are more readily accessible.

These studies are mostly performed *ex situ i.e.*, the analysis is performed in a stepwise manner, first the milling and then the measurement (Figure 1).[32]

30 Do. J.L.; Friščić, T. *CS Cent. Sci.* **2017**, 3(1), 13–19.

31 Michalchuk, A.A.L.; Tumanov, I.A.; Boldyreva, E.V. *CrystEngCom*, **2019**, 21(13), 2174-2179.

32 (a) Ma, X.H.; Yuan, W.B.; Bell, S.E.J; James, S.L. *Chem. Commun*. **2014**, 50, 1585. (b) Caira, M.R.; Nassimbeni, L.R.; Wildervanck, A.F. *J. Chem. Soc. Perkin Trans.* **1995**, 2, 2213. (c) Harris, K.D.M. *Nat. Chem*. **2013**, 5, 12. (d) Rojac, T. ; Malic, B. ; Kosec, M. ; Polomska, M. ; Hilczer, B. ; Zupancic, B. ; Zalar, B. *Solid State Ionics* **2012**, 215, 1. e) Fischer, F.; Scholz, G.; Benemann, S.; Rademann, K.; Emmerling, F. *CrystEngComm.* **2014**,16, 8272.

However, lately *in situ* X-ray[33] and Raman[34] techniques have been developed allowing to conduct the measurement without interrupting the milling process and so, permitting the analysis of the evolution of the reaction inside the milling jar in real time.[35] Apart from the spectroscopic techniques, *in situ* monitoring is also employed for the investigation of temperature and pressure inside the milling jar. [36]

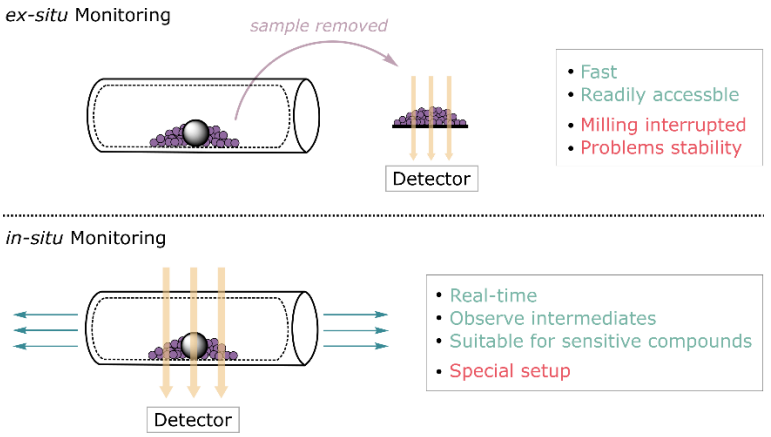

Figure 1. Representation of ex-situ and in-situ monitoring with the advantages and disadvantages of the techniques.

33 Friščić, T.; Halasz, I.; Beldon, P. J.; Belenguer, A. M.; Adams, F.; Kimber, S. A. J.; Honkimaki, V.; Dinnebier, R. E. *Nature Chem.* **2013,** *5*, 66. (b) Halasz, I.; Kimber, S. A. J.; Beldon, P. J.; Belenguer, A. M.; Adams, F.; Honkimaki, V.; Nightingale, R. C.; Dinnebier, R. E.; Friščić, T. *Nat. Protoc.* **2013**, *8*, 1718. (c) Lampronti, G.I.; Michalchuk, A.L.A.; Mazzeo, P.P.; Belenguerb, A.M.; Sandersb, J.K.M.; Bacchid, A.; Emmerling, F. arXiv: 14034623, **2021**.

34 Gracin, D.; Štrukil, V.; Friščić, T.; Halasz, I.; Užarević, T. *Angew. Chem.Int. Ed.* **2014**, *53*, 6193.

35 (a) Batzdorf, L.; Fischer, F.; Wilke, M.; Wenzel, K.-J.; Emmerling, F. *Angew. Chem. Int. Ed*. **2014**, 54 (6), 1.(b) Štrukil, V.; Gracin, D.; Magdysyuk, O.V.; Dinnebier, R.E.; Friščić, T. *Angew. Chem. Int. Ed.* **2015**, 54, 8440.

36 Užarević, K.; V.; Mottillo, C.; Julien, P.A.; Puškarić, A.; Friščić, T.; Halasz, I. C*ryst. Growth Des.* **2016**, 16, 4, 2342–2347.

Although *in situ* techniques enable to gather extensive knowledge on mechanochemical reactions, they are not frequently used, largely due to the limited and expensive character of the method. Thus, the development of more accessible *in situ* monitoring techniques would represent a boast on the mechanistic understanding of ball milling reactivity.

From a computational perspective, these reactions are largely understudied. Some investigations focus on the simulation of the motion in milling processes with special attention to breakage processes.[37] However, when it comes to reactivity inside ball-mills, a proper description is lacking. Some studies use the computational methods explained above, others use standard DFT calculations involving a gas phase medium, albeit without paying much attention to the computational method.[38] Therefore, efforts must be directed towards the unification of the computational treatments as well as the combination of theory and experiments to assist a faster development of this interesting synthetic strategy.

37 Tavares, L. M. *KONA Powder Part. J.* **2016**, 106-124.

38 (a) Krištofíková, D.; Mečiarová, M.; Rakovský, E.; Šebesta**, R.** *ACS Sustainable Chem. Eng.* 2020, 8, 38, 14417–14424.

2. Objectives

During the last decade, we have observed a steady growth in the utilization of mechanochemical techniques. Still, progress in the area remains slow, largely due to the little understanding of its underlying reaction mechanisms. The intrinsically interdisciplinary nature of the field, and the broad spectrum of reactions covered by the "mechanochemistry" concept, hampers the achievement of a unified picture of these force-assisted reactions.

In the literature one can find diverse computational techniques for the calculation of mechanochemical reactions which simulate the effect of a directional forces to a target molecule. However, there is to our knowledge a lack of methods to study the effect of a non-directional force applied to the system, as it happens in ball-milling techniques.

In this context, we aimed to develop a computational approach for the rationalization of ball milling mechanochemical processes. Thereby, contributing to the understanding of ball milling reaction mechanisms, we expect to assist in the advancement of the field.

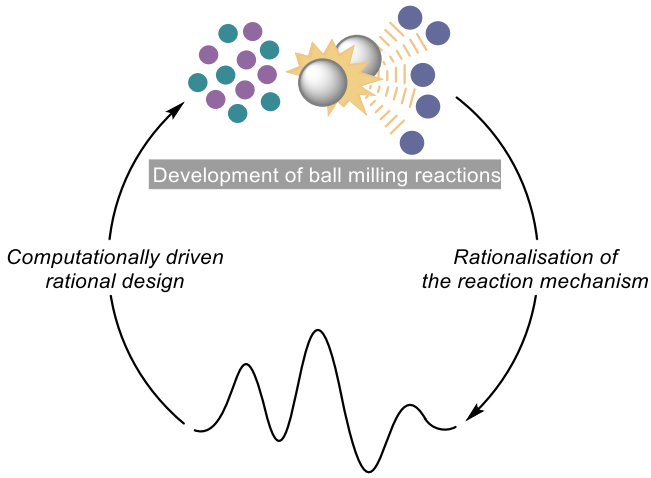

Scheme 4. Computationally driven rational design of ball milling reactions based on mechanistic understanding.

3. Methodology

From now on, any term related to mechanochemistry mentioned throughout the chapter will refer to ball milling, unless otherwise stated.

As mentioned above, there is a division within the community working on ball-milling reactions. On one side, there have been many efforts on pointing out the differences between mechanochemical reactions and solution-based processes to emphasize the extremely different nature of the transformations.[30] On the other side, the attention has been directed towards the similitudes. Indeed, when comparing the reaction outcome between both methodologies, the similarities between them are remarkable. Most reactions present merely a decrease on the reaction time, others slight differences on selectivity, and lastly there are some cases, albeit far less common, where completely different reactivity has been observed. However, when we analyze these cases, most of the times, we can find alternative and simple explanations to rationalize these differences.

In our point of view, and bearing these significant similarities in mind, it seems counterintuitive to consider ball milling reactions as completely different transformations to solution processes. Thus, we have tackled ball milling reactions as a variant of solution reactions, focusing on how the system is modified by the mechanical force rather than on the specific mechanical interactions.

Our key hypothesis is that the role of the isotropic mechanochemical grinding is the mixing of the reacting species, and that otherwise the process is quite similar to those in solution. The caveat is that there are significantly different sets of concentrations and dielectric environment, which may affect the reaction output. Therefore, mechanochemical reactions could be reproduced through the incorporation of these parameters to the standard DFT tools. We are fully aware that there are other peculiarities of the mechanochemical

process that are relevant and may play a mechanistic role, such as grinding frequency, the vial material or interactions between the reactants and the ball surface. However, our idea here is to start with a simple approach and evaluate how far it can take us.

The strategy will be composed by the three steps shown in Scheme 5. First the mechanism elucidation with a specific dielectric environment. Then a microkinetic study in which the concentrations are included. Finally, the proposed hypothesis is evaluated by comparing the results with experimental data. To be able to confirm the validity of the methodology is necessary to start with simple reactions that carry a defined mechanism, this strategy avoids error sources that could arise from an incorrect mechanism. We have selected three simple organic reactions: Diels-Alder, N-sulfonylguanadine synthesis and Brady reaction that will be discussed in the following sections.

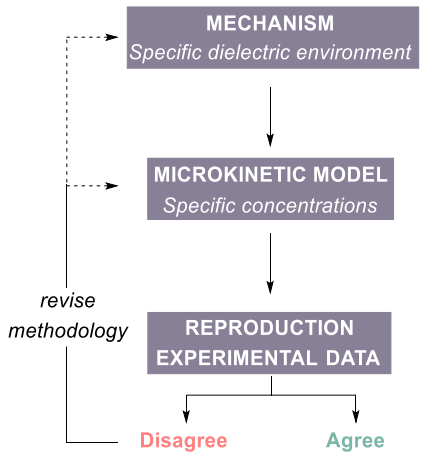

Scheme 5. Steps followed to define the strategy for the calculation of ball milling reactions.

Prior to the validation of the methodology, we must define the different approaches for the evaluation of the dielectric environment and the concentrations:

Dielectric environment

Mechanochemical reactions occur in the absence of solvent, therefore, the first great unknown is the proper way to model the environment. We have considered two different approaches to implement the medium of mechanochemical reactions:

(i) Vacuum

The first approximation is to use gas phase calculations; this treatment is employed since most mechanochemical reactions occur between two solid reagents; owing to the rigid nature of solid species, the molecules are presumably in contact with the other reactant molecules and air.

(ii) Solvation cage-like medium

The second approximation considers that, the environment of a mechanochemical reaction is defined by its own reagents and, when applicable, the liquid assisted grinding (LAG) additive. This treatment assumes that when mechanochemical conditions are applied, the high frequency stirring the mixture and the high concentration of reactants would generate a solvent cage-like medium. This medium can be seen as a pseudo-fluid generated by all the species in the reaction media.

To model this hypothesis, we have customized the PCM implicit solvation model, to define the medium created by the reactants. The PCM methodology has been selected since it can be defined with two relatively accessible parameters: the dielectric constant (ε) and the infinite dielectric constant (ε^{∞}). Figure shows the keywords required to define a customized PCM solvent with ε and ε^{∞} in a Gaussian input.

```
# scrf=(solvent=generic,read)
(XYZ coordinates)
solventname = Name of the solvent
eps = Dielectric constant
epsinf = Infinite dielectric constant
```

Figure 2. Keywords employed to define a customised PCM model in a Gaussian input.

The infinite dielectric constant can be computed as the square power of the refracting index. Both values for the refracting index and dielectric constants can be usually extracted from the literature. In those systems where different dielectric environments were mixed, *e.g.*, reactant 1, reactant 2 and LAG, the resulting dielectric constant was computed using the method reported by Prakongan and Nagai in 1984 shown in Equation 5. The same procedure was employed to weigh the refracting index of the different species.

$$\varepsilon_M = \sum \phi_n \, \varepsilon_n \tag{5}$$

where Φ_n is the molar fraction of each component, ε_n their dielectric constants and ε_M the dielectric constant of the mixture.

Concentration

The other critical parameters that affect the mechanochemical reactions are the concentrations. Although the calculation of concentration is generally straightforward, in mechanochemical reactions, the absence of solvent complicates the definition. We have estimated them by extrapolation from the density of the reagents (Equation 6).

$$C_A = \frac{n_A \rho_T}{m_T} \tag{6}$$

where, ρ_T corresponds to:

$$\rho_T = \frac{\sum_{i=0}^{i=n} m_i \rho_i}{m_T} \quad (7)$$

and m_T corresponds to:

$$m_T = \sum_{i=0}^{i=n} m_i \quad (8)$$

Throughout this approximation we set ourselves on an ideal system where a complete homogenization has been achieved. We know that this is not an exact approach, but we consider it introduces a substantial feature of the mechanochemical environment.

4. Calculations on a Diels-Alder reaction

Experimental overview

Diels-Alder reactions are among the most important transformations in organic chemistry. They have been applied to a large number of procedures for the synthesis of ellaborate compounds as well for the industrial production at a large scale. In 2017 Andersen *et al.* reported a mechanochemical investigation on a set of six Diels-Alder reactions constituted by all the combinations between two dienophiles; benzoquinone (BQ) and maleic anhydride (MA), and three dienes; anthracene (H9), 9-methylanthracene (MA9) and 9,10-dimethylanthracene (DMA). These reactions were chosen because they span a wide range of yields, with reactions achieved easily at room temperature and others providing no conversion (Scheme 6).

Their study aimed to shed light on mechanistic aspects of mechanochemical transformations. In particular, the authors were interested on the rationalization of the effect of frequency, temperature, and vial material on the yield. Hence, they performed a systematic investigation in which these parameters were modified and their effect to the reaction yield was carefully examined. Note

that the operating temperature in all the reactions described is 36 ºC at 15 Hz, with an increase up to 2 ºC when the reaction is performed at 21 Hz.

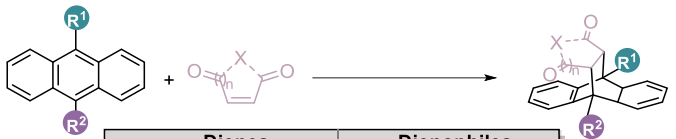

Dienes	R^1	R^2	Dienophiles
H9:	H	H	**MA:** Maleic anhydride
MA9:	H	CH_3	**BQ:** Benzoquinone
DMA:	CH_3	CH_3	

Scheme 6. Set of Diels-Alder reactions studied by Andersen *et al.* with mechanochemical techniques.

First, they studied the effect of frequency and the vial material on the reaction outcome. They observed an exponential growth of the conversion with the frequency (Figure 3, left) and a substantial effect arising from the choice of vial material going through teflon (PTFE), unhardened steel (UHS), stainless steel (SS), and hardened steel (HS) (Figure 3, right).

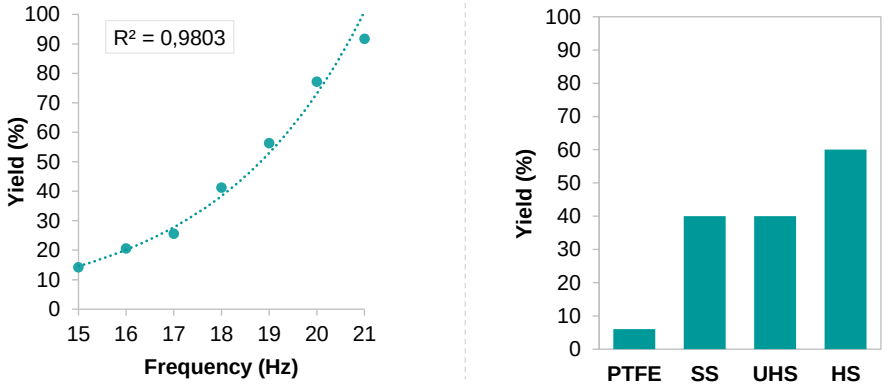

Figure 3. Systematic investigations based on the DMA-9 and BQ reaction. Left: exponential grow of the conversion with the frequency with SS vial. Right: effect of the vial material to the conversion.[39]

39 When reproducing the graph, we have seen a slight discrepancy on the R2, however it does not have any effect on the overall conclusion.

With this information in hand, they proceeded to select three different frequencies (15, 18 and 21 Hz) and three different vial materials (PTFE, SS and HS) and studied the differences caused, by these variables, on the yield after 3h of reaction. The experimental data was complemented with DFT gas phase calculations of the potential energy barrier associated with the corresponding transition states (Figure 4). The calculations reproduced qualitatively the trends in reactivity, hence they were employed to distinguish between the Diels-Alder reactions.

The reactions with lower energy barriers (DMA-MA and MA-MA) gave a 100% yield within all conditions. Those with higher barriers (H9-MA and H9-BQ) yielded no conversion. On the other hand, the reactions with intermediate barriers were highly affected by the conditions, with changes from 100% to 0% yield for the DMA-BQ system and from 27% to 0% for MA-BQ.

With the information extracted they divided the mechanochemical reactions on three regions: (*Region I*) thermally-driven region, in which all the reactions are allowed due to low barriers; (*Region II*) collisionally-driven region, in which the frequency and the milling container affect the yield obtained; and (*Region III*) conditionally-forbidden region, in which the barrier for the reaction was too high for the reaction to proceed.

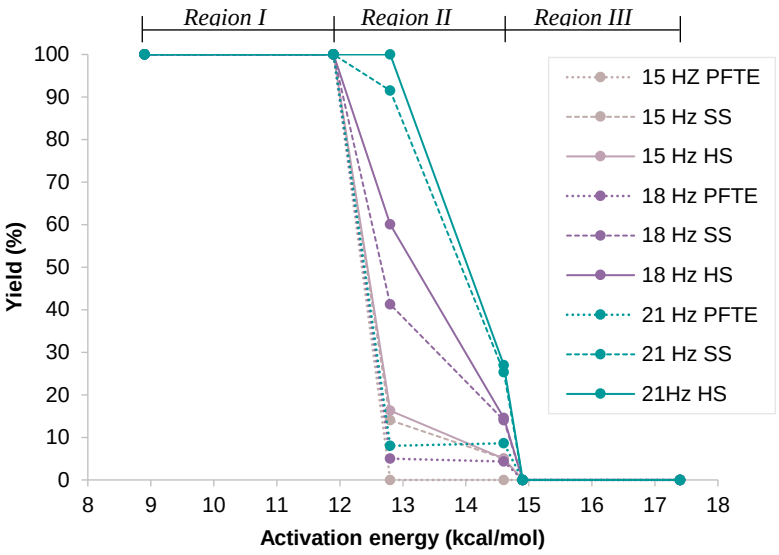

Figure 4. Yields reported by Andersen *et al*. for the set of Diels-Alder reactions at different reaction conditions (variations on frequency and vial material).

Then, they examined the temperature dependence of three reactions that did not achieve full conversion with the initial temperature: two in the conditionally forbidden region (H9-MA and H9-BQ) and one in the collisionally-driven region (MA-BQ). All reactions achieved a quantitative conversion when the temperature was increased (Figure 5). They also compared the results obtained for the mechanochemical reaction H9-BQ with the equivalent reaction in solution. While under mechanochemical conditions the transformation is achieved at ~100ºC, in solution it is necessary to reach ~140ºC (refluxing xylene), demonstrating a significant boost on the reaction rate when mechanochemical conditions are employed. Overall, in their work, Andersen *et al*. highlighted the power of mechanochemistry to modify reaction times and pointed a similarity between the mechanism in mechanochemical conditions and that in solution.

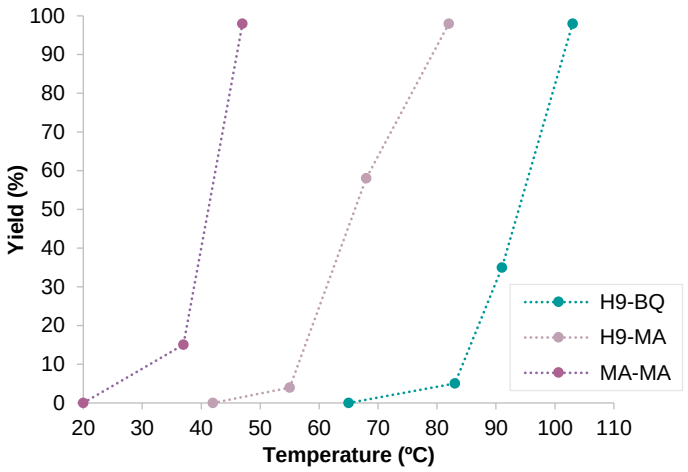

Figure 5. Dependence of the yield with the temperature from left to right; MA-BQ, H9-MA and H9-BQ reaction.

Computational details

All calculations were carried out using Gaussian09 (Rev. D.01) package. To select the level of theory, we performed a benchmarking which included the mPW1PW91, ωB97x-D, M06, M06-2X, BP97, M06-D3 and B3LYP-D3 functionals (D3 states for Grimme-D3 dispersion corrections), with 6-31+G(d) and 6-311++G(d,p) basis sets (subsection "Benchmarking"). The B3LYP-D3 functional, was selected together with a 6-311++G(d,p) basis set. All geometries were optimized without symmetry restrictions and vibrational frequency calculations were computed for all stationary points to confirm their nature as minima (zero imaginary frequencies) or as transition states (one imaginary frequency). Solvation effects were introduced implicitly through the PCM model, which has been customized to introduce the dielectric environment provided by the mixture of the reagents. The values used for both dielectric constants and infinite dielectric constant are depicted in the subsection "Customization of the PCM model". The reported energies are free energies in solution or gas phase (as specified throughout the text) at 311 K and 1 M, unless otherwise specified. Microkinetic simulations were carried out

using the COPASI 4.22 program; the values for the concentrations used in the model are depicted in the subsection "Concentrations". A data set collection of all computed structures is available in the ioChem-BD repository.

Benchmarking

The selection of the proper functional is very important for DFT calculations, especially when applying microkinetic models, as these are highly sensible to small variations on the level of theory. Moreover, as Andersen *et al.* performed a computational investigation with the mPW1PW91 functional, we wanted to compare its performance with that of other methods. Notice that whereas in the original work the authors used the calculations for a qualitative description of the system, and therefore, they reported potential energies; in our investigation we aim to obtain quantitative reproduction of experimental reaction times. This requires the implementation of a microkinetic model, and consequently the use of free energy barriers. Therefore, the benchmark has been done through the free energy barriers of the six Diels-Alder reactions; the results are collected in Table 2 and Table 3.

Table 2. Comparison of the activation barrier for ωB97xD, B3LYP-D3, M06, M06-2x and mPW1PW91 functionals for the set of Diels-Alder reaction with 6-31+g(d,p) basis set. Energies are free energies in kcal/mol.

6-31+g(d,p)		H9-BQ	H9-MA	MA9-BQ	DMA-BQ	MA9-MA	DMA-MA
ωB97xD	Vacuum	25.8	23.2	22.8	22.0	19.9	17.9
	Solid Average	26.8	23.2	22.2	20.2	17.9	16.4
B3LYP-D3	Vacuum	25.8	23.8	23.1	22.8	20.9	18.4
	Solid Average	26.6	23.3	22.2	21.7	18.5	16.8
M06	Vacuum	24.4	23.3	21.8	19.5	19.6	15.7
	Solid Average	24.7	23.9	20.3	18.6	17.7	16.2
M06-2x	Vacuum	23.0	21.8	21.3	19.7	19.1	16.6
	Solid Average	24.7	22.5	20.9	18.4	17.6	16.1
mPW1PW91	Vacuum	30.0	27.6	28.6	27.7	26.2	23.9

Table 3. Comparison of the activation barrier for ωB97xD, B3LYP-D3, M06-D3 and B97D functionals for the set of Diels-Alder reaction with 6-311++g(d,p) basis set. Energies are free energies in kcal/mol.

6-311++g(d,p)		H9-BQ	H9-MA	MA9-BQ	DMA-BQ	MA9-MA	DMA-MA
ωB97xD	Vacuum	23.9	23.9	23.2	23.2	20.9	18.1
	Solid Average	27.4	23.3	23.3	21.5	18.4	17.5
B3LYP-D3	Vacuum	26.3	24.5	23.9	23.7	21.9	19.3
	Solid Average	27.3	23.8	23.0	22.7	19.1	18.2
M06-D3	Vacuum	24.8	22.0	21.9	21.0	19.8	18.4
	Solid Average	27.3	22.0	20.9	19.6	16.4	17.1
B97D	Vacuum	23.1	22.0	20.6	21.0	18.9	16.9
	Solid Average	24.0	21.3	19.7	19.9	17.1	15.8

There are minor differences between the selected functionals or basis sets, with the exception of the mPW1PW91 functional which shows substantial higher activation energies. These results are analysed in more detail in the subsection *"Comparison with calculations in the experimental publication"*. Although the other methods present small energy differences, in some cases we observe substantial differences on the qualitative picture *i.e.*, different order on the activation energies. According to the experimental work, the reactions should be ordered from easier to more difficult as: DMA-MA, MA9-MA, DMA-BQ, MA9-BQ, H9-MA and H9-MA. However, this order is not respected with the M06, mPW1PW91 and B97D functionals. For example, the B97D functional predicts a lower barrier for MA9-BQ than for DMA-BQ. We can also observe small energy differences between vacuum and solid average methods, the comparison between the approaches is discussed in the subsection *"Application of the methodology"*. After the benchmarking, the B3LYP-D3 functional with 6-311++g(d,p) basis set was selected as level of theory because it provides the best agreement with experiment.

Customization of the PCM model

To define a PCM model for a solvent that is not included in the options offered by Gaussian, we need to use its dielectric constant and the refracting index. Table 4 depicts the values, (extracted from the literature) of the two parameters for benzoquinone, anthracene, and maleic anhydride. Please notice that since the dielectric constants and refracting indexes for all the dienes are similar, we have used the values for anthracene in all the reactions.

Table 4. Dielectric constants and refracting indices used for the implementation of the solvent cage-like medium.

Compound	Dielectric constant (ε)	Refracting index (*n*)
Benzoquinone	3.1	1.453
Maleic anhydride	51.0	1.515
Anthracene	2.4	1.595

With the values of the dielectric constants and the refracting index we proceeded to calculate the solvent features, following the strategy explained in the methodology section (Table 5). Please notice that two different solvent media have been employed: when the dienophile is benzoquinone, we use mix_BQ and when it is maleic anhydride mix_MA. Indeed, the large difference between their dielectric constants could significantly affect the reaction outcome.

Table 5. Dielectric constants and refracting indexes applied as "solid average" in the reactions.

Solvent	Dielectric constant (ε)	Inf. dielectric constant (ε^{∞})
mix_MA_rxn1	26.7	1.556
mix_BQ_rxn1	2.7	1.459

Concentration

The concentrations obtained for the set of Diels-Alder reactions were calculated following the strategy explained in the methodology section. The results are presented in Table 6. In all cases, the mixture is stoichiometric, with the same number of moles for both reactants.

Table 6. Concentrations (M) used for the calculation of the different Diels-Alder reactions in mechanochemical conditions.

Reaction studied	Concentration (M)
H9-BQ	2.74
H9-MA	2.72
MA9-BQ	2.88
DMA-BQ	2.86
MA9-MA	2.74
DMA-MA	2.72

Results and discussion

Application of the method

Based on the experimental data from Andersen *et al*. article, we applied of the previously described method to the set of Diels-Alder reactions. The mechanism was investigated considering two possible dielectric environments: vacuum or solid average. As expected, the pericyclic reaction takes place in a single step, and the transition state shows a rather unremarkable concerted arrangement, as shown in Scheme 7.

With the mechanism in hand, we converted the free energy barriers into rate constants that together with the computed concentrations (see section Concentrations) were introduced into a microkinetic model. The results for both approaches (vacuum and solid average) are reported in **Figure** together with the collection of experimental data at three different frequencies (15, 18, 21 Hz). It is important to mention here that the obtained mechanochemical concentrations are between 2 and 3M for each of the reactant, if we had used typical values for the concentration of reactants in organic solution, the reaction times would have been much longer. This is likely to be a general feature of

mechanochemical processes, an acceleration because of the increased concentrations.

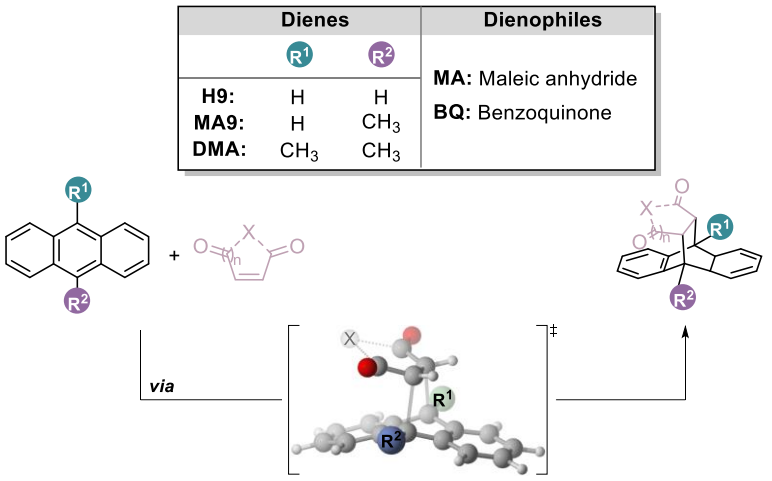

Scheme 7. Diels-Alder reactions studied by Andersen *et al.* with mechanochemical techniques and general picture of the 3D transition state involved on the transformations.

Both dielectric environments produce similar results for this specific system. This is consistent with the low sensitivity of the Diels-Alder reaction to the medium due to the small change in charge distribution throughout the process. The most significant result from Figure 6 is in any case the good overall agreement between calculation and experiment. There is a clear gradation in yields that follows the experimental trends, with DMA-MA and MA9-MA producing the highest yields, and H9-BQ and H9-MA producing the lowest ones. The quantitative agreement is also reasonable, with values close to 100% for the fastest systems, values close to 0% for the slowest ones, and intermediate values for the others. These intermediate values are of course the most difficult to reproduce, as this is the situation where the exponential dependence in the Eyring equation comes into play, and hence the predicted yield is very sensitive to the computed barrier. It would not be realistic to expect

a better quantitative agreement considering that we do not introduce the milling frequency in our calculations, even if we believe it is strongly related with concentrations *i.e.*, the frequency modifies the homogenization of the system.

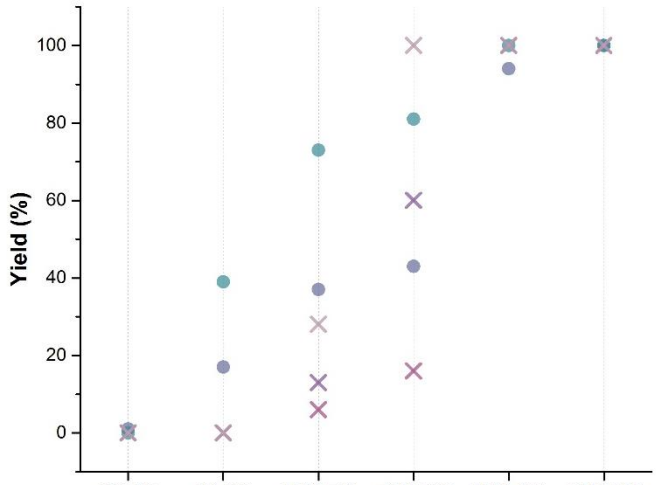

	H9-BQ	H9-MA	MA9-BQ	DMA-BQ	MA9-MA	DMA-MA
15 Hz HS	0	0	6	16	100	100
18 Hz HS	0	0	13	60	100	100
21 Hz HS	0	0	28	100	100	100
Vacuum	0	17	37	43	94	100
Continuum	0	39	73	81	100	100

Figure 6. Reported experimental yields together with our computed yields for the Diels-Alder reactions.

Comparison with calculations in the experimental publication

After demonstrating the remarkable agreement between our calculations and the experimental results, we wanted to compare the values with the mPW1PW91 functional applied in the experimental publication. The results (shown in Table 7) show that if we had used directly the raw DFT values supplied in the experimental publication, the agreement in terms of reaction yield would have been very poor. There are two problematic issues with respect to the method utilized in the experimental article: first, the need to introduce entropic corrections leads to a modification on the qualitative agreement by switching the order of the experimentally observed trends for DMA-BQ, MA9-

MA and H9-MA reactions. Then, the free energy barriers obtained are quite high in comparison with other functionals, as highlighted in the Benchmarking section. This leads to 0% conversion for most of the reactions, even if we consider the high concentrations of mechanochemical systems. This further evidences that the reproduction of reaction times is much more challenging than reproducing qualitative trends in barriers. Thus, we must pay special attention in the selection of the method since it can drastically modify the results.

Table 7. Values of concentrations, ΔG, rate constant, $t_{1/2}$ and yield used for the kinetic study of the Diels-Alder reaction with mPW1PW91 functional.

	Concetration (M)	ΔG (kcal/mol)	Rate constant (s^{-1})	$t_{1/2}$ (h)	Yield (%)
H9-BQ	2.74	30.0	$6.04 \cdot 10^{-10}$	167816	0
H9-MA	2.72	27.6	$3.65 \cdot 10^{-8}$	2797	0
MA9-BQ	2.88	28.6	$6.75 \cdot 10^{-9}$	14288	0
DMA-BQ	2.86	27.7	$3.08 \cdot 10^{-8}$	3150	0
MA9-MA	2.74	26.2	$3.88 \cdot 10^{-7}$	261	1
DMA-MA	2.72	23.9	$1.88 \cdot 10^{-5}$	5	36

Milling frequency

The general reproduction of experimental results allows a deeper analysis of our computational results in connection with other reaction features, using the wealth of data supplied in the original experimental work. We will first focus on the role of the frequency of ball milling in the reaction yield, and how we can take this into account in our computational model. As explained in the experimental overview section, Andersen *et al.* performed a series of experiments with different milling frequencies where they measured the yield at a given time, which was therefore constant. They found an empirical dependence between yield (y) and milling frequency (ν) of an exponential nature, Equation (1):

$$y = A \exp(\alpha v) \quad (1)$$

where A, α are a preexponential factor and a multiplier to the exponent. The exponential fit indicates a first order dependence of the yield on the concentration, thus, Equation (2):

$$\frac{dy}{dv} = k_v[A] \quad (2)$$

where k_v is a specific frequency-related rate constant. On one hand, this expression is intuitively logical, the higher frequency should produce a larger amount of accessible reactant, and thus a faster reaction. On the other hand, a first order dependence seems in contradiction with the second order nature of a process involving two reactants, A and B. This contradiction can be solved by assuming that the concentration of the second reactant, B, is independent from the milling frequency. After all, the two solids will have different physical properties, and it can well be the case that each of them has a characteristic range of frequencies where the efficient grinding takes place. In this particular case, we can postulate that B would be already fully homogenized in the range of frequencies considered. Of course, in the absence of more data we cannot identify reactant A as either DMA or BQ.

The explanation above on the role of the milling frequency is fully consistent with our model where we are predicting that the role of the milling is to increase the amount of accessible reactant, thus the effective concentration. The implication of the solid crystal structure further notes one of the general problems on the rationalization of reactions involving solid reagents; the effect of experimental parameters in the solid cannot be elucidated through homogeneous computational treatments.

A last topic we want to mention here is that we used the Eyring-Polany equation, and thus the pre-exponential factor is set to a fixed value. The fact that we reproduce the experimental results without introducing an explicit

dependence of the pre-exponential factor on the milling frequency strongly suggests that, at least in this case, this is not the key difference between mechanochemical reactions and processes in solution.

Temperature

The publication by Andersen and Mack also examined systematically the effect of a second variable, the temperature. They explored its dependence for three reactions (H9-BQ, H9-MA and MA-BQ) within their set. We further studied this temperature dependence computationally for the reaction with the highest activation energy (H9-BQ).

First, we applied a temperature correction to the Gibbs free energies for all the calculations, and then, the resulting rate constants were employed to carry out the microkinetic modelling at the desired temperature. The results obtained from the microkinetic study are shown in Figure 7 together with the experimental temperature dependence of the same reaction.

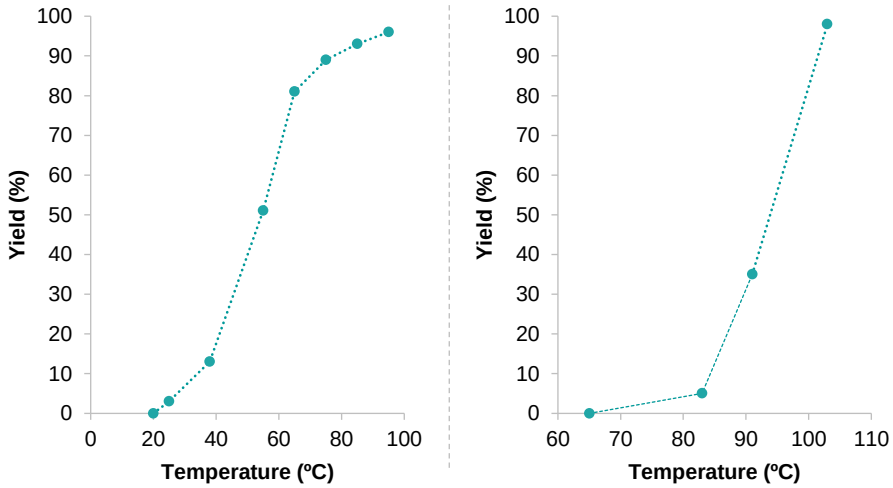

Figure 7. Dependence of the yield with the temperature for the H9-BQ reaction. Left: computational data. Right: experimental data.

Upon the comparison of the two graphs, we observe a similar curve for both experimental and computed data, with a grow from 0% to 90% yield within an approximate range of 40ºC. However, there is a discrepancy on the exact temperature required to perform the transformation. Whereas in the computed curve, the reaction has achieved already a 90% conversion at 70ºC, at the same temperature, in the experimental curve, the conversion is nearly zero. This is attributed to two different facts: (i) underestimation of the barrier with the selected functional and (ii) consideration of an "ideal system" regarding the concentrations, since we assume that the system is fully homogenized during the entire process. Both facts would lead to an underestimation of the time/temperature required to achieve the reaction. However, we claim that the important take-home message of this subsection is the high similarity between the shape of the experimental and the computed curve, pointing towards the proper description of the temperature by the Eyring-Polanyi equation.

The study of this Diels-Alder reactions confirms the validity of our hypothesis: at least some mechanochemical processes follow the same mechanism than in solution, and their behavior can be reproduced by DFT calculations and microkinetic modeling. On the other hand, this particular system was not able to discriminate between the two different models for the theoretical description of the environment.

5. Calculations on the synthesis of N-sulfonylguanidine

Experimental overview

N-sulfonylguanidines are relevant compounds due to their properties as pharmaceuticals, and herbicides. The most usual procedure for their synthesis consists in the C-N coupling of an arylsulfonamide and a carbodiimide. The method has its limitations, mainly in terms of being rather slow; the rather low nucleophilic character of the sulfonamide blocks the reaction in normal conditions. We can overcome this situation and achieve a successful

transformation either by placing specific substituents that present inductive effects or by using a catalyst. For example, the use of a trifluoromethylsulfonamide (**1a**) as a nucleophile has been found to promote the reaction (Scheme 8, A).[40]

In this context, Friščić and co-workers examined the application of ball milling to the N-sulfonylguanidine synthesis.[41] The authors evaluated a variety of conditions, with different sets of reactants. They started with trifluoromethylsulfonamide (**1a**) as a nucleophile, which has been found to be productive under solution conditions, and found analogous reactivity *via* mechanochemical techniques, albeit with a considerable reduction of time (from 12h to 2h). It is worth mentioning that apart from **1a** being the only sulfonamide able to promote the transformation, its reactivity was limited to aliphatic groups on the carbodiimide. Indeed, when aromatic carbodiimides were introduced as coupling partners, the reaction did not reach conversion. Similarly, when other nucleophiles were used, the reaction was not productive in absence of catalyst. However, in such cases, good to excellent yields were obtained upon the introduction of CuCl as catalyst achieving a broader scope for the transformation (Scheme 8, B). This catalytic alternative was also attempted in solution, and no traces of the product were observed, pointing out the need of mechanochemical techniques.

40 a) B. A. Shainyan, L. L. Tolstikova, U. Schilde, J. Fluorine Chem. **2012**, 135, 261; b) L. L. Tolstikova, N. N. Chipanina, L. P. Oznobikhina, B. A. Shainyan, Russ. J. Org. Chem. 2011, 47, 1278.

41 Tan, D.; Mottillo, C.; Katsenis, A. D.; Vjekoslav, S.; Friščić, T. *Angew. Chem. Int. Ed.* **2014**, 53, 9321–9324.

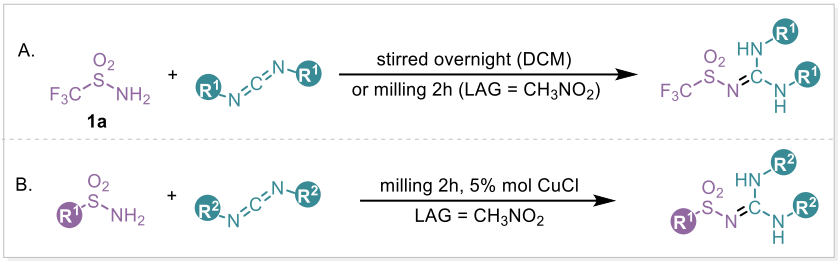

Scheme 8. Synthesis of N-sulfonylguanidine in a) catalyst free conditions and b) 5%CuCl as catalyst.

The N-sulfonylguanidine synthesis is a slightly more complex transformation in comparison to the Diels-Alder process presented in the last section. Besides, this study permits the evaluation of the experimental reaction times for both mechanochemical and solution-based transformations, which show a considerable difference (from 12h to 2h). Therefore, the transformation has been selected as a second system to validate our methodology.

Computational details

All calculations were carried out using Gaussian09 (Rev. D.01) package. The ωB97x-D functional, was used together with the 6-31+G(d) basis set. All geometries were optimized without symmetry restrictions and vibrational frequency calculations were computed for all stationary points to confirm their nature as minima (zero imaginary frequencies) or as transition state (one imaginary frequency). Solvation effects were introduced implicitly through the PCM model, the reactions in solution are reproduced with acetone (ε=20.X) as solvent, and to reproduce the mechanochemical environment, the solvent has been customized to account for the mixture provided by the reagents and LAG. The values used for both dielectric constants and infinite dielectric constant are depicted in the subsection "Customization of the PCM model". The reported energies are free energies in solution or gas phase (specified throughout the text) at 298 K and 1 M. Microkinetic simulations were carried out using the COPASI 4.22 program; the values for the concentrations used in the model are

depicted in the subsection "Concentrations". A data set collection of all computed structures is available in the ioChem-BD repository.

Customization of the PCM model

The dielectric constant (ε) and refracting index (*n*) values for sulfonamide, carbodiimide and acetonitrile (LAG) used to define the PCM model are shown in Table 8.

Table 8. Dielectric constants and refracting indices used for the implementation of the solvation cage-like medium.

Compound	Dielectric constant (ε)	Refracting index (*n*)
Carbodiimide	3.4	1.482
Sulfonamide	3.5	1.380
Acetonitrile	37.5	1.344

With the values extracted from the literature, we can compute the ε and ε^{∞} for our reacting systems; the results are presented in Table 9. Notice that the same values have been employed for all the reactions. This is because the values for the dielectric constants and refracting index for the sulfonamides and carbodiimides with different substituents were difficult to find. Besides the use of the same LAG, which is present in higher amounts in comparison to the reagents, prompt us to assume that the final values for ε and ε^{∞} will be similar and therefore the effect on the reaction outcome will be negligible.

Table 9. Dielectric constants and refracting indexes applied as "solid average" in the reactions.

Solvent	Dielectric constant (ε)	Inf. dielectric constant (ε^{∞})
mix_SA	16.7	1.451

Concentrations

The values of the concentrations obtained for the N-sulfonylguanidine synthesis for: (1) the reaction in solution, obtained from the experimental data and (2) mechanochemical environment, obtained applying Equation 5, are presented in Table 10.

Table 10. Concentrations (M) obtained for the N-sulfonylguanidine synthesis in solution and in mechanochemical conditions for the four reactions under study.

Reaction	Solution concentration (M)	Mechanochemical concentration (M)
N1	0.7	2.91
N2	0.7	3.00
N3	0.7	2.90
N4	0.7	2.10

Results and discussion

Application of the method

Our strategy for the quantitative reproduction of ball milling transformations was applied to the N-sulfonylguanidine synthesis reported by Friščić and co-workers. Although the experimental work employs CuCl as catalyst in most of the transformations, we are interested in the catalyst-free reactions. The absence of catalyst implies a much simpler reaction mechanism, which is necessary for a successful validation of our approach.

The reactions selected for our investigation are shown in Scheme 9: three involving substituents that did not gave any conversion in the absence of catalyst (N2-N4), and only one (N1) that has been reported to show to reach the desired coupling product. Within the investigation of this reaction, we aim

to understand the enhanced reactivity when going from solution-based transformations to ball milling techniques.

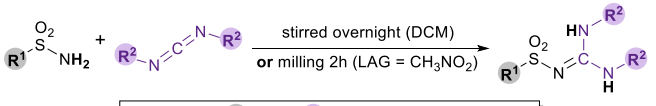

	R^1	R^2	
N1:	CF_3	*t*Bu	***Yield 92%***
N2:	*p*-tolyl	*i*Pr	
N3:	*p*-tolyl	*t*Bu	*No reaction*
N4:	CF_3	*p*-tolyl	

Scheme 9. Reactions under study by Friščić and co-workers for the N-sulfonylguanidines synthesis.

Since the Diels-Alder reaction was not highly affected by the dielectric environment, we were not able to discard one of the approaches, thus we will apply both vacuum and solid average once again. We envisage that in this case, due to the presence of a more complex mechanism, the medium can have a higher influence, and help on the discrimination between dielectric environments. First, we proceeded with the mechanistic investigation; Scheme 10 shows a general picture of the free energy profile that we computed for the four (N1-N4) reactions.

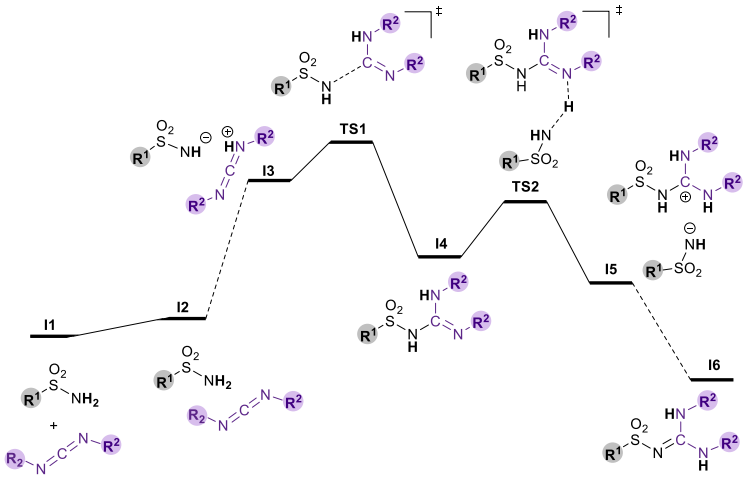

Scheme 10. Representation of the calculated mechanism for the synthesis of N-sulfonylguanidines.

The reaction starts with the formation of the adduct (**I2**) with the subsequent low barrier proton transfer from the sulfonamide to the carbodiimide. The proton transfer yields intermediate **I3**, which corresponds to an adduct between the two charged moieties interacting. Once intermediate **I3** is formed, it rapidly evolves towards the rate determining formation of the C-N bond through transition state **TS1**. This leads to intermediate **I4**, which evolves via a second proton transfer through the lower barrier **TS2**, which involves a sulfonamide shuttle. The need of a second sulfonamide molecule is required to avoid the formation of a high-strained three-membered transition state (Figure 8) which was found 18.1 kcal/mol higher for the specific case of the N1 reaction. This proton transfer proceeds in a stepwise manner, across intermediate **I5**, which evolves through a barrierless process to yield the desired product **I6** in an exergonic step.

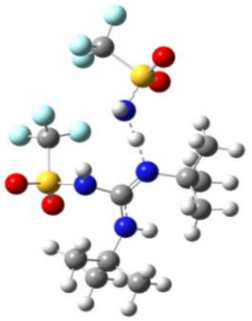

TS2 (11.1 kcal/mol)

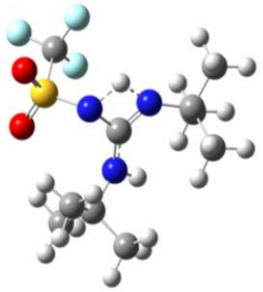

TS2$_X$ (29.2 kcal/mol)

Figure 8: Transition states for the second proton transfer for the N1 substituents in gas phase. A) intermolecular proton transfer and B) intramolecular proton transfer.

The energy data for systems N1-N4 is shown in **Table 11**. Note that different dielectric environments are presented; for reactions in solution we use dichloromethane, and for those in mechanochemical conditions, either vacuum or solid average. From the mechanistic profiles we can see that the RDS corresponds to **TS1** for all the systems. This step is followed by a downhill

transformation until the formation of the product. Therefore, we can envisage that the reaction could be approximated to a second order reaction, in which the kinetics of the process can be properly evaluated through the free energy difference between the separate reactants and **TS1**. We can clearly see that the inductive effects of the substituents play a crucial role in the height of the barrier. Adduct **I3** involves a charge separation, and some of this splitting is retained in **TS1**. Intermediate **I3** shows a considerably higher stabilization on the reaction N1 in comparison to the analogous intermediates in systems N2-N4 (Table 11). This stabilization rules the reaction outcome since the activation energy for the C-N coupling is only feasible for the reaction between **1a** and *tert*-butylcarbodiimide, **2a** (set N1), which corresponds in agreement with the experimental data. Although the barriers indicates that this is the only feasible reaction, which is in qualitative agreement with experiment, we wanted to go beyond this qualitative agreement, so we performed next an estimation of the reaction times *via* microkinetic modeling.

Table 11. Free energies values (in kcal/mol) for each of the stationary points of the mechanism depicted in Figure S1, for the four different set of substituents (from N1-N4).

		I1	I2	I3	TS1	I4	TS2	I5	I6
Dichloromehtane	N1	0.0	2.8	17.0	22.7	7.0	14.5	3.2	-8.4
	N2	0.0	4.6	28.8	29.2	-4.7	6.2	-0.6	-13.6
	N3	0.0	1.7	26.6	28.3	6.6	15.3	5.8	-3.5
	N4	0.0	6.6	25.1	26.1	-1.7	6.4	8.7	-12.6
Vacuum	N1	0.0	0.1	18.8	21.3	3.7	11.1	-	-16.8
	N2	0.0	2.7	25.2	31.1	-7.4	2.6	-	-11.0
	N3	0.0	2.1	28.4	30.4	3.4	9.9	-	-6.7
	N4	0.0	3.0	-	32.3	-5.3	4.1	-	-10.1
Solid Average	N1	0.0	3.4	16.6	22.6	7.6	17.9	3.7	-8.4
	N2	0.0	3.4	27.5	29.6	-4.6	7.7	-1.7	-14.2
	N3	0.0	2.8	26.0	29.2	7.8	16.2	6.4	-3.2
	N4	0.0	5.8	24.6	27.5	-1.4	6.5	7.3	-13.0

To perform the microkinetic analysis, first the free energy barriers of the three different environments (DCM, vacumm and solid average) were converted into rate constants. Then, for those systems reproducing a mechanochemical reaction, the concentrations were computed (as explained in the Concentrations section), and for the system in DCM, which was reproducing the reaction in solution, the value of the concentration was extracted from the experimental work. The results obtained with all these variations are reported in Table 12. We could even justify the minor disagreements. The experimental fact that the reaction is complete in two hours does not preclude that it could take place in less time. Regardless of this nuance, the agreement between our computed reaction times and the reported experimental values can be deemed as very good, showing an accurate prediction even for the most demanding system (N1).

We were delighted to find that only the reaction N1 is found to proceed within a feasible reaction time, in agreement with experiment. The difference between this system and the other three (N2-N4) is perfectly reproduced, with reaction times at the range of hundreds of thousands of hours for these non-reacting sets within all dielectric environments. Although the qualitative trend could be expected by the observation of the computed energy barriers, we view the quantitative agreement for reaction times as a serious confirmation of the validity of the treatment.

Table 12. Comparison between the time necessary for the quantitative conversion (99%) obtained by the application of a kinetic model to the different reaction sets (N1-N4) with the experimental reaction time.

	Dielectric environment	Concentration (M)	Predicted time (h)	Exp. time (h)
N1	DCM (8.9)	0.7[a]	11:47	12
	Vacuum (1)	2.9	0:15	2
	Solid Average (16.7)	2.9	1:08	2
N2	Dichloromethane	0.7	$6.66 \cdot 10^{3}$	No reaction
	Vacuum	3.0	$3.84 \cdot 10^{4}$	No reaction
	Solid Average	3.0	$3.05 \cdot 10^{3}$	No reaction
N3	DCM (8.9)	0.7[a]	$9.95 \cdot 10^{8}$	No reaction
	Vacuum (1)	2.9	$1.13 \cdot 10^{6}$	No reaction
	Solid Average (16.7)	2.9	$2.03 \cdot 10^{5}$	No reaction
N4	Dichloromethane	0.7	$3.56 \cdot 10^{1}$	No reaction
	Vacuum	2.1	$4.16 \cdot 10^{5}$	No reaction
	Solid Average	2.1	$1.26 \cdot 10^{2}$	No reaction

We could even justify the minor disagreements. The experimental fact that the reaction is complete in two hours does not preclude that it could take place in less time. Regardless of this nuance, the agreement between our computed

reaction times and the reported experimental values can be deemed as very good, showing an accurate prediction even for the most demanding system (N1).

Calculations indicate that the reaction in dichloromethane needs 11:47 hours to be completed, fully compatible with the experimental observation of the reaction running overnight. For the mechanochemical reaction, which takes 2 hours according to experiment, our calculations (solid average approach), predict a reaction time slightly above one hour (1:08). Incidentally, for this reaction we can discriminate between the two computational approaches for the dielectric environment, with the results being clearly in favor of using a dielectric constant related to those of the solids being mixed rather than to that of vacuum (0:15 hours). In addition, this result aids us to explain the influence of liquid-assisted grinding (LAG) in mechanochemical systems. On the solid average approach, we include the LAG used in the dielectric environment of the reaction. Although the effect of LAG is negligible in this system, it is not the case in others, particularly in those reactions with highly polarized transition states or ionic mechanisms where a modification of the dielectric environment may lead to drastic changes on the reaction outcome.

The fact that we can reproduce the experimentally observed acceleration of *ca*. one order of magnitude associated to mechanochemical conditions allows us to examine its origin. As mentioned above, according to our hypothesis, the mechanochemical conditions introduce changes in the dielectric constant and the concentrations. The reduction of time for this N-sulfonylguanidine synthesis is mainly driven by the increase on the concentration of the reacting species. The DFT-computed barriers, where dielectric effects are included, are almost the same for DCM and mechanochemical conditions. Thus, we show that in this case, the reaction acceleration is associated to the high effective reactant concentrations accessible in the ball milling device that cannot be reached in standard organic solvents.

6. Calculations on the synthesis of 2,4-dinitrophenylhidrazones

Experimental overview

The investigation of Diels-Alder and N-sulfonylguanidine synthesis has allowed us to validate our approach to the computational study of ball milling processes. It has also led us to select the solid average as the best description of the dielectric environment because it reproduces more accurately the reaction yields and provides an explanation of the effect of LAG. The validity of our hypothesis supports the similarities between mechanochemical and solution mechanisms. However, there are some systems for which complete different reactivities have been reported.

This is the case of the synthesis of 2,4-dinitrophenylhidrazones, also known as the Brady's test; a well-known qualitative analysis to determine the presence of aldehydes or ketones in a sample. The reaction requires the presence of acid catalysis when it is performed in solution, however, the product can be synthetized in absence of acid using mechanochemical techniques, as reported by Kaupp and co-workers.[42] The authors investigated a set of aldehydes and ketones which could react with 2,4-diphenylhidrazine. A selection of the reactivity is shown in Table 13. Most of the transformations proceeded within 10-20 min of kneading ball-milling at 60-70ºC (**1**a-h) or upon 15-20 min at 70-125ºC (**1**i-j). It must be noted that due to potential explosive nature of the dry 2,4-diphenylhidrazines, the reactant was introduced as wetted crystals (50% H_2O by weight).

This study represents a clear example of a reaction that proceeds through different mechanisms when performed in solution (acid catalysed) or under mechanochemical techniques (neutral medium). The clear differences between

42 Mokhatari, J.; Naimi-Jamal, M.R.; Hamzeali, H.; Dekamin, M.G.; Kaupp, G. *ChemSusChem*, 2009, **2**, 248-254.

both methodologies together with the simplicity of its reaction mechanism make this reaction suitable for our study.

Table 13. Synthesis of 2,4-dinitrophenylhydrazones from the reaction of 2,4-diphenylhidrazines with a diversity of aldehydes or ketones (1). The table show a small selection of the results reported in the experimental investigation.

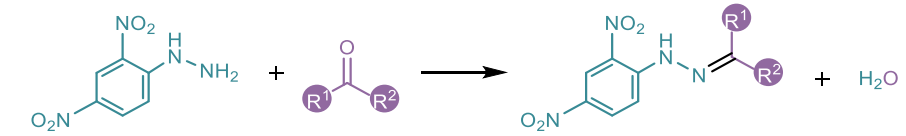

2,4-dinitrophenylhydrazine — 2,4-dinitrophenylhydrazone

1	R^1	R^2	1	R^1	R^2
a	H	Ph	f	H	MeCH-CH
b	H	*p*-HOC_6H_4	g	Me	Me
c	H	*p*-ClC_6H_4	h	Cyclohexanone	
d	H	$(Me)_2CH$	i	Me	Ph
e	H	*m*-$NO_2C_6H_4$	j	Benzophenone	

Computational details

All the calculations were carried out using Gaussian09 (Rev.D.01) with the B3LYP-D3 functional and the 6-31+G(d) basis set. Single-point calculations were performed with the 6-311++G(d,p) basis set to minimize the basis set superposition error (BSSE). Vibrational frequency calculations were computed to confirm the nature of all stationary points (zero imaginary frequencies for minima and one for transition states). Implicit solvent was included through the PCM method. In the case of the mechanochemical environment, the medium was defined as the mixture of reactants, the dielectric constant (ε) and infinite dielectric constant (ε^{∞}) were computed as explained in the section "Customization of the PCM model. For the reaction in solution ethanol (ε=24.85) was implemented as solvent. Explicit solvent molecules were

included as proton shuttles in the transition states. This has entailed the use of a cluster continuum model (see subsection *"Implementation of the cluster continuum model"*). The reported energies are free energies in solution at 298 K and 1 M unless otherwise stated. Microkinetic simulations were carried out using the COPASI 4.22 program; the values for the concentrations used in the model are depicted in the subsection "Concentrations". A data set collection of all computed structures is available in the ioChem-BD repository.

Customization of the PCM model

The values for the dielectric constants (ε) and the refracting index (*n*) used to define the PCM model are shown in Table 14**¡Error! La autoreferencia al marcador no es válida.**. Note that for benzaldehyde (BA) and benzophenone (BP) the same dielectric constant and refracting index were considered. This is, because the difference between the two compounds is minimal and, in this manner, we can apply the same solvent for all the calculations. We also mention that we did not find the dielectric constant of 2,4-dinitrophenylhidrazine, which was approximated to that of dinitrobenzene.

Table 14. Dielectric constants and refracting indices used for the implementation of the solvation cage-like medium.

Compound	Dielectric constant (ε)	Refracting index (*n*)
Water	78.76	1.340
2,4-dinitrophenylhidrazine	2.80	1.374
Benzaldehide / Benzophenone	18.22	1.546

These parameters were employed to calculate the solvent features following the strategy explained in the method section. The values obtained for the dielectric constant and the infinite dielectric constant are shown in Table 15.

Table 15. Dielectric constants and refracting indexes applied as "solid average" in the reactions.

Solvent	Dielectric constant (ε)	Inf. dielectric constant (ε^{∞})
Solid average	62.78	1.884

Concentrations

Table 16 shows the concentrations used to perform the microkinetic study: (i) reaction of benzaldehyde in solution (S-BA), obtained from the experimental data, (ii) reaction of benzaldehyde and benzophenone in a mechanochemical environment (M-BA and M-BP), obtained applying Equation 6, (iii) water contained in the 2,4-diphenylhidrazines crystals and (iv) ethanol employed as solvent.

Table 16. Initial concentrations (M) used for the Brady reaction in solution and in mechanochemical conditions.

System	Concentration (M)
S-BA	0.09
M-BA	3.34
M-BP	3.34
H2O	18.4
Ethanol	17.1

Results and discussion

Mechanism elucidation

With the experimental data in hand, we proceeded to apply the previously described methodology to compute ball milling reactions. Our goal is to reproduce the differences found with the synthesis of 2,4-dinitrophenylhidrazones in solution and in mechanochemical conditions, *i.e.*,

in solution acid catalysis is required, whereas through mechanochemistry the reaction proceeds in neutral conditions (Scheme 11). Benzaldehyde was selected as model system, and its reaction with 2,4-dinitrophenylhidrazine was investigated under both environments. To obtain a more general picture of the transformation, the reaction with benzophenone was also studied under mechanochemical conditions. This is because while the reaction with benzaldehyde proceeds in 10-20 min of kneading ball-milling at 60-70ºC, the reaction with benzophenone requires the use of acid as catalyst, even under mechanochemical conditions.

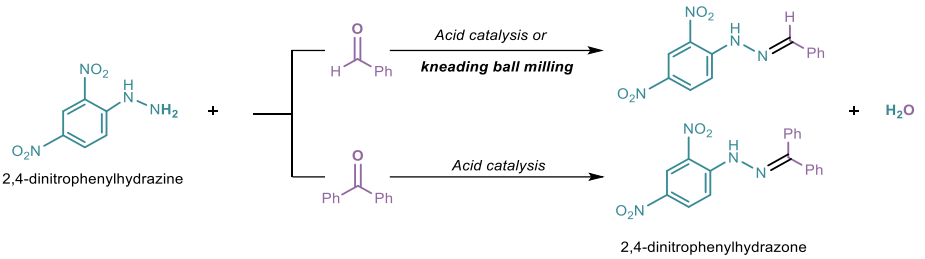

Scheme 11. Synthesis of 2,4-dinitrophenylhydrazone from 2,4-dinitrophenylhydrazine with benzaldehyde or benzophenone.

First, we elucidated the standard acid-catalyzed mechanism for the reaction in solution with benzaldehyde as the carbonyl group (Scheme 12). The reaction starts with the protonation of the aldehyde by the sulphuric acid leading to a charged carbonyl moiety with a considerable increased electrophilic character (**I2**). Although these acid-base process occurs through an endergonic step of 9.6 kcal/mol, the highly acidic medium favours the process. The protonated aldehyde reacts then with hydrazine through TS1, with an associated barrier for the C—N bond formation of 15.3 kcal/mol. This transition state is the rate determining step of the reaction. The process releases intermediate **I3** in a quasi-isoenergetic step of -0.3 kcal/mol. From this point the reaction involves a series of downhill acid-base steps: the acid deprotonates the charged nitrogen, forming the neutral species, **I4**, which is subsequently protonated releasing a

water molecule (**I5**). Finally, a molecule of H_2SO_4 abstracts a proton from intermediate (**I5**) leading to the formation of the 2,4-dinitrophenylhydrazone (**I6**).

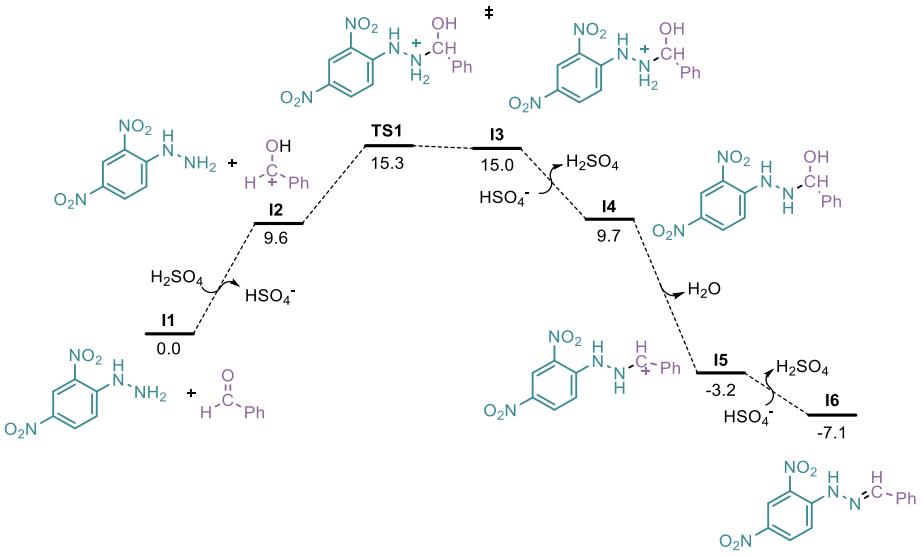

Scheme 12. Reaction mechanism for the acid catalysed synthesis of 2,4-dinitrophenylhydrazones in ethanol.

The low barriers obtained for the acid-catalyzed mechanism confirms the fast reaction rate involved on the synthesis of 2,4-dinitrophenylhydrazones when performed in ethanol solution; the reaction proceeds almost instantaneous at room temperature when acid catalysis is applied. Under neutral conditions the scenario changes, the coupling of 2,4-dinitrophenylhidrazines and carbonyl groups is not feasible, unless mechanochemical techniques are employed.

To understand this modified reactivity, we have calculated the reaction mechanism under neutral conditions in both solution and in mechanochemical medium. A general picture of the energetic profile is shown in Scheme 13. The reaction is composed by two main steps: first, the coupling of the carbonyl with the 2,4-dinitrohidrazine molecule (TS1) which yields the coupling product **I2**, second, a proton transfer from the nitrogen to the hydroxyl group which forms

the condensation product while releasing a water molecule (**I3**). Both steps are assisted by two solvent molecules (either ethanol or water), which are crucial to achieve less-strained transition states. The introduction of explicit solvent molecules while using implicit solvents is not trivial, in fact, this represents a major source of error on the simulation of the current system. The introduction of these molecules has been carefully studied and will be explained in the following subsection "Implementation of the cluster continuum model", since it can represent a major source of error.

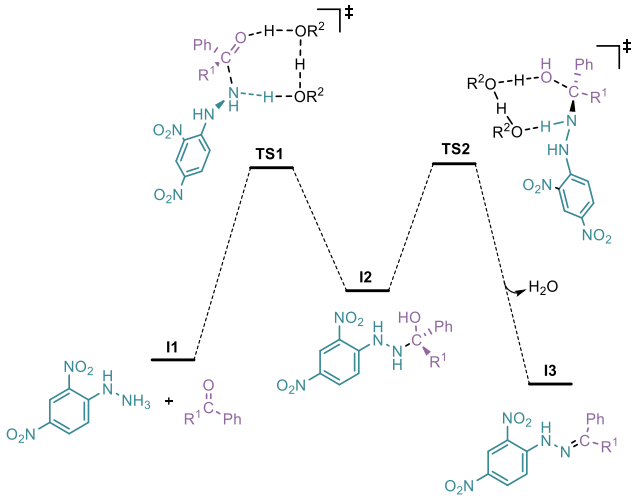

Scheme 13. Reaction mechanism under neutral conditions for benzaldehyde (R_1= H) or benzophenone (R_1= Ph) and using either ethanol (R_2=CH_2CH_3) or water (R_2=H) as proton shuttles.

The energy data obtained for all the systems is depicted in Table 17. For the sake of clarity, in the following discussion the systems will be labelled as S-BA, M-BA and M-BP, the first letter stands for solution or mechanochemistry and after the hyphen the substrate employed is defined (BA = benzaldehyde and BP = benzophenone). The effect of the solvent molecules as shuttle was investigated on the M-BA system. Since the use of two solvent molecules significantly decreases the activation energy, the same amount was used for the

S-BA and M-BP reactions. The barriers for both **TS1** and **TS2** are considerably high. For example, the mechanochemical reaction with benzaldehyde (M-BA), which should be affordable under mechanochemical conditions, presents barriers around 30 kcal/mol. However, within the analysis of the energy profile we are neglecting issues such as temperatures and concentrations. These parameters will be included on the microkinetic investigation, hence, the values herein presented should only be taken as a general trend.

Table 17. Energies obtained for the synthesis of 2,4-dinitrophenylhidrazones under neutral conditions with different carbonyl groups (benzaldehide and benzophenone) and in different mediums (solution or mechanochemical). Free energies at 298K and 1 atm.

Entry	System	Num. x Shuttle molecule	I1	TS1	I2	TS2	I3
1	S-BA	2 x ethanol	0.0	26.7	9.7	27.0	-3.5
2		2 x H_2O	0.0	29.3	9.7	30.7	-3.5
3	M-BA	2 x H_2O	0.0	29.7	10.0	29.9	-3.3
4		1 x H_2O	0.0	33.7	10.0	37.5	-3.3
5		-	0.0	46.7	10.0	58.1	-3.3
6	M-BP	2 x H_2O	0.0	37.0	12.3	34.3	-3.5

Implementation of the cluster continuum model

The neutral mechanism requires the incorporation of explicit solvent molecules as proton shuttles since they provide a less strained, and more stable transition states (Table 18). Unfortunately, the introduction of an isolated solvent molecule to the system is not trivial, this aspect is carefully discussed on the section “cluster continuum model” of the Theoretical background. Therefore, herein we will focus on the practical aspects of the application of a cluster continuum model to the current system, the most important aspect being the selection of the cluster size. Equation 11 presents the reaction used to correct

the introduction of explicit solvent molecules; $(Solv)_n$ represents the bulk of the solvent as a cluster of a given number of molecules, n, and x the number of molecules released from the cluster.

$$(Solv)_n \xrightarrow{\Delta G_1} x\,Solv + (Solv)_{n-x} \quad (3)$$

For the mechanochemical transformation (M-BA and M-BP) where the milling is performed with large amounts of water, the selection of the cluster is straightforward. Indeed, in the original article by Goddard and co-workers, they reported that a cluster of fourteen molecules of water is optimal for the application of the cluster continuum model. Thus, we have taken fourteen as a reference value, and extracted the structure of the cluster from their work, then one water molecule was introduced to the system to be able to compute ΔG_1 and obtain the value for the correction. The results for ΔG_1 are shown in Table 18. Note that different temperatures are specified, this is because the different systems proceed at different temperatures; therefore, each cluster has been corrected accounting for the desired temperatures (discussed below in the subsection; "Temperature").

On the other side, in the system with ethanol as solvent (S-BA), the scenario is more complex. The high conformational flexibility of ethanol hampers the characterization of the lowest energy cluster. Indeed, the potential energy surface (PES) of ethanol clusters is among the most complex alcohol clusters. To the best of our knowledge, the biggest ethanol cluster for which the PES has been extensively studied is a hexamer which is remarkably far from the size of water clusters that have been reported in the literature. Still, we assumed that the hexamer will be close to the asymptotic value that we need to reach to properly reproduce the process, hence, the error will be relatively small. This appears as the most viable option since the investigation of the PES of bigger ethanol clusters would be extremely time demanding, and the introduction of

ethanol molecules in a random manner would lead to considerably higher errors.

To obtain the correction value (Equation 3), we need to have another cluster with a difference of one solvent molecule. In this case, if we incorporate an extra solvent molecule to the cluster (as previously done with water), the error due would be considerably higher, due to the conformational flexibility of ethanol. Therefore, we decreased the number of molecules instead of augmenting it, and utilized an ethanol pentamer previously reported in the literature. The results for ΔG_1 are shown in Table 18. Once again, each system has been studied at the corresponding temperature, a fact that will be discussed in the following sections.

Table 18. Free energies for the reaction in Equation 6 of the different systems (S-BA, M-BA and M-BP) with the corresponding solvent and temperature.

Entry	System	Solvent	Temperature (K)	Energy (kcal/mol)
1	S-BA	Ethanol	298	-3.6
2	M-BA	H_2O	343	-5.3
3	M-BA	H_2O	373	-6.6
4	M-BP	H_2O	368	-6.6
5	M-BP	H_2O	398	-7.5

Microkinetic analysis

Once the mechanistic profile has been elucidated it is necessary to proceed with the microkinetic study. To avoid unrealistic trimolecular steps (moreover not allowed by the COPASI software), two different reactions involving the formation of the adducts between the substrates and the solvent molecule were defined.

The rate constants depend on the temperature, thus the values in the free energy profiles reported above must be corrected for each experimental temperature: 298K for S-BA, 343 K for M-BA and 368K for M-BP. Once we have the complete energy profile, we can proceed with the calculation of the rate constants (Table 19). Note that the adduct formation (R1, R2, and R3) have been included as diffusion-driven processes. In contrast, R4 and R5 proceed through **TS1** and **TS2**, respectively.

Table 19. Rate constants (k_1 and k_{-1}) for all the reactions included in the kinetic model (R1-R5) on the different systems (S-BA, M-BA, M-BP) at the experimental temperature.

	S-BA (298 K)		M-BA (343 K)		M-BP (368 K)	
	k_1	k_{-1}	k_1	k_{-1}	k_1	k_{-1}
R1	$5.3625 \cdot 10^{8}$	$3.3341 \cdot 10^{9}$	$2.6385 \cdot 10^{8}$	$8.2281 \cdot 10^{10}$	$7.9332 \cdot 10^{8}$	$8.5342 \cdot 10^{10}$
R2	$7.5268 \cdot 10^{7}$	$2.3754 \cdot 10^{10}$	$1.1125 \cdot 10^{11}$	$1.9514 \cdot 10^{8}$	$1.5165 \cdot 10^{11}$	$4.4645 \cdot 10^{8}$
R3	$2.2757 \cdot 10^{12}$	$7.8567 \cdot 10^{5}$	$1.6072 \cdot 10^{10}$	$1.3508 \cdot 10^{9}$	$4.5774 \cdot 10^{11}$	$1.4791 \cdot 10^{8}$
R4	$5.8628 \cdot 10^{-5}$	$6.6947 \cdot 10^{-1}$	$2.2846 \cdot 10^{-4}$	$1.8040 \cdot 10^{1}$	$2.4800 \cdot 10^{-10}$	3.2531
R5	$4.1805 \cdot 10^{-1}$	$9.0027 \cdot 10^{-10}$	$5.0184 \cdot 10^{1}$	$4.7036 \cdot 10^{-6}$	$3.6776 \cdot 10^{2}$	$1.5377 \cdot 10^{-6}$

Finally, the rate constants were combined with the concentrations (sub-section "Concentrations" on the Computational details) and included in the microkinetic study. The yields obtained with the corresponding reaction time (10 minutes for S-BA and M-BA systems and 1h for M-BP) at each experimental temperature are shown in Table 20.

When benzaldehyde is used as carbonyl group, the theoretical yields obtained are 2% and 13% for S-BA and M-BA, respectively. The increase on yield of M-BA compared to S-BA confirms that the reaction is faster under mechanochemical conditions. Still, the yield obtained for M-BA is much lower than expected, as experimentally the reaction achieves full conversion after 10 minutes. The results are still qualitatively correct, as the theoretical yield for

the M-BP reaction is 0%, in agreement with the experimental data, but something seems to be amiss.

Table 20. Theoretical yields obtained after a reaction time of 10 minutes for the S-BA, M-BA and 1h for the M-BP system at the experimental temperatures.

System	Temperature (K)	Yield (%)
S-BA	298	2
M-BA	343	13
M-BP	368	0

We decided to further investigate what could be wrong with our modelling of this system, and we postulate that there is an issue with the temperature inside the milling jar. It has been proposed that the local temperatures inside the jar an increase because of the input of kinetic energy due to the collisions of the milling balls, or because of the exothermicity of the reaction taking place. In fact, temperature increases from 6 to 30K depending on the system under study. This depends on the frequency, the ball mill used and the specific reaction being carried out, therefore it depends on the experimental conditions. We will examine in what follows how this local jar effect can affect our computational predictions with two different methods.

The first of them is taken the publications by Emmerling and co-workers, who proposed that local temperature effects led to an effective decrease of 1.5 kcal/mol in the reaction barrier. We will thus use this decrease to recompute our barriers. We will also use as alternative treatment a direct increase of temperature of 30K, which we expect to have a similar effect. The rate constants associated to this increased temperature are reported in Table 21).

Table 21. Rate constants (k_1 and k_{-1}) for all the reactions included in the kinetic model (R1-R5) on the mechanochemical systems (S-BA, M-BA, M-BP) at the experimental temperature + 30 K.

	M-BA (373 K)		M-BP (398 K)	
	k_1	k_{-1}	k_1	k_{-1}
R1	$2.1055 \cdot 10^{8}$	$3.9682 \cdot 10^{11}$	$4.4711 \cdot 10^{10}$	$4.9650 \cdot 10^{9}$
R2	$3.3931 \cdot 10^{11}$	$2.4623 \cdot 10^{8}$	$2.6086 \cdot 10^{11}$	$8.5097 \cdot 10^{8}$
R3	$5.3161 \cdot 10^{10}$	$1.5716 \cdot 10^{9}$	$8.4906 \cdot 10^{11}$	$2.6145 \cdot 10^{8}$
R4	$2.6129 \cdot 10^{-3}$	$1.2454 \cdot 10^{2}$	$5.7071 \cdot 10^{-9}$	$2.1164 \cdot 10^{1}$
R5	$4.8475 \cdot 10^{2}$	$1.0705 \cdot 10^{-4}$	$1.4816 \cdot 10^{2}$	$1.8122 \cdot 10^{-6}$

The effect of introduction of this local jar effect with the two methods is reported in Table 21, entries 3 and 4. The local jar effect increases substantialy agreement with experiment: the predicted yield for M-BA increases from 13% to 78% when the 30K increase is applied (Table 22, entry 3) and to 70% with the drecrease of the barrier (Table 22, entry 4). In contrast, for the M-BP reaction, the theoretical yield remains 0% after one hour of reaction with both methodologies (Table 22, entries 6 and 7), also in agreement with experiment.

Table 22. Comparison of the predicted yields obtained after a reaction time of 10 minutes for the S-BA, M-BA and 1h for the M-BP with a variety of approaches.

Entry	System	Temperature (K)	Yield (%)
1	S-BA	298	2
2	M-BA	343	13
3	M-BA [b]	373	78
4	M-BA [c]	343	70
5	M-BP [a]	368	0
6	M-BP [a,b]	398	0
7	M-BP [c]	368	0

[a] Experimental reaction time of one hour. [b] Local jar effect through method 1 (temperature increase). [c] Local jar effect through method 2 (free energy decrease).

This local jar effect leads thus to a highly improved agreement. However, we are aware that this is a tentative explanation, as such effect was not included in the two previous reactions, which showed also good agreement. The only thing we can say is that temperature changes inside the jar are not always monitored, and that they may behave differently. Indeed, Andersen and co-workers demonstrated that for the specific case of their Diels-Alder reactions (section Diels-Alder), the temperature in the milling jar suffered an increase of merely 2 ºC. However, this potential usually overlooked on synthetic mechanochemistry. In fact, the parameter is not discussed neither in the work by Friščić and co-workers on the synthesis of N-sulfonylguanidines (section N-sulfonylguanidine synthesis), nor in the current work on the synthesis of 2,4-dinitrohidrazones. It may well be that the explosive nature of 2,4-dinitrohidrazines, and the associated exothermicity leads in this case to a termperature increase that is absent from the other two cases.

Summary

We have developed a method for the modelling of mechanochemical reactions through the combination of standard DFT tools, and microkinetic modeling. The strategy is based on the incorporation of a dielectric environment, specific concentrations, and an eventual local jar correction. Even though this are not the only features that may play a mechanistic role on mechanochemical reactions, they proved to be enough for the reproduction of experimental reaction times and yields for three different organic reactions.

This investigation emerges as a proof-of-concept of the similitudes between ball milling and solution-based reactions. The mechanistic similarity, and our ability to reproduce mechanochemical reactions, opens a promising path for the design and optimization of other mechanochemical processes.

Chapter II. "Ni-catalyzed Reductive Cross-coupling enabled by a Substrate Radical Trapping Mechanism"

UNIVERSITAT ROVIRA I VIRGILI
BEYOND CONVENTIONAL DFT CATALYSIS: MECHANOCHEMISTRY AND SOLID REDUCTANTS
Bruna Sánchez Pladevall

1. Introduction

Transition metal catalysed cross-coupling reactions are among the most used transformations in organic synthetic chemistry for their versatility in building molecular complexity.[1] The reaction takes place between a nucleophilic and an electrophilic coupling partners, leading to the selective formation of C–C or C–X bonds.[2] Traditionally, cross-coupling reactions involved the palladium-catalysed coupling of a sp^2-hybridized aryl halide with an organometallic reagent (organoboron, organotin, organozinc, organosilicon or Grignard reagents).[3] However, the methodology has evolved in the past decades reaching a high level of sophistication and broadening the scope, achieving effective couplings with a wide range of substrates (Scheme 1).[4]

The standard organometallic nucleophiles have been expanded to other compounds such as organolithium or organoiridium derivatives which proved to be adequate for some transformations.[5] Besides, over the last years, alternative strategies such as C-H activation or the use of stabilized carbon

1 Biffis, A.; Centomo, P.; del Zotto, A.; Zecca, M. *Chem. Rev.* **2018**, 118, 4, 2249-2295.

2 (a) Ruiz-Castillo, P.; Buchwald, S.L. *Chem. Rev*. **2016**, 116, 12564–12649. (b) Brijesh, S.K**.** ***Catal. Sci. Technol.***, **2021**,**11**, 1186-1221.

3 (a) Nicolaou, K.C.; Bulger, P.G.; Sarlah, D. *Angew. Chem. Int. Ed.* **2005**, 44, 4442–4489. (b) Corbet, J-P.; Mignani, G. *Chem. Rev*. **2006**, 106, 2651–2710. (c) Magano, J.; Dunetz, J.R. *Chem. Rev.* **2011**, 111, 2177–2250. (d) Buchwald, S.L. *Acc. Chem. Res.* **2008**, 41, 1439. (e) Gildner, P.G.; Colacot, T.J. *Organometallics*, **2015**, 34, 5497–5508. (f) Hazari, N.; Melvin, P.R.; Mohadjer, B.M. *Nat. Rev. Chem.* **2017**, 1, 0025.

4 Sestelo, J.P.; Sarandeses, L.A. *Molecules*, **2020**, 25, 4500.

5 (a) Hornillos, V.; Massimo, G.; Vila, C.; Fañanás-Mastral, M.; Feringa, B.L. *Org. Lett.* **2013**, 15, 19, 5114–5117. (b) Jia, Z.; Liu, Q.: Peng, X.S.; Wong, H.N.C. *Nat Commun.*, **2016**, **7,** 10614. (c) Zhao, K.; Shen, L.; Shen, Z.-L.; Loh, T.-P. *Chem. Soc. Rev.* **2017**, 46, 586–602. (d) Gil-Negrete, J.M.; Sestelo, J.P.; Sarandeses, L.A. *Chem. Commun*. **2018**, 54, 1453–1456.

nucleophiles, *e.g.*, enolates, have gained importance.[6] Such methodologies avoid the need of pre-activation, and allow proceeding from commercially available species, leading to a faster and cleaner process. On the other hand, the set of electrophilic coupling partners has also been successfully extended to other less reactive sp^2-hybridized electrophiles (amides, esters, amines, etc),[7] as well as sp^3-hybridized electrophiles. [8]

The fast development of cross-coupling reactions is due largely to the detailed understanding of the underlying mechanisms, comprising the study of side reactions and the elucidation of the nature of reaction intermediates.[9] In general, the transformation proceeds through three main steps: (i) oxidative addition, (ii) transmetalation and (iii) reductive elimination (Scheme 1).[10]

Even though palladium is the original and most used metal in cross-coupling reactions, first row metals are gaining ground since they can promote transformations that are challenging with the second-row metal. In particular, nickel catalysts, which are commonly proposed as surrogate for palladium, have proved to be highly effective to promote transformations involving the activation of inert substrates as well as the reduction of the β-hydride elimination rate, achieving products that are inaccessible with palladium e.g.,

6 Topics in Current Chemistry, Vol. 292; Yu, J.-Q.; Shi, Z. (Eds.) Springer: Berlin, Germany, 2010.

7 (a) Dander, J.E.; Garg, N.K. *ACS Catal.* **2017**, 7, 1413–1423. (b) Takise, R.; Muto, K.; Yamaguchi, J. *Chem. Soc. Rev.*, **2017**, 46, 5864–5888. (c) Guo, L.; Rueping, M. *Chem. Eur. J.*, **2018**, 24, 7794– 7809.

8 Choi, J.; Fu, G.C. *Science*, **2017**, 356, eaaf7230.

9 (a) Schwarzer, M.C. et al. *J. Am. Chem. Soc*. **2017**, 139, 10347–10358. (b) Somerville, R.J.; Hale, L.V.A.; Gómez-Bemgoa, E.; Burés, J.; Martin, R. *J. Am. Chem. Soc*., **2018**, 140, 8771–8780. (c) Reina, A.; Krachko, T.; Onida, K.; Bouyssi, D.; Jeanneau, E. Monteiro, N.; Amgoune, A. *ACS Catal.* **2020**, 10, 3, 2189–2197.

10 Campeau, L.-C.; Hazari, N, *Organometallics*, **2019**, 38(1), 3-35.

reactions involving C(sp^3) couplings.[11] The ease that nickel presents in front of palladium to promote these transformations is based on the substantial differences that exist between them. The most notorious one is its higher activity and oxidation state flexibility which givess access to a wide diversity of reactivity patterns *e.g.* radical pathways.[12] These properties allow nickel-catalysed cross-coupling reactions to proceed through diverse mechanisms involving both one and two electron pathways.

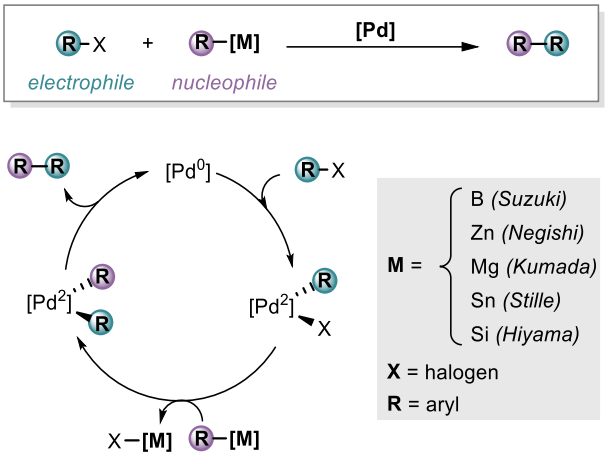

Scheme 1. Conventional Pd-catalysed cross-coupling reaction; reaction mechanism standard and nucleophiles employed.

Nickel catalysts can promote the classical C(sp^2) couplings through the standard two-electron cross-coupling mechanism (analogous to Pd-catalysed pathway). Commonly, the concerted mechanism involves a the Ni^0/Ni^{II} catalytic cycle,[13] however, the higher reducing properties of Ni in comparison

11 Jana, R.; Pathak, T. P.; Sigman, M. S. *Chem. Rev*. **2011**, 111, 1417–1492.

12 De Aguirre, A.; Funes-Ardoiz, I.; Maseras, F. *Angew. Chem. Int. Ed*. **2019**, 58(12), 3898-3902.

13 Jin, L.; Zhang, H.; Li, P.; Sowa, J.R.; Jr; Lei, A. *J. Am. Chem. Soc*. **2009**, 131, 29, 9892–9893.

to Pd, opens the possibility of a Ni^{I}/Ni^{III} variant[14] (Scheme 2, A). Notice that in these concerted mechanisms, the high oxidation state flexibility of nickel species can hinder the reactivity, promoting off cycle reactions.[15]

On the other hand, most Ni-catalysed cross-coupling transformations involving $C(sp^3)$ electrophiles imply the presence of SET events and radical pathways. These mechanisms are typically classified as radical rebound pathway[16] (Scheme 2, B) or radical chain pathway (Scheme 2, C). Both catalytic cycles start with a Ni^{I} halide intermediate followed by a sequence of steps which depends on the nature of the system. In the radical rebound cycle, the Ni^{I} species undergoes first the transmetalation, then the electrophile approaches and performs a SET oxidative addition, namely halide abstraction, in which a Ni^{II} species and a radical are formed. Subsequently, those species are combined yielding the Ni^{III} intermediate which is prone to perform the reductive elimination. In the radical chain cycle, the Ni^{I} complex reacts with the electrophile through a SET oxidative addition initiating a chain reaction, in which the formed radical is trapped by the nickel centre after the transmetalation step.

14 Zhang, K. Conda-Sheridan, M.; Cooke, Louie, J. *Organometallics* **2011**, 30(9), 2546–2552.

15 Diccianni, J. B.; Diao, T. *Trends in Chemistry*, **2019**, 1(9), 830–844.

16 Lin, X.; Phillips, D.L. *J. Org. Chem.* **2008**, 73, 10, 3680–3688.

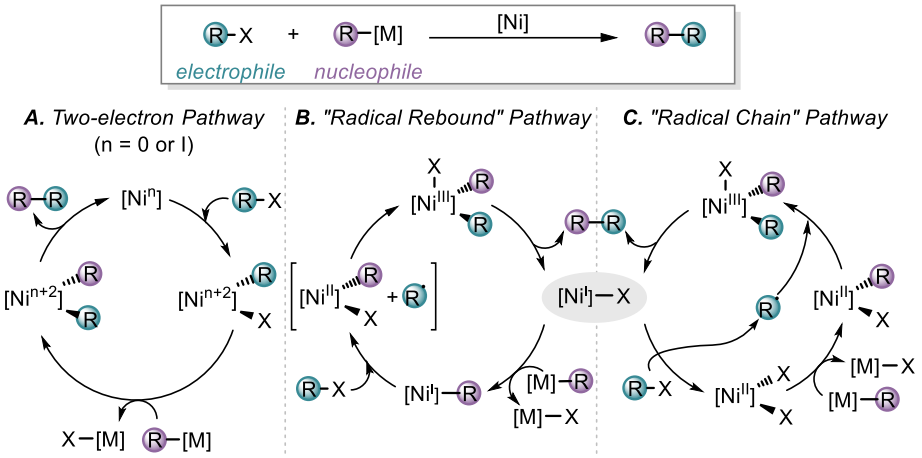

Scheme 2. Ni-catalysed cross-coupling reaction mechanisms. (A) two-electron pathway, (B) radical rebound pathway, (C) radical chain pathway.

The increased mechanistic understanding on cross-coupling reactions has directly inspired the study of other types of reactivity, such as reductive couplings. Although this coupling strategy has been known for over a century,[17] most significant advances were achieved over the past decade.[18] The concept of reductive coupling is simple; it involves the reaction of two electrophilic centres with the incorporation of an external reductant to maintain the entire procedure electroneutral (Scheme 3). This synthetic strategy is interesting from a green chemistry perspective since it avoids the use of organometallic reagents (which usually need to be previously synthesized), substituting it by more commercially available compounds such as alkyl halides. In addition, it prevents functional group incompatibilities, arising from the inherent reactivity of some of the common organometallic reagents. A conceptually related

17 Wurtz, A.; *Ann. Chem. Pharm.* **1855**, 96, 364–375.

18 (a) Knappke CEI; Grupe S; Gaertner D; Corpet M; Gosmini C; Jacobi von Wangelin A. *Chem. Eur. J.* **2014**, 20, 6828–6842. (c) Weix, D.J. *Acc. Chem. Res.* **2015**, 48, 1767–1775. (c) Gu, J.; Wang, X.; Xue, W.; Gong, H. *Org. Chem. Front.* **2015**, 2, 1411–1421. (d) Richmond, E.; Moran, J. *Synthesis*, **2018**, 50, 499-513.

solution is the use of oxidative coupling, which in turn requires an external reducing agent. This has been also studied in our group but is not the subject here.

In contrast to cross-coupling reactions, reductive cross-coupling mechanisms are far less understood, the main challenge being the cross-selectivity origin. Whereas in classic cross-coupling reactions, the substrates are well differentiated, this is not the case in the reductive cross-coupling scenario where the use of two electrophiles as coupling partners implies similar substrate reactivities, making it difficult to achieve a selective cross-coupling bond formation, as opposed to homo-coupled products.[19]

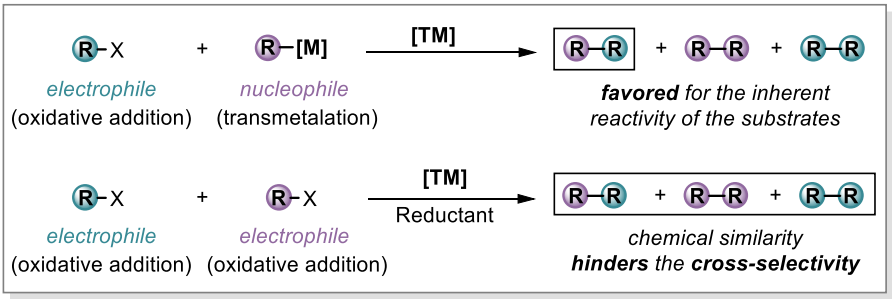

Scheme 3. Comparison of selectivity challenges between classic cross coupling transformations with cross-electrophile couplings.

The current state of understanding with regard to cross-electrophile coupling mechanisms is still far from providing a general and unified picture of these transformations. The reaction shares several steps with traditional cross-coupling, however, substantial differences exist between them; the most remarkable being the absence of the transmetalation step. In cross-electrophile couplings the organometallic nucleophile is replaced by a second electrophile, which is also activated through an oxidative addition event. Therefore, the general mechanism involves two subsequent oxidative additions followed by a

19 Everson, D.A.; Weix, D.J. *Journal of Organic Chemistry*, **2014**, 79(11), 4793–4798.

reductive elimination. The cross-selectivity of these two oxidative addition steps is the critical point for the discrimination between heterocoupling and homocoupling products.

Within these standards, different reaction pathways have been proposed with major differences found on the oxidative addition events: sequential reduction mechanism (Scheme 4, A) and radical chain mechanism (Scheme, B).[20] In the sequential reduction mechanism, first, one electrophile selectively undergoes a concerted oxidative addition at the Ni^0 center. Then, the metal is reduced yielding a Ni^I intermediate that activates selectively the second electrophile through another oxidative addition event. Finally, a reductive elimination occurs, followed by a second reduction of the catalyst to recover the Ni^0 active species. In this reaction manifold, the substrates must present a sufficient degree of electronic differentiation to favor the cross-coupling over the homocoupling *i.e.*, each compound must preferentially undergo oxidative addition with either a Ni^0 or a Ni^I species.

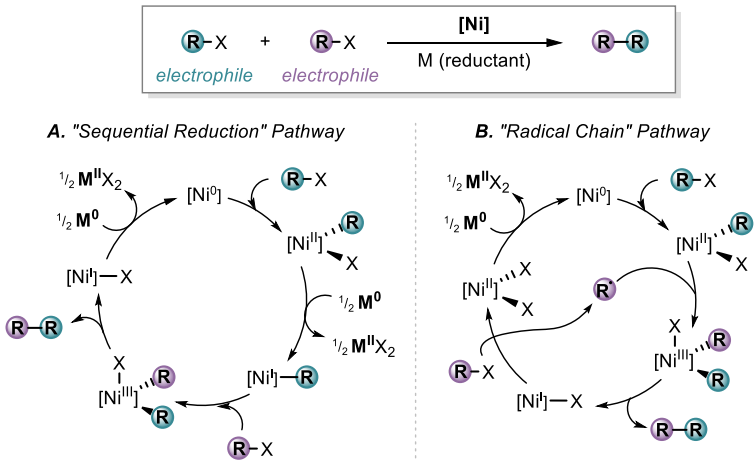

Scheme 4. Ni-catalysed cross-coupling reaction mechanisms. (A) sequential reduction pathway and (B) radical chain pathway.

20 Lucas, E.L.; Jarvo, E.R. *Nat. Rev. Chem.* **2017**, 1, 0065.

In the radical chain mechanism, the reaction also starts with the selective oxidative addition of one of the electrophiles in the Ni^0 centre. The other electrophile reacts *via* radical formation leading to a chain reaction in which the formed radical is trapped by the Ni^{II} species obtained after the first oxidative addition event. From the resulting Ni^{III} specie the reductive elimination can take place yielding the cross-coupling product and a Ni^{I} halide. Notice that this Ni^{I} intermediate is the one that prompts the radical formation with the second electrophile yielding a Ni^{II} specie that is reduced to recover the Ni^0 active specie. This pathway selectively forms the cross-coupling product when one of the substrates preferentially undergoes a two-electron oxidative addition and the other is more prone to radical formation. Typically, this involves a $C(sp^2)$-$C(sp^3)$ coupling: the sp^2-hybridized electrophile couple through a concerted oxidative addition with the Ni^0 centre and sp^3-hybridized electrophiles are activated via SET oxidative addition on a Ni^{I}.

There is still a long path towards the full understanding of cross-electrophile coupling mechanisms. Although there are a wide range of synthetic cross-electrophile couplings methods,[21] the mechanistic investigations of these systems are hampered by the presence of the reductant which presents complications on the mechanistic analysis; as it leads to the formation of heterogeneous reaction mixtures and paramagnetic species (which hamper the ^1H NMR reaction monitoring).

The problem is further complicated by the relative scarcity of computational investigations in the field.[22] Similarly to what happens in experimental studies, this is due to the substantial difficulties that the methodology presents. For

21 (a) Everson, D.A.; Shrestha, R.; Weix, D.J. *J. Am. Chem. Soc.* **2010**, 132, 920-921. (b) Wu, F.; Lu, W.; Qian, Q.; Ren, Q.; Gong, H. *Org. Lett*. **2012**, 14, 3044-3047. (c) Sun, S.; Börjesson, M.; Martin-Montero, R.; Martin, R. *J. Am. Chem. Soc*. **2018**, 140, 12765-12769.

22 Y. Wang, Q. Ren, *Curr. Org. Chem.* **2020**, 24, 1367-1383.

example, intrinsic problems owing to the presence of a solid reducing agent as well as the difficulties to control and predict the reactivity of the commonly employed catalysts (such as Ni), due to their high oxidation state flexibility. Even it is not trivial to obtain, we expect mechanistic understanding to be crucial for the exploitation of the synergistic role of reductant and metal, and to the further optimization of new catalytic systems based on these features.

2. Experimental overview

Over the past decades, there has been a steady increase on the number of fluorine-containing drug candidates in the pharmaceutical industry.[23] The selective introduction of fluorine to target molecules can modulate a wide range of properties, *e.g.*, activity, metabolic stability, or bioavailability. Therefore, the exploration of this biologically relevant chemical space and the development of simple and efficient fluorination methods has been of great interest in both academic and industrial worlds.[24]

In 2018, Sheng *et al.* applied, for the first time, a reductive cross-coupling methodology to perform late-stage monofluoroalkylation of drugs (Scheme 5).[25] In the original work, the authors claim that the methods developed until the moment, including direct fluorination of C-H bonds of alkyl arenes and transition metal catalysed cross-coupling of monofluoroalkyl halides with aryl metal species, involve harsh reaction conditions and functional group incompatibility, impeding its application to late-stage processes. By contrast, the mild conditions conferred by reductive cross-coupling strategies (due to the absence of an organometallic nucleophile) can promote fluoroalkylation in the synthesis of a wide range of drug-like molecules.

23 Pattison, G. *Organic and Biomolecular Chemistry*, **2019**, 17(23), 5651–5660.

24 Caron, S. *Organic Process Research and Development*, **2020**, 24(4), 470–480.

25 Sheng, J.; Ni, H.-Q.; Zhang, H.-R.; Zhang, K.-F.; Wang, Y.-N.; & Wang, X.-S. *Angew. Chem. Int. Ed.*, **2018**, 57, 7634 –7639.

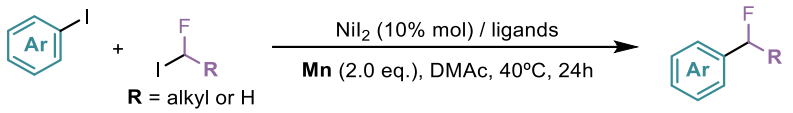

Scheme 5. Ni-catalysed reductive cross-coupling of aryl halides with monofluoroalkyl halides reported by Sheng *et al.*

The optimization of the reaction conditions was achieved through combinatorial catalysis, where a mixture of monodentate and bidentate ligands was found to be required to effectively promote the transformation. We consider this system to be a good example of cross-electrophile couplings, with an explained preference for heterocoupling *vs* homocoupling. Moreover, the authors published several mechanistic experiments that can be extremely helpful for the in depth analysis of the transformation. In this section we want to introduce the reader to the most important details of the experimental work.

The authors started the optimization of the reaction conditions taking phenyl iodide (**1a**) and 1-fluoro-1-iodoethylbenzene (**2a**) as parent substrates. The coupling was performed in the presence of 10 mol% of NiI_2, superstoichometric amounts of Mn (2 eq.) and with dimethylacetamide (DMAc) as solvent. When 4,4'-dimethyl-2,2'-dipyridyl (dmbpy) was used as ligand, the desired heterocoupling product was obtained in 21% yield after 24h at 40ºC (Table 1, entry 1). With this encouraging result in hand, they started the screening of different phosphines and nitrogen-based ligands.

The use of bidentate ligands gave, in all cases, yields close to 20% (entries 1-4). On the other hand, when monodentate ligands were screened the coupling product was not observed (entries 5-8). Then, the authors started a combinatorial study with dmbpy (the bidentate ligand achieving the highest yield) and various N- or P-based monodentate ligands. When the P-based ligand (PPh_3) was employed, no rise in the conversion yield was observed (entry 9). However, with N-based ligands, the conversion increased from 20%

up to 80% with the 4-cyanopyridine (4-CNPy) ligand (entries 10-12). Thus, the mixture of dmbpy (10 mol%) and 4-CNPy ligands (20 mol%) was selected as the optimal combination for the present system. Besides, the yield obtained with this combination could be slightly improved (from 80 to 88%) when the amount of **2a** was increased to 1.1 equivalents (entry 13). Thus, the latter parameters were selected as the optimal reaction conditions.

It is noteworthy that the authors also provide a complete investigation of the nickel source, solvents and temperatures, as well as a larger optimization of the ligand selection including a combinatorial screening and the study of the amount of catalyst required. However, these results are not relevant for the discussion of the computational investigation and will not be presented here. Finally, control experiments were conducted to ensure the participation of both nickel catalyst and ligands (entries 14 and 15).

With the optimal conditions in hand, they investigated the scope of the reaction (Scheme 6). First, variations on the aryl halides including *para*-, *meta*- and *ortho*- substitutions were tested, obtaining good to excellent yields for both electron donating groups (**7**, **8**, **12**, **13**, **17**, **18**) and electron withdrawing groups (**4**-**6**, **9**-**11**, **14**-**16**). Besides, polycyclic substrates were also found to be compatible with the reaction, leading to the formation of the desired product in excellent yields (**19**, **20**). Various monofluoroalkyl iodides including different alkyl chain lengths and substituents in the aromatic ring were tested without modifying the high reaction efficiency.

Table 1. Optimization of reaction conditions in the experimental work by Sheng *et al.* [a]

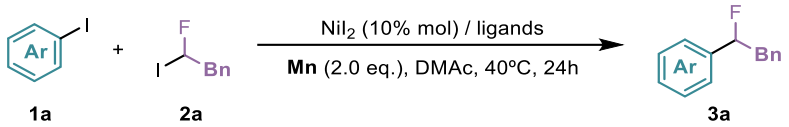

1a **2a** **3a**

entry	Ligands (mol %)	**3a** Yield (%)
1	dmbpy (10)	21
2	bpy (10)	17
3	dtbpy (10)	17
4	dombpy (10)	16
5	pyridine (20)	0
6	4-CNPy (20)	0
7	DMAP (10)	0
8	PPh_3	0
9	dmbpy (10) / PPh_3 (20)	20
10	dmbpy (10) / Py (20)	71 (71)
11	dmbpy (10) / DMAP (20)	40
12	dmbpy (10) / 4-CNPy (20)	80 (82)
13[b]	dmbpy (10) / 4-CNPy (20)	88 (91)
14	-	0
15[c]	dmbpy (10) / 4-CNPy (20)	0

[a] The yield was determined by ^{19}F NMR spectroscopy using $PhCF_3$ as an internal standard; yields in parentheses are for the isolated product. [b] The reaction was carried out with **2a** (1.1 equiv). [c] No NiI_2 was added.

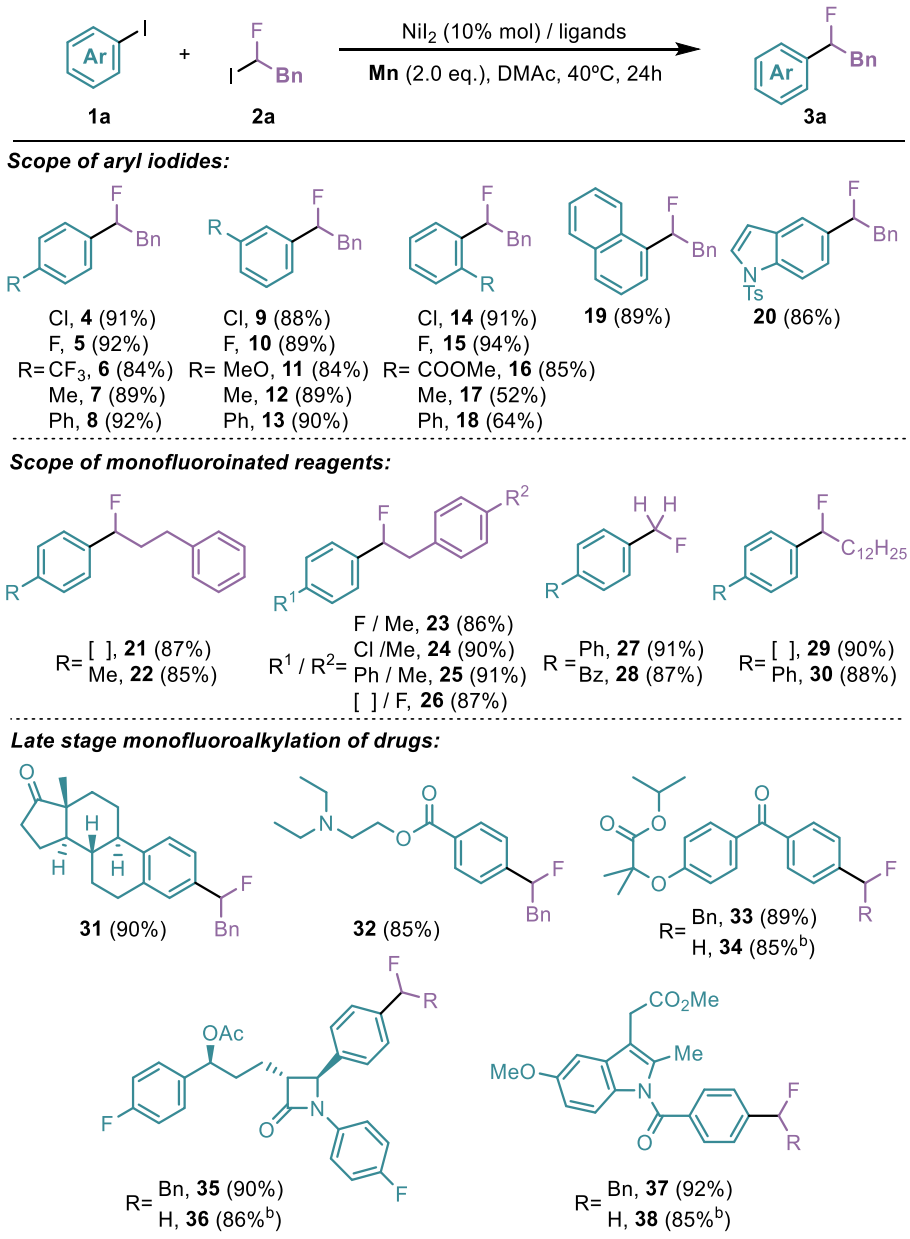

Scheme 6. Selected examples of the substrate scope of the Ni-catalysed reductive cross-coupling of aryl halides with monofluoroalkyl halides reported by Sheng *et al.*

The reaction scope demonstrates the excellent functional-group tolerance of the catalytic system which is crucial to perform late stage monofluoroalkylation of drugs. In fact, the authors succeeded in applying their methodology to complex biologically active molecules (bearing a wide range of functional groups), obtaining compounds such as ezetimibe, estrone, indometacin, fenofibrate and procaine in excellent yields (**31**-**38**).

After evaluating the substrate scope and demonstrated the excellent functional-group tolerance of the methodology, the authors performed some further mechanistic experiments to gain insights into the reaction pathway. First, the authors introduced a radical clock reagent to the standard reaction conditions (Scheme 7) and observed the formation of the ring-opened product in a 21% yield (**39**), pointing out to the presence of a free monofluoroalkyl radical in the catalytic cycle.

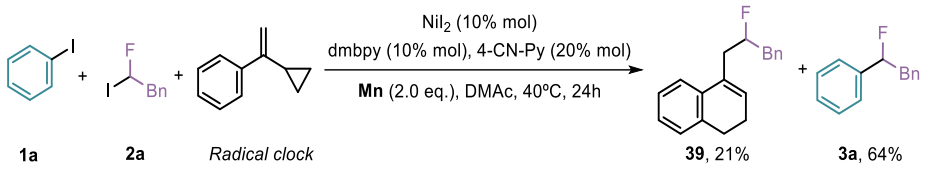

Scheme 7. Mechanistic experiment; introduction of a radical clock to the standard reaction conditions.

Then, they investigated the oxidation state of the metal in the active species by replacing the nickel(II) salt precursor by $Ni(cod)_2$. The reaction successfully achieved the product **3a** in a 93% yield, indicating the presence of a Ni^0 active species; since the reaction could proceed from a Ni^0 precursor, the presence of a Ni^{II} or Ni^{I} active was not necessary. In the original reaction conditions, this Ni^0 active species can arise from the reduction of the nickel salt by Mn, prior to the start of the catalytic cycle.

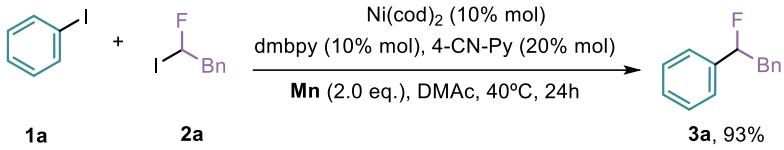

1a **2a** **3a**, 93%

Scheme 8. Mechanistic experiment; substitution of the standard nickel source (NiI_2) by the Ni^0 species, $Ni(cod)_2$.

The potential role as catalyst of a Ni^0 active species together with the formation of a monofluoroalkyl radical prompted the authors to synthetise the potential reaction intermediate **40** (Scheme 9). When the reaction between **40** and **2a** was performed under stoichiometric conditions (Scheme 9, top), the desired product was obtained in a 76% yield, likewise when the nickel species **40** was employed as nickel source (instead of the $NiBr_2$) in the standard catalytic conditions (Scheme, bottom) the coupling product was obtained with a 81% yield. These results are comparable to those obtained in standard conditions, indicating the plausible participation of **40** into the catalytic cycle. Then variations on the amount of Mn and 4-CNPy were tested, demonstrating the key role of both species. On one hand, elimination of Mn led to a drop of the reaction yield from 76% to 34% in stoichiometric conditions and only traces were obtained when the catalytic system was investigated. On the other hand, the exclusion of the 4-CNPy leads in both cases (stoichiometric and catalytic conditions) to only traces of the desired product.

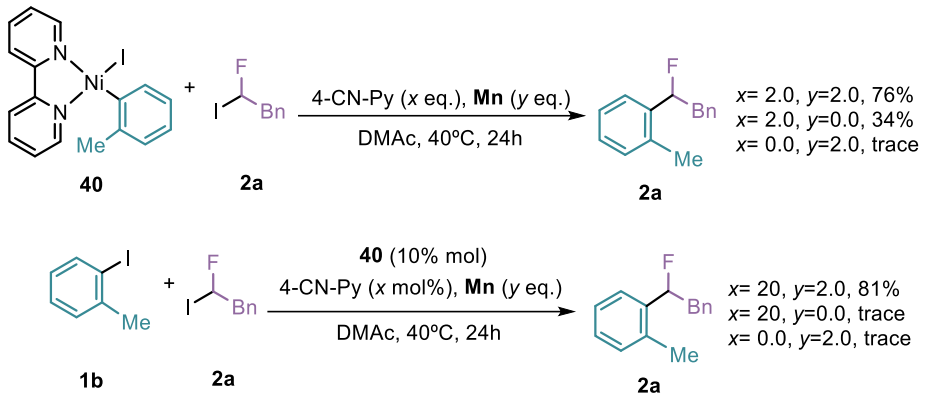

Scheme 9. Mechanistic studies for the identification of plausible intermediates of the catalytic cycle (40).

Finally, the authors performed control experiments to rule out the possible in-situ formation of monofluoroalkyl manganese species (**Scheme**). The monofluoroalkyl halide, **2a** was subjected to standard conditions (in absence of its coupling partner, **1a**) and no monofluoroalkyl manganese species were detected, thus the authors discarded the formation of such compound in the reaction media.

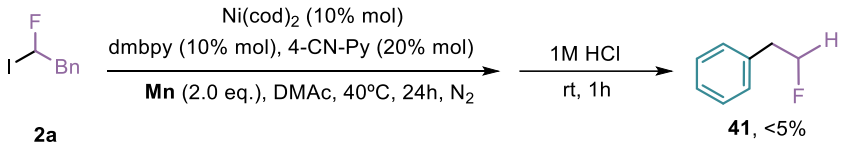

Scheme 10. Control experiment to rule out the formation of monofluoroalkyl manganese species.

With all the mechanistic information in hand, the authors concluded that the results obtained are consistent with the classic nickel-based reductive cross-coupling catalytic cycles. Therefore, they proposed two plausible mechanistic scenarios (Scheme 11) based on previously reported catalytic cycles for reductive cross-coupling.

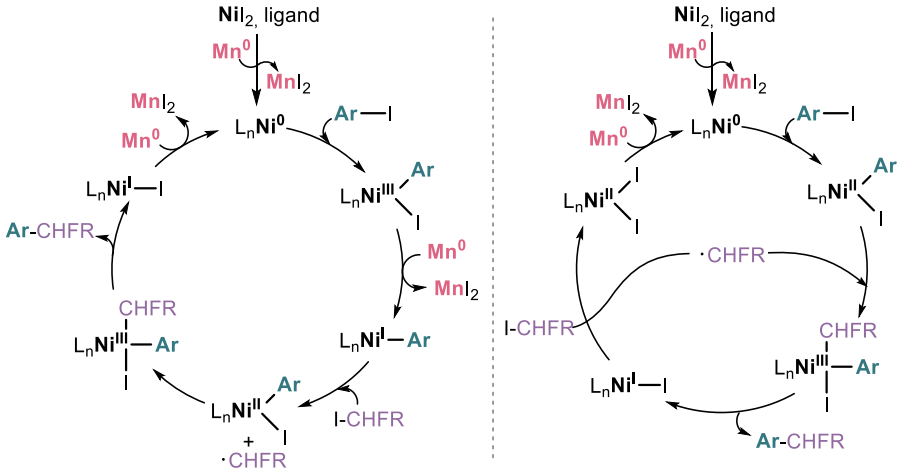

Scheme 11. Plausible catalytic cycles proposed by Sheng *et al.*

3. Objectives

The work by Sheng *et al.* reported above represents a brilliant example of the challenges on the mechanistic investigation of reductive coupling reactions. The poorly differentiated substrates, the high flexibility of nickel species, which is even more notorious upon the use of manganese as reductant, and the presence of radicals, which are known to easily promote off cycle reactions, hampers the identification of the main catalytic cycle. Indeed, the authors proposed two plausible catalytic cycles in accordance with the mechanistic information that they were able to gather. We believe that in this case, and even more fundamentally as a general rule, it is crucial to combine experiments with computational studies, if possible, in a jointly effort to improve the understanding of reaction mechanisms and drive the development of new strategies.

It is not always possible to work hand-in-hand with experimentalists, fortunately, microkinetic modelling appears as the missing link between the two worlds, enabling a more accurate simulation of complex transformations.

To our knowledge, microkinetic modelling has never yet been applied for the rationalisation of reductive coupling mechanisms. Herein we aim to combine the experimental information on the Ni-catalysed reductive cross-coupling of aryl halides with monofluoroalkyl halides with the diverse computational techniques available to achieve a comprehensive picture of the transformation. Special attention is directed towards the reproduction of the challenging selectivity, as well as the role of side reactions originating from the highly flexible character of the system.

4. Computational details

All calculations were carried out using the Gaussian09 (Rev. D.01)[26] package at the B3LYP[27] level of theory, including Grimme empirical dispersion.[28] For geometry optimizations, the standard 6-31G(d)[29] basis set was employed for all

26 M. J. Frisch, G. W. Trucks, H. B. Schlegel, G. E. Scuseria, M. A. Robb, J. R. Cheeseman, G. Scalmani, V. Barone, B. Mennucci, G. A. Petersson, H. Nakatsuji, M. Caricato, X. Li, H. P. Hratchian, A. F. Izmaylov, J. Bloino, G. Zheng, J. L. Sonnenberg, M. Hada, M. Ehara, K. Toyota, R. Fukuda, J. Hasegawa, M. Ishida, T. Nakajima, Y. Honda, O. Kitao, H. Nakai, T. Vreven, J. A. Montgomery, J. E. Peralta, F. Ogliaro, M. Bearpark, J. J. Heyd, E. Brothers, K. N. Kudin, V. N. Staroverov, R. Kobayashi, J. Normand, K. Raghavachari, A. Rendell, J. C. Burant, S. S. Iyengar, J. Tomasi, M. Cossi, N. Rega, J. M. Millam, M. Klene, J. E. Knox, J. B. Cross, V. Bakken, C. Adamo, J. Jaramillo, R. Gomperts, R. E. Stratmann, O. Yazyev, A. J. Austin, R. Cammi, C. Pomelli, J. W. Ochterski, R. L. Martin, K. Morokuma, V. G. Zakrzewski, G. A. Voth, P. Salvador, J. J. Dannenberg, S. Dapprich, A. D. Daniels, Farkas, J. B. Foresman, J. V. Ortiz, J. Cioslowski and D. J. Fox, Revision D.01 ed., Gaussian, Inc., Wallingford, CT, **2009**.

27 (a) A. D. Becke, *J. Chem. Phys*, **1993**, *98*, 5648-5652; (b) C. Lee, W. Yang and R. G. Parr, *Phys. Rev. B*, **1988**, *37*, 785-789; (c) P. J. Stephens, F. J. Devlin, C. F. Chabalowski and M. J. Frisch, *J. Phys. Chem.*, **1994**, *98*, 11623-11627

28 S. Grimme, J. Antony, S. Ehrlich and H. Krieg, *J. Chem. Phys.*, **2010**, *132*, 154104.

29 (a) M. M. Francl, W. J. Pietro, W. J. Hehre, J. S. Binkley, M. S. Gordon, D. J. DeFrees and J. A. Pople, *J. Chem. Phys.*, **1982**, *77*, 3654-3665; (b) P. C. Hariharan and J. A. Pople, *Theor. Chim. Acta*, **1973**, *28*, 213-222; (c) W. J. Hehre, R. Ditchfield and J. A. Pople, *J. Chem. Phys.*, **1972**, *56*, 2257-2261.

C, H, N, and F atoms and the LANL2DZ[30] basis set, along with its associated ECP was employed for Ni and I. For all calculations, vibrational frequency calculations were computed to establish the nature of all stationary points (zero imaginary frequencies for minima and one for transition states). Potential energies were further refined with 6-311+G(d,p)[31] for all atoms, except for I, in which LANL2DZ(d,p)[5] and its associated ECP was used and for Ni, in which LANL2TZ[32] and its associated ECP was applied. Solvation was implemented implicitly through the SMD methodology and n,n-dimethylacetamide selected as solvent (ε= 37.781).[33] All the calculations have been carried out at 298.15K and 1 atm.

Microkinetic modelling was performed on the DFT free energy profiles with the COPASI 4.22[34] software. The parameters used for the study were based on the experimental conditions: all the initial concentrations were set to zero except for **Mn**=0.8M, **1a**=0.2M, **2a=**0.2M and **4-CNPy**=0.04M. The evolution of the concentrations was investigated within 24h, which is the experimental reaction time. The study accounted for the experimental temperature (313 K). Computed free energies were modified by applying corrections for the temperature (from 298.15 K to 313.15 K) and a change on the reference state (from 1 atm to 1 M). These modifications have been done through the GoodVibes 1.0.1[35] program.

30 P. J. Hay and W. R. Wadt, *J. Chem. Phys.*, **1985**, *82*, 270-283.

31 R. Krishnan, J. S. Binkley, R. Seeger and J. A. Pople, *J. Chem. Phys.*, **1980**, *72*, 650-654.

32 L. E. Roy, P. J. Hay and R. L. Martin, *J. Chem. Theory Comput.*, **2008**, *4*, 1029-1031.

33 A. V. Marenich, C. J. Cramer and D. G. Truhlar, *J. Phys. Chem. B*, **2009**, *113*, 6378-6396.

34 Hoops, S.; Sahle, S.; Gauges, R.: Lee, C.; Pahle, J.; Simus, N.; Singhal, M.; Xu, L.; Mendes, P.; Kummer, U. *Bioinformatics*, **2006,** 22, 3067.

35 Funes-Ardoiz, I.; Paton, R.S. GoodVibes: GoodVibes v1.0.1. Zenodo.

A data set collection of all computational data is available in the ioChem-BD repository.[36]

5. Results and discussion

We selected phenyl iodide (**1a**) and 1-fluoro-1-iodoethylbenzene (**2a**) as coupling partners for the computational investigation i.e., the same substrates used by the authors as parent substrates in the optimization of reaction conditions (Scheme 12).

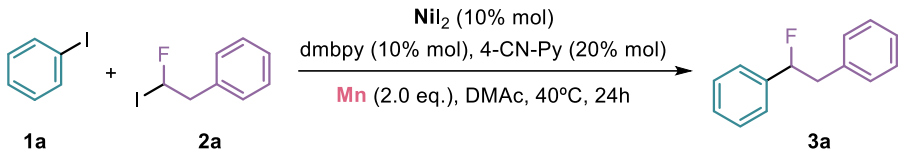

Scheme 12. Model reaction used in the computational study of the reductive cross-coupling of aryl halides with monofluoroalkyl halides reported by Sheng *et al.*

Reduction of the NiI_2 precursor

The transformation starts with the reduction of the nickel salt (NiI_2) by solid manganese (Scheme 13**Scheme**). The participation of solid manganese in the redox reaction leads to the application of a thermodynamic cycle for the calculation of the free energy change. This method, as explained in the theoretical background section permits the calculation of the standard reduction potential (SRP) of a solid metal in a given solvent. The division of the SRP by the number of electrons leads to the free energy of the solid manganese oxidation. We can then add the value to the DFT estimation of the change associated to the reduction of the nickel complex and obtain the thermodynamic parameters of the overall redox process.

36 M. Alvarez-Moreno, C. de Graaf, N. Lopez, F. Maseras, J. M. Poblet, C. Bo, *J. Chem. Inf. Model.* **2015**, *55*, 95–103.

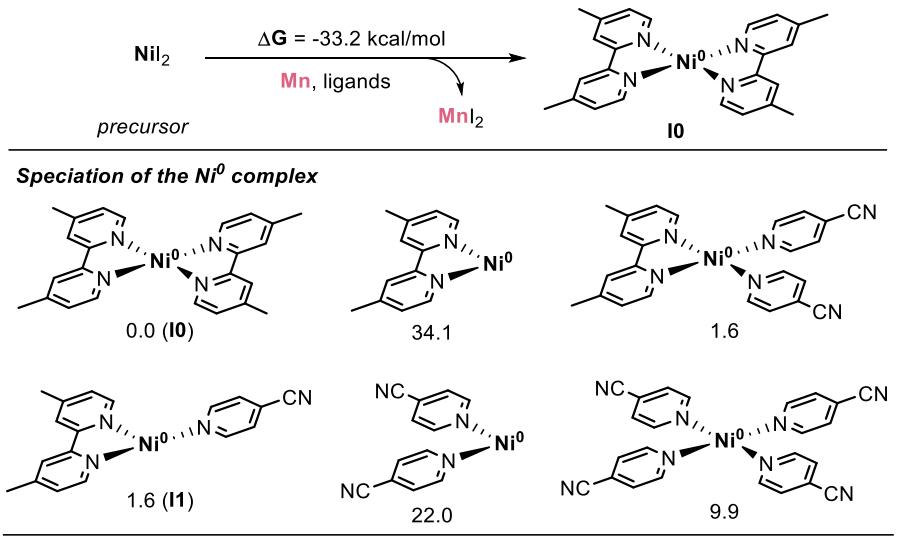

Scheme 13. Reduction of the NiI_2 salt by manganese to form the precursor of the catalytic cycle (top) and speciation of the possible species formed after the nickel salt reduction. Gibbs free energies in kcal/mol.

The reaction proceeds in an exergonic manner, with a free energy of -33.2 kcal/mol and yields a Mn^{II} salt and a Ni^0 complex, **I0**, where the metal center is coordinated to two dmbpy ligands (Scheme 13, top). The preferred ligand coordination sphere on the Ni^0 complex was elucidated through a speciation study, in which different combinations of dmbpy and 4-CNPy ligands were investigated (Scheme 13, bottom).

It can be mentioned that the thermodynamic cycle would first release a cationic manganese and two iodide atoms to the reaction media which would then react to form the ionic pair through an exergonic reaction of 5.1 kcal/mol. The procedure outlined above to compute the energy cost of the abstraction of electrons from solid manganese has been directly included in the calculation of all the redox thermodynamic steps throughout the chapter.

Mechanistic profile

Conventional cross-electrophile mechanism

Although the Ni(dmbpy)$_2$ (**I0**) is the most stable Ni^0 complex, the high affinity of the low valent nickel species for a square planar coordination blocks the oxidative addition from taking place on this complex. Thus, the first step of the reaction involves a slightly endergonic ligand exchange of 1.6 kcal/mol between a dmbpy and a 4-CNPy ligands to form the active species, **I1**. Moreover, the 4-CNPy ligand presents a redox non-innocent behavior and, in some cases, can delocalize one electron, formally oxidizing the nickel center by one unit (Scheme 14). As we will further discuss in the following section, the redox non-innocent behavior of 4-CNPy ligand and the more flexible coordination sphere conferred by the combination of bidentate (dmbpy) and monocoordinate (4-CNPy) ligands, are crucial to achieve the transformation in excellent yields.

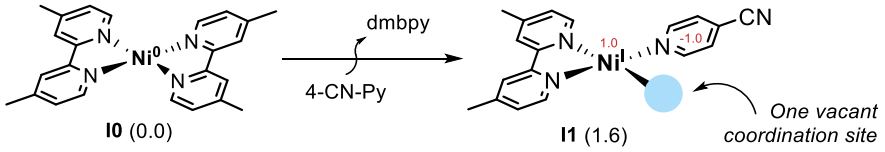

Scheme 14. Ligand exchange to achieve the active specie of the catalytic cycle, **I1**. Gibbs free energies in kcal/mol.

Once we have achieved the active species, the transformation proceeds through an oxidative addition of either phenyl iodide (**1a**) or 1-fluoro-1-iodoethylbenzene (**2a**). This process can occur through different pathways: (i) concerted two electron oxidative addition and (ii) halide abstraction, which involves a single electron transfer (SET) process. Our experience with similar substrates had found a preference for halide abstraction processes. [37] Bearing

37 (a) de Aguirre. A.; Funes-Ardoiz, I.; Maseras, F. *Angew. Chem. Int. Ed.* **2019**, 131, 3938-3942. (b) Nelson, D. J.; Maseras, F. *Chem. Commun.* **2018**, 54, 10646-10649. (c) Funes-Ardoiz, I.; Nelson, D. J.; Maseras, F. *Chem. Eur. J.* **2017**, 23, 16728-16733.

this in mind, and considering that the concerted pathways are often favored for reagents involving sp^2 carbons (due to orbital disposition),[38] we selected phenyl iodide (**1a**) as model substrate to investigate the preferred pathways *i.e.*, concerted oxidative addition or halide abstraction. For the sake of completion, we also considered two possible ligand coordination spheres for the concerted oxidative addition (Scheme 15).

From the active specie **I1**, the oxidative addition proceeds through the concerted pathway with a barrier of 45.5 kcal/mol ($\mathbf{TS_{OXadd2}}$). This barrier is lowered to 23.8 kcal/mol with the decoordination of a 4-CNPy ligand prior to the transition state, which allows the process to occur through a square planar conformation: the preferred disposition of low valent nickel species ($\mathbf{TS_{OXadd1}}$). On the other hand, the halide abstraction transition state ($\mathbf{TS_{habs1}}$) is found at 11.4 kcal/mol, thus becoming the preferred pathway for the oxidative addition process. Since **1a** (due to the sp^2 nature of the carbon), is more favourable to the concerted two electron oxidative addition in comparison to **2a**, we will assume that **2a** will also proceed through a halide abstraction mechanism. Moreover, the presence of a SET mechanism is consistent with the experimental observations, where the use of a radical clock shuts down the reaction, pointing out the presence of a free radical on the reaction media.

38 Mollar, C.; Besora, M.; Maseras, F.; Asensio, G.; Medio-Simon, M. *Chem. Eur. J.* **2010**, *16*, 13390-13397.

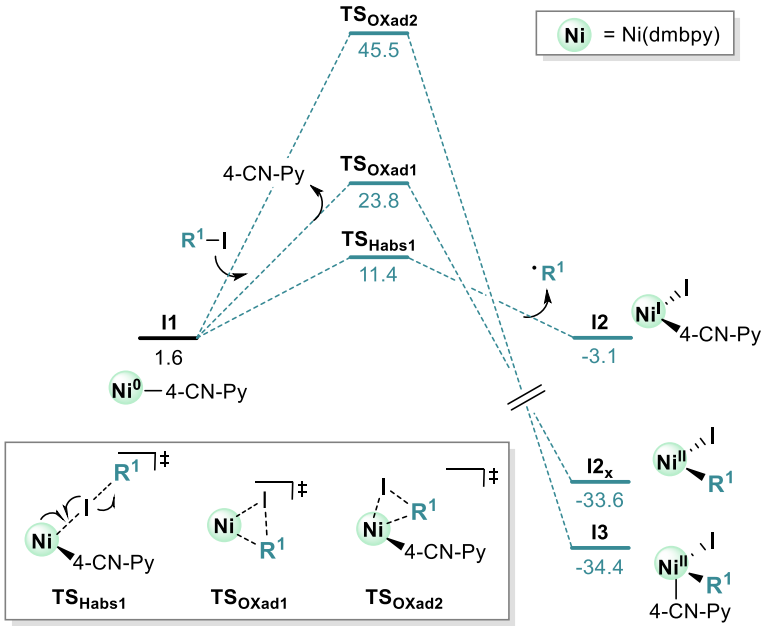

Scheme 15. Comparison of possible pathways for the oxidative addition: concerted two electron oxidative addition and halide abstraction mechanism. Gibbs free energies in kcal/mol.

Having elucidated the preferred oxidative addition pathway, we studied the competition between the oxidative addition of the two substrates: **1a** and **2a**. The first part of the mechanism for both substrates is shown in Scheme 16. After the ligand exchange with the subsequent formation of the active species, **I1**, the transformation evolves towards the halide abstraction, found at 11.4 and 7.1 kcal/mol, for **1a** and **2a**, respectively. The process releases a radical yielding the intermediate **I2**, which presents a wide energy difference (11.5 kcal/mol) between both pathways in favour of substrate **2a**. The trends observed are related to the radical stability; with radicals in sp^3 centres being more stable than those in sp^2. When the *p*-character of the orbital containing the free radical decreases, *i.e.* the *s*-character increases, the half-filled orbital containing the free radical is held closer to the nucleus leading to a higher electron affinity that implies a highly destabilized radical. The energy difference between

pathways found in **I2** (arising from the radical stability) disappears when the radical is trapped by the Ni centre to form **I3**. This process occurs in a highly exergonic step of 31.3 kcal/mol for **1a** and 20.9 kcal/mol for **2a**. Finally, manganese reduces the Ni^{II} species **I3** to the Ni^{I} species **I4** in a slightly exergonic step of 4.3 and 3.4 kcal/mol for **1a** and **2a**, respectively.

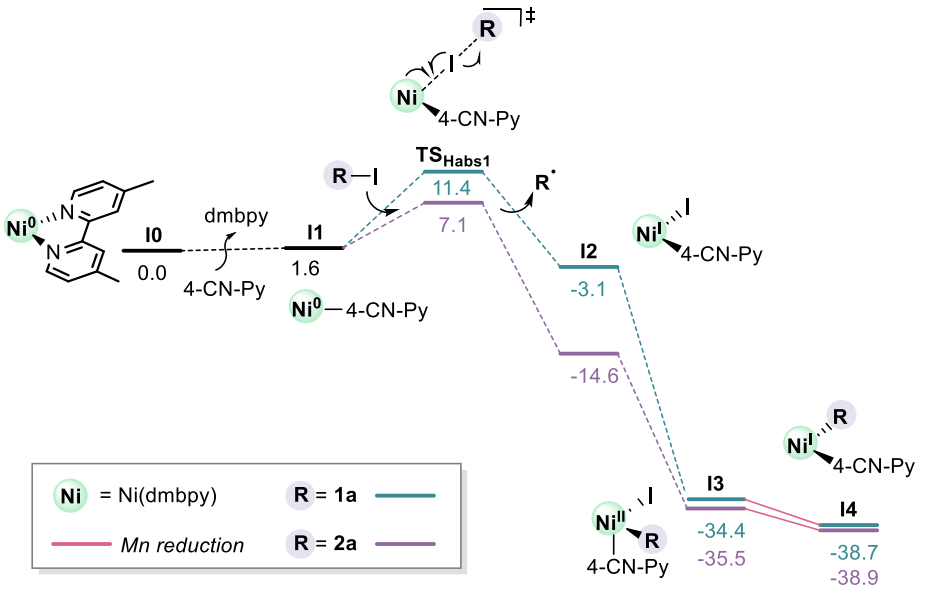

Scheme 16. Reaction mechanism for the first oxidative addition of both the aryl halide (1a) and monofluoroalkyl halide (2a). Gibbs free energies in kcal/mol.

From intermediate **I4** the reaction proceeds with a second oxidative addition leading to four possible scenarios corresponding to the homo and heterocoupling products. For the sake of clarity, we have divided the paths on different schemes depending on the outcome of the first oxidative addition: Scheme 17 present the mechanism after the oxidative addition of **1a** and Scheme 18 the pathway after the oxidative addition of **2a**. It is noteworthy that there are no significant qualitative differences between paths, only the relative energies of intermediates and transition states. Thus, we will only discuss in detail the mechanism after the oxidative addition of **1a** shown in Scheme 17.

To differentiate between the intermediates of the homocoupling and heterocoupling pathways we have used the same labels for the intermediates and an additional subscript has been used to specify the system in specific cases, such as in the microkinetic modeling. When only one substrate has performed the oxidative addition, we use the subscripts **1a** or **2a** referring to the substrate. For the second oxidative addition, *i.e.*, when two substrates have been activated, we use the superscript hom1a (**1a** homogeneous path), hom2a (**2a** homogeneous path) and het (heterogeneous coupling).

The second stage of the pathway starts with the decoordination of the 4-CNPy ligand from the nickel center in intermediate $\mathbf{I4_{1a}}$ to yield the tricoordinated species $\mathbf{I5_{1a}}$. This intermediate reacts with a second equivalent of substrate trough $\mathbf{TS_{habs2}}$, found at 14.2 and 10.8 kcal/mol for **1a** and **2a**, respectively. Once more, the process follows a halide abstraction pathway which favors the oxidative addition of **2a**. The process releases the corresponding radical together with intermediate **I6**. The two forms of intermediate **I6** present a quite high energy difference (11.4 kcal/mol) between pathways due to differences in sp^2 and sp^3 radical stabilities (favoring the latter). Then, the radical is trapped by the nickel center yielding **I7** which is 1.6 kcal/mol more stable for the **1a** homocoupling pathway. Intermediate **I7** can decoordinate the iodine atom yielding **I8**; this reaction implies an easily affordable process of 7.7 kcal/mol for the **1a** homocoupling pathway, however, the heterocoupling pathway presents a considerably high energy step of 17.6 kcal/mol. Once **I8** is obtained, it can easily evolve towards the coordination of one 4-CNPy ligand yielding **I9** in an exergonic step of 12.5 and 20.9 for **1a** and **2a**, respectively. All this Ni^{III} species can perform the reductive elimination through an affordable barrier (Scheme 17, table).

The reductive elimination shows a clear dependence on the degree of orbital hybridization favouring those cases where a greater *p*-character is found on the carbons involved on the process, thus, the lowest activation energy is found for

the **1a** homocoupling ($\Delta G^{\ddagger}$ = 3.6 kcal/mol). The relative barriers for the formation of both homo and hetero-coupling products are similar on the three possible pathways (from **I7**, **I8** or **I9**). However, we must bear in mind the high instability of **I8** which will hamper the reductive elimination from this intermediate.

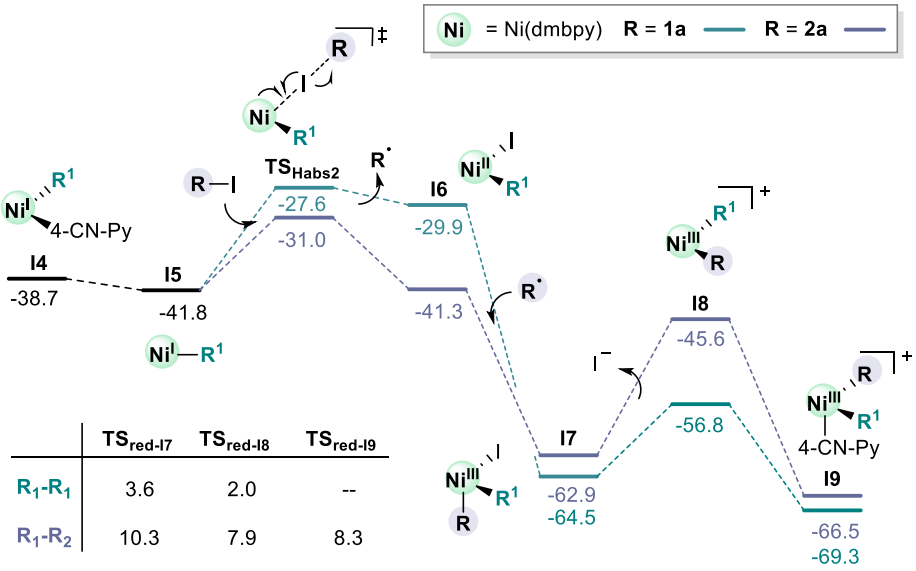

	$TS_{red\text{-}I7}$	$TS_{red\text{-}I8}$	$TS_{red\text{-}I9}$
R_1-R_1	3.6	2.0	--
R_1-R_2	10.3	7.9	8.3

Scheme 17. Reaction mechanism for the second oxidative addition and reductive elimination of both aryl halides (1a) and monofluoroalkyl halides (2a). This mechanism corresponds to the evolution of the I4 (1a) i.e., first oxidative addition process involving 1a. Gibbs free energies in kcal/mol.

In fact, the C-C coupling presents the lowest barrier from intermediate **I9**, which at the same time is the lowest energy reductive elimination promoter. On one hand, the **1a** homocoupling from this intermediate is assumed to be essentially barrierless, as this was suggested by potential energy scans, and it was not possible to locate the low energy transition state. On the other hand, the reductive elimination of the heterocoupling pathway occurs through a barrier of 8.3 kcal/mol. Although **I9** presents the lowest energy pathway, the

necessity to reach the species through the prior formation of **I8**, implies that the reductive elimination from **I9** competes with the one from **I7**.

As already stated, the mechanism starting from $\mathbf{I4_{2a}}$ follows the same path, with small differences on the energies of intermediates and transition states (Scheme 18). Once again, the oxidative addition occurs through a halide abstraction and favors the **2a** substrate. The situation for the reductive elimination is also similar to the scenario starting from $\mathbf{I4_{1a}}$. There are three different Ni^{III} species that can promote the C-C coupling. However, intermediate **I8** is considerably high in energy (in comparison to **I7** and **I9**) and therefore, the reductive elimination from the intermediate is highly disfavored (Scheme 18, table).

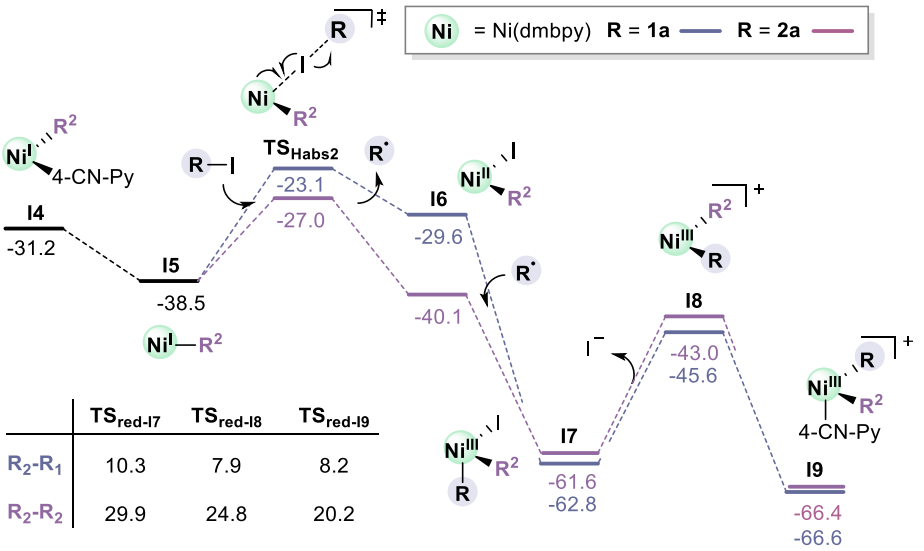

Scheme 18. Reaction mechanism for the second oxidative addition and reductive elimination of both aryl halides (1a) and monofluoroalkyl halides (2a). This mechanism corresponds to the evolution of the I4 (2a) i.e., first oxidative addition step involving 2a. Gibbs free energies in kcal/mol.

Still, the relative energy for the reductive elimination are similar for the three intermediates. In this case, we observe a strong dependance with orbital hybridization, *e.g.*, from intermediate **I7**, the reductive elimination to form the

heterocoupling product is found at 10.3 kcal/mol, while the **2a** homocoupling involves a kinetically prohibitive process of 29.9 kcal/mol.

After the reductive elimination step and the release of the product, the catalyst must reenter to the catalytic cycle. This process differs depending on the nickel species involved on the reductive elimination **I7**, **I8** or **I9** which yield **I10**, **I11** and **I12**, respectively (Scheme 19). These species can be easily converted into **I1** through a reduction combined with diverse ligand exchanges.

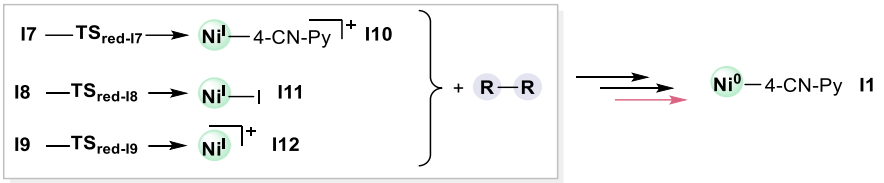

Scheme 19. Catalyst species obtained after the reductive elimination and interconversion to form I1 and re-enter to the catalytic cycle.

The mechanism presented above implies a complex scenario with a high number of competing paths that encumber the prediction of the reaction outcome. In cross-electrophiles mechanisms, the selectivity is typically determined in the oxidative addition steps. In the present system, both $\mathbf{TS_{habs1}}$ and $\mathbf{TS_{habs2}}$ favour the oxidative addition of **2a**, which would lead to the selective formation of the **2a** homocoupling product. However, the barrier through $\mathbf{TS_{red}}$ to form the **2a** homocoupling product is considerably higher in comparison to **1a** homocoupling and heterocoupling pathways. In fact, the transformation is kinetically prohibitive with the most accessible reductive elimination promoter, **I7**. Therefore, it is not trivial to determine which product will be preferentially formed.

The energetic profile description is not enough for intricated mechanisms such as the one presented here. Hence, the computed Gibbs free energies have been converted into rate constants and then introduced into a microkinetic model.

Table 1 shows all the barriers and kinetic constants included in the microkinetic model for both direct and reverse reactions.

Please notice that the different reactions in Table 1 have been coloured according to the nature of the process. Reactions in grey are those that proceed without transition state and are considered under diffusion control. In these reactions the barrier has been approximated *via* Stokes-Einstein equation with Smoluchowski formulation (see theoretical background). Then, reactions in pink represent redox processes in which the barrier has been approximated using a thermodynamic cycle. Finally, the reactions in black represent those involving a transition state.

Table 2. Chemical reactions included in the conventional cross-electrophile mechanism variant. Barriers (kcal/mol) and kinetic constants (s^{-1}) of both direct and reverse reaction.

Label	Chemical reaction	Direct		Reverse	
		Barrier	Kinetic constant	Barrier	Kinetic constant
R0	I0 + 4-CNPy ⇄ I1 +dmbpy	4.0	1.0615E+10	5.60	8.0483E+08
R1	I1 + 2a ⇄ I2 + 2a.	6.9	1.0207E+08	19.9	8.5122E-02
R2	I1 + 1a ⇄ I2 + 1a.	11.1	1.0864E+05	12.7	9.0928E+03
R3	I2 + Mn ⇄ I1 + MnI_2	4.0	1.0615E+10	7.3	5.6289E+07
R4	I2 + 2a. ⇄ $I3_{2a}$	4.0	1.0615E+10	26.7	1.5397E-06
R5	I2 + 1a. ⇄ $i3_{1a}$	4.0	1.0615E+10	37.2	7.3786E-14
R8	$I3_{2a}$ + Mn ⇄ $I4_{2a}$ + MnI_2	4.0	1.0615E+10	7.5	4.0773E+07
R9	$I5_{2a}$ + 2a ⇄ $i6_{2a}$ + 2a.	9.6	1.3928E+06	12.1	2.3398E+04
R10	$I5_{2a}$ + 1a ⇄ $i6_{2a}$ + 1a.	13.6	2.1898E+03	4.7	3.6922E+09
R11	$I5_{2a}$ + 2a ⇄ $i6_{2a}$ + 2a.	8.9	3.9997E+06	8.4	8.6627E+06
R12	$I5_{2a}$ + 1a ⇄ $i6_{2a}$ + 1a.	12.3	1.5776E+04	0.4	3.4294E+12
R17	$I7_{hom2a}$ ⇄ I10 + $Prod_{hom2a}$	30.0	8.0170E-09	63.8	1.7910E-32
R18	$I7_{het}$ ⇄ I10 + $Prod_{het}$	10.3	4.0481E+05	45.5	1.0508E-19

R19	$I7_{hom1a} \rightleftarrows I10 + Prod_{hom1a}$	3.7	1.8530E+10	38.2	1.4879E-14
R20	$I3_{1a} + Mn \rightleftarrows i4_{1a} + MnI_2$	4.0	1.0615E+10	8.3	1.0427E+07
R30	$I8_{hom2a} \rightleftarrows I11 + Prod_{hom2a}$	7.9	2.0602E+07	45.6	9.0396E-20
R31	$I8_{het} \rightleftarrows I11 + Prod_{het}$	24.8	3.0680E-05	62.2	2.4057E-31
R32	$I8_{hom1a} \rightleftarrows I11 + Prod_{hom1a}$	2.1	2.4308E+11	40.2	5.7083E-16
R33	$I4_{2a} \rightleftarrows I5_{2a}$ + 4-CNPy	6.2	2.9217E+08	4.0	1.0615E+10
R34	$I4_{1a} \rightleftarrows I5_{1a}$ + 4-CNPy	4.0	1.0615E+10	5.2	1.5663E+09
R42	$I7_{het} \rightleftarrows I9_{het}$ + 4-CNPy	26.9	1.0595E-06	4.0	1.0615E+10
R43	$I7_{hom2a} \rightleftarrows I9_{hom2a}$ + 4-CNPy	29.3	2.3512E-08	4.0	1.0615E+10
R44	$I7_{hom1a} \rightleftarrows I9_{hom1a}$ + 4-CNPy	18.4	9.3481E-01	4.0	1.0615E+10
R45	$I9_{het} + I^- \rightleftarrows I8_{het}$	4.0	1.0615E+10	23.1	4.5097E-04
R46	$I9_{hom2a} + I^- \rightleftarrows I8_{hom2a}$	4.0	1.0615E+10	24.5	4.8194E-05
R47	$I9_{hom1a} + I^- \rightleftarrows I8_{hom1a}$	4.0	1.0615E+10	13.5	2.2996E+03
R48	$I3_{2a} \rightleftarrows I6_{2a}$ + 4-CNPy	16.5	2.0023E+01	4.0	1.0615E+10
R49	$I3_{1a} \rightleftarrows I6_{1a}$ + 4-CNPy	15.2	1.4949E+02	4.0	1.0615E+10
R52	$I6_{2a}$ + 1a. $\rightleftarrows I8_{het}$	4.0	1.0615E+10	39.1	3.0545E-15
R53	$I6_{2a}$ + 2a. $\rightleftarrows I8_{hom2a}$	4.0	1.0615E+10	26.5	2.2057E-06
R54	$I6_{1a}$ + 1a. $\rightleftarrows I8_{hom1a}$	4.0	1.0615E+10	40.5	3.5155E-16
R55	$I6_{1a}$ + 2a. $\rightleftarrows I8_{het}$	4.0	1.0615E+10	27.4	4.7585E-07
R59	$I10 + I^- \rightleftarrows I2$	4.0	1.0615E+10	5.5	9.9034E+08
R60	I11 + 4-CNPy $\rightleftarrows$ I2	4.0	1.0615E+10	6.7	1.3765E+08
R61	$I12 + I^- \rightleftarrows I11$	4.0	1.0615E+10	23.2	4.0938E-04
R62	$I9_{het} \rightleftarrows I12 + Prod_{het}$	8.2	1.1485E+07	45.9	5.5513E-20
R63	$I9_{hom2a} \rightleftarrows I12 + Prod_{hom2a}$	20.2	4.9175E-02	59.0	4.5394E-29
R64	$I9_{hom1a} \rightleftarrows I12 + Prod_{hom1a}$	*Introduced as a diffusion process (TS not found)*			

Diffusion controlled process
Redox process
Transition state controlled process

The results obtained with the microkinetic model are shown in Figure 1. The parameters used for the study are explained in the computational details section. Unfortunately, the results obtained strongly disagree with the experimental yields. First, **1a** and **2a** homocouplings products are obtained in 8% and <1% yields, respectively. More critically, only a 1% of the desired cross-coupling product is observed. A detailed analysis of the results shows the preferential formation of the **(I7-I9)$_{hom2a}$** reductive elimination precursors. However, the reductive elimination process is kinetically prohibited from **I7$_{hom2a}$** and **I8$_{hom2a}$** and highly demanding from **I9$_{hom2a}$**. This situation generates a catalyst blockage before the reductive elimination that prevents the transformation to occur in the elapsed time.

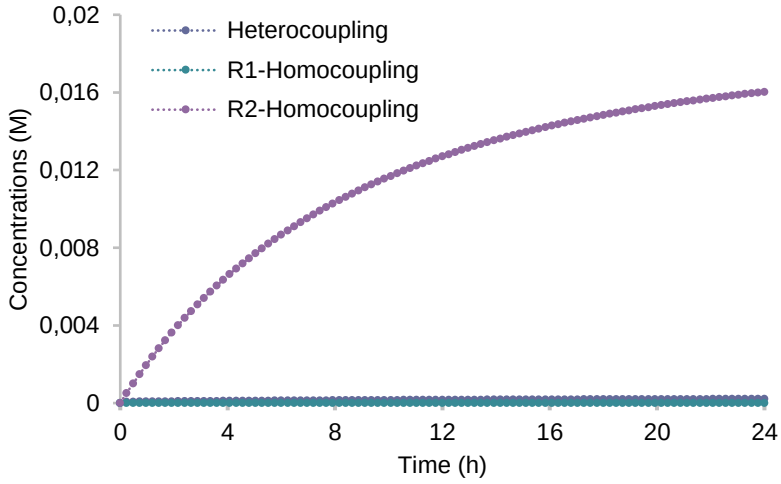

Figure 1. Theoretical evolution of the concentration of the different products within 24h of reaction time for the classic cross electrophile mechanism model.

There are two elements on this mechanistic scenario that disagree with experiments: (i) The reaction is not productive within the experimental time. This could be potentially attributed to an error on the methodology employed as small differences on the barriers could imply higher yields. (ii) The wrong selectivity obtained pointing towards the formation of the **2a** homocoupling product. In this case the error cannot be attributed to the methodology as it

seems qualitatively consistent with the overall results. Instead, we must envisage an error on the model, *i.e*. the reaction proceeds through a different mechanism.

Expanded cross-electrophile mechanism

At this point, the model was expanded by the incorporation of alternative reaction paths. First, we envisaged that Mn could reduce all the Ni-I species present in the reaction media as the reductant is present in superstoichiometric amounts. Second, since nickel is known for its high radical affinity, we expanded the radical trapping to all the nickel species in the reaction media (Scheme 19).

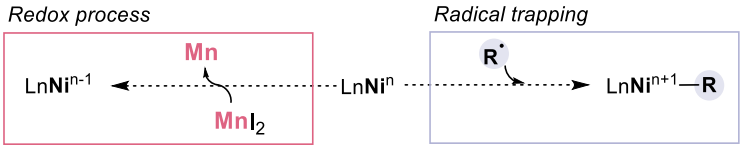

Scheme 19. Alternative paths included in the reaction scenario: the presence of higher number of redox process (left) and the possible radical trapping by other species in the reaction media (right).

In this second scenario, all the alternative reaction paths have been incorporated to the conventional cross-electrophile mechanism shown in the previous section. To facilitate the discussion, we will present a general picture of the reaction mechanism in which the light colours represent the steps conforming the classic cross-electrophile pathway, and the dark colours correspond to the newly added steps *i.e.,* extra reductions and radical trappings. As we did in the previous section, we will divide the mechanism in three different schemes: Scheme 20 depicts the pathway for the first oxidative addition while Scheme 21 and Scheme 22 show the second oxidative addition taking as starting point **I4$_{1a}$** and **I4$_{2a}$**, respectively.

One of the additional reaction paths is based on the potential reduction of other Ni-I species present in the catalytic cycle. This implies that after the first oxidative addition step, which forms intermediate **I2** and the corresponding radical (Scheme 20), the system can evolve trough two different paths: (i) the nickel centre can trap the radical forming the Ni^{II} species **I3** (as in the classic cross electrophile mechanism) or (ii) intermediate **I2** can react with manganese in a redox reaction to recover the active species **I1**. The latter occurs through a thermodynamically favourable process of -3.5 kcal/mol. Notice that this reaction energy does not correspond to the difference between the intermediates in the reaction path. In fact, in the profile the reduction from **I2** to **I1** appears to be endergonic. This is due to the use of a thermodynamic cycle to compute the values for redox processes, which implies a modification of the reference point. The Mn reductions (pink lines) have only been included in the schemes aiming to provide a general picture of the mechanism and the different competing paths involved. Besides, all the redox reactions in the catalytic cycle, together with their reaction energies are depicted in Scheme 23.

Since both competing pathways from **I2** (radical trapping and reduction) are exergonic and controlled by diffusion, the concentration will play an important role on the discrimination between pathways. Thus, the presence of superstoichiometric amounts of Mn, will tip the balance towards the reduction of **I2**. This preference towards the **I2** reduction implies the continuous generation of radical species through a Ni^{I}-Ni^{0} catalytic cycle. Still, without the general picture of the mechanism and a microkinetic analysis we cannot draw any conclusion about the implications of this new scenario.

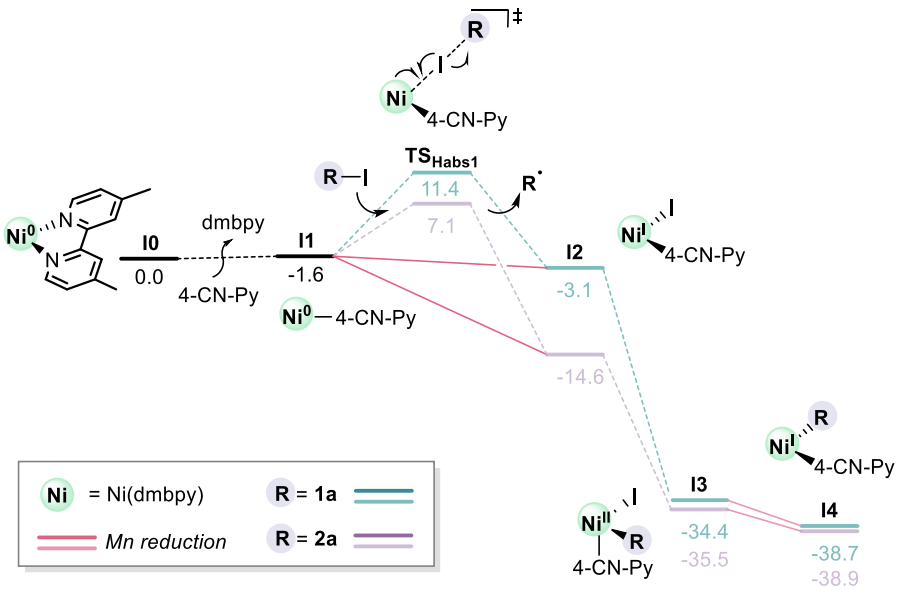

Scheme 20. Reaction mechanism for the first oxidative addition of both aryl halides (1a) and monofluoroalkyl halides (2a). The light lines represent the steps present in the classic cross-electrophlile mechanism and the dark lines the alternative reaction paths included. Gibbs free energies in kcal/mol.

In the second part of the mechanism we first included potential radical trappings by other species in the reaction media. Although we could envisage the raddical addition to any intermediate, we discarted those with high valent nickel species (**I7**-**I9**) since it would imply the formation of highly instable Ni^{IV} intermediates. There are two possible raddical additions to low valent nickel species: to **I4** and to **I5**, which yield the highly stable Ni^{II} intermediates **I13** and **I14**, respectively (Scheme and Scheme). Both **I13** and **I14** could potentially be precursors of the reductive elimination and since they are in equilibrium, we have computed the reductive elimination transition state from the most stable intermediate (**I13**). The process is highly energetic in comparison to the analogous Ni^{III} reductive elimination precursors: 20.4 kcal/mol for the **1a** homocoupling product, 19.5 kcal/mol for the heterocoupling product (Scheme) and 45.4 kcal/mol for the **2a** homocoupling product (Scheme).

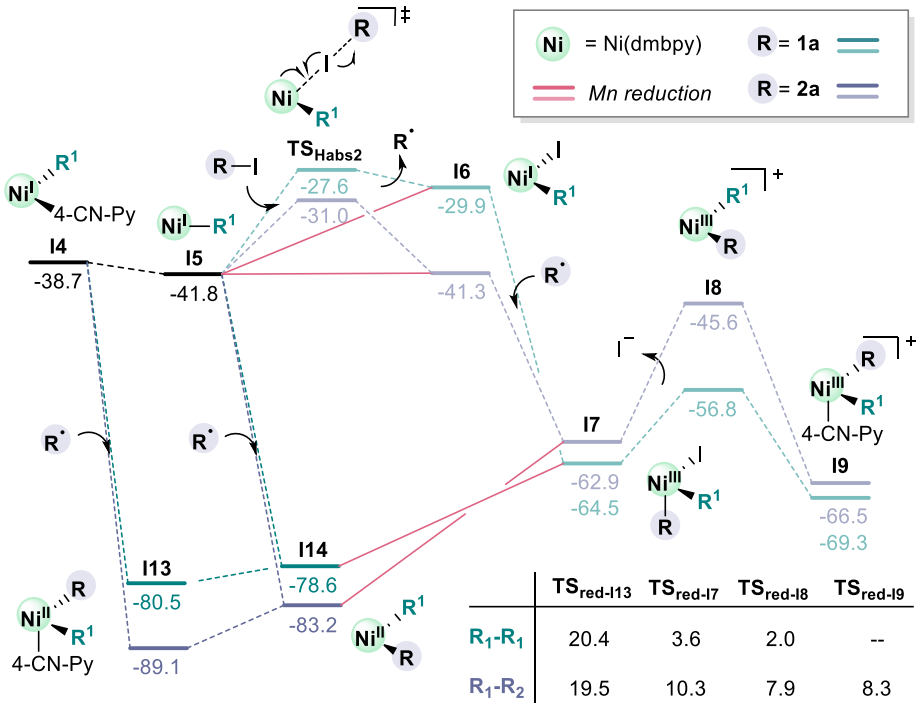

	$TS_{red\text{-}I13}$	$TS_{red\text{-}I7}$	$TS_{red\text{-}I8}$	$TS_{red\text{-}I9}$
R_1-R_1	20.4	3.6	2.0	--
R_1-R_2	19.5	10.3	7.9	8.3

Scheme 21. Reaction mechanism for the second oxidative addition and reductive elimination of both aryl halide (1a) and monofluoroalkyl halide (2a). The mechanism corresponds to the evolution of the $I4_{1a}$. The light lines represent the steps present in the classic cross-electrophlile mechanism and the dark lines the alternative reaction paths included. Gibbs free energies in kcal/mol.

On the other hand, we considered the reduction of any Ni-I intermediates present in the reaction mechanism (**I6** and **I7**). Intermediate **I6** is reduced in an exergonic step to form **I5** that can either undergo again the oxidative addition process ($\mathbf{TS_{habs2}}$) or trap the released radical yielding **I14**. This reduction is analogous to the one occurring after the first oxidative addition (from **I2** to **I1**). The presence of high concentration of Mn, will incline the mechanism towards the reduction, leading to the continuous generation of radicals through a Ni^{II}-Ni^{I} catalytic cycle.

The reduction of **I7** yields the Ni^{II} species **I14**, which rapidly coordinates a 4-CNPy ligand yielding **I13**. This redox reaction competes with two other transformations; the direct reductive elimination and the decoordination of one iodine atom to form **I8**. Since, the reduction is the only exergonic and barrierless step, intermediate **I7** will preferentially evolve towards that path leading to a slower reductive elimination (prohibitive in the **2a** homocoupling) since it occurs on a Ni^{II} instead of a Ni^{III} species (Scheme and Scheme).

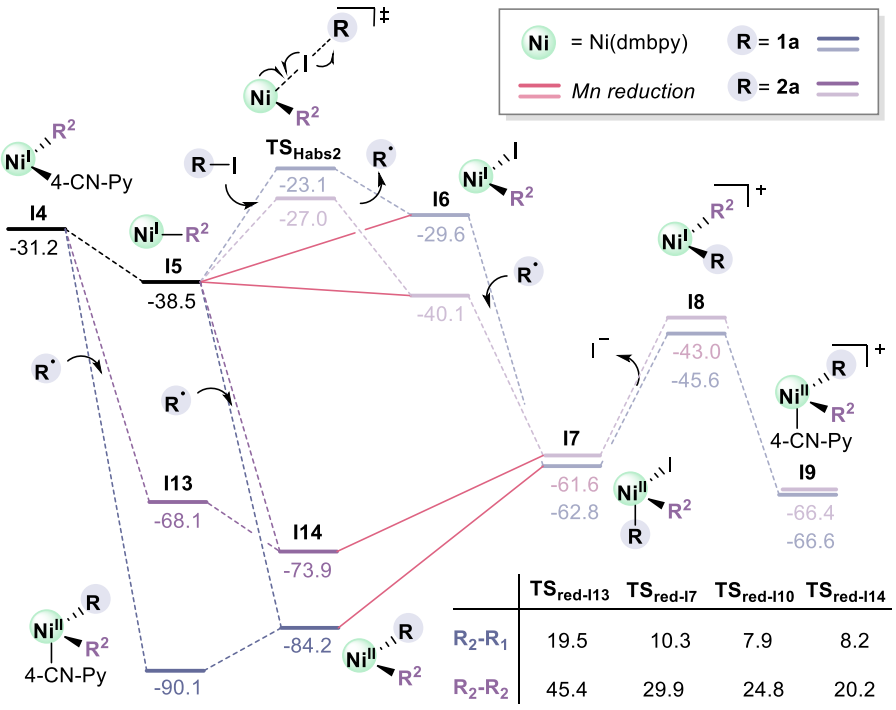

Scheme 22. Reaction mechanism for the second oxidative addition and reductive elimination of both aryl halides (1a) and monofluoroalkyl halides (2a). The mechanism shows to the evolution of the $I4_{2a}$. The light lines represent the steps present in the classic cross-electrophlile mechanism and the dark lines the alternative reaction paths included. Gibbs free energies in kcal/mol.

Finally, after the reductive elimination, the resulting species are converted into **I1** so that they can reenter the catalytic cycle. This process has been shown in

the previous section for **I7**, **I8**, **I9**. In this case, we have an extra reductive elimination process from **I13**, however this reductive elimination yields directly **I1**, so the catalyst can directly restart the catalytic cycle without any further conversion.

As noted above, reaction energies of the redox processes do not correspond to the difference between the intermediates shown in the reaction path. Scheme 23 collects the thermodynamic values for all the redox steps in the system. All the computed reactions are found to be exergonic, with reductions of higher valent species (**I6** and **I7**) presenting more thermodynamically favorable steps. Interestingly, the redox reactions from **I3** to **I4**, which is the only one included in the classic cross electrophile mechanism are among the less favorable reduction processes (Scheme 23, bold). Therefore, when performing a computational study of systems involving reductants, it is crucial to incorporate all side reactions arising from the reduction of higher valent species, as they can induce a change in the overall scenario.

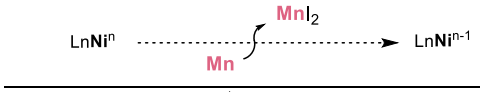

Reactants	Products	Reaction energy (kcal/mol)
I2	**I1**	-3.3
$\mathbf{I3}_{\mathbf{2a}}$	$\mathbf{I4}_{\mathbf{2a}}$	-3.5
$\mathbf{I3}_{\mathbf{1a}}$	$\mathbf{I4}_{\mathbf{1a}}$	-4.3
$\mathbf{I6}_{\mathbf{2a}}$	$\mathbf{I5}_{\mathbf{2a}}$	-16.7
$\mathbf{I6}_{\mathbf{1a}}$	$\mathbf{I5}_{\mathbf{1a}}$	-13.7
$\mathbf{I7}_{\mathbf{hom2a}}$	$\mathbf{I13}_{\mathbf{hom2a}}$	-12.3
$\mathbf{I7}_{\mathbf{hom1a}}$	$\mathbf{I13}_{\mathbf{hom1a}}$	-21.0
$\mathbf{I7}_{\mathbf{het}}$	$\mathbf{I13}_{\mathbf{het}}$	-21.4

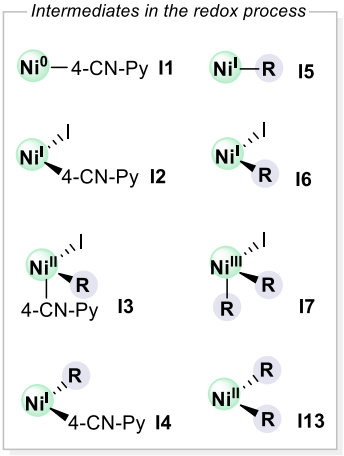

Scheme 23. Reaction energies for all the redox steps in the system obtained via a thermodynamic cycle. Gibbs free energies in kcal/mol.

Overall, the expansion of the classic cross-electrophile mechanism induces an extra layer of complexity in the reaction mechanism. Obviously, as both radical trapping and redox reactions occur through diffusion-controlled processes, the concentration is crucial to discriminate between paths. The combination of a complex mechanism with critical effect of the concentration forces again the application of a microkinetic model. The barriers and kinetic constants included in the microkinetic model for both direct and reverse reactions are shown in Table 2 and Table 3.

Table 3. Chemical reactions included (additional to those in the previous section; conventional cross-electrophile mechanism variant) in the extended cross-electrophile mechanism model. Barriers (kcal/mol) and kinetic constants (s^{-1}) of both direct and reverse reaction.

Label	Chemical reaction	Direct		Reverse	
		ΔG (kcal/mol)	*k*	ΔG (kcal/mol)	*k*
R6	$I3_{2a}$ + 1a. ⇄ $I7_{het}$ + I^-	4.0	1.0615E+10	30.4	3.8044E-09
R7	$I3_{2a}$ + 2a. ⇄ $I7_{hom2a}$ + I^-	4.0	1.0615E+10	18.7	5.7048E-01
R13	$I3_{2a}$ + 1a. ⇄ $I8_{het}$ + 4-CNPy	4.0	1.0615E+10	26.7	1.6193E-06
R14	$I3_{2a}$ + 2a. ⇄ $I8_{hom2a}$ + 4-CNPy	4.0	1.0615E+10	14.0	1.1693E+03
R15	$I3_{1a}$ + 1a. ⇄ $I8_{hom1a}$ + 4-CNPy	4.0	1.0615E+10	29.2	2.4963E-08
R16	$I3_{1a}$ + 2a. ⇄ $I8_{het}$ + 4-CNPy	4.0	1.0615E+10	16.2	3.3789E+01
R21	$I3_{1a}$ + 2a. ⇄ $I7_{het}$ + I^-	4.0	1.0615E+10	19.9	7.9386E-02
R22	$I3_{1a}$ + 1a. ⇄ $I7_{hom1a}$ + I^-	4.0	1.0615E+10	34.1	1.0148E-11
R23	$I4_{2a}$ + 1a. ⇄ $I13_{het}$	4.0	1.0615E+10	38.7	6.1320E-15
R24	$I4_{2a}$ + 2a. ⇄ $I13_{hom2a}$	4.0	1.0615E+10	28.7	6.4824E-08
R25	$I4_{1a}$ + 1a. ⇄ $I13_{hom1a}$	4.0	1.0615E+10	44.0	1.3194E-18
R26	$I4_{1a}$ + 2a. ⇄ $I13_{het}$	4.0	1.0615E+10	27.4	5.0022E-07
R27	I8 ⇄ I1 + $Prod_{het}$	19.5	1.6937E-01	47.7	3.5132E-21
R28	I8* ⇄ I1 + $Prod_{hom2a}$	45.4	1.2626E-19	70.6	3.1970E-37

R29	I8** ⇄ I1 + $Prod_{hom1a}$	20.4	3.9709E-02	45.4	1.2347E-19
R35	$I5_{2a}$ + 1a. ⇄ $I14_{het}$	4.0	1.0615E+10	46.8	1.3007E-20
R36	$I5_{2a}$ + 2a. ⇄ $I14_{hom2a}$	4.0	1.0615E+10	25.1	2.0488E-05
R37	$I5_{1a}$ + 1a. ⇄ $I14_{hom1a}$	4.0	1.0615E+10	44.7	3.8798E-19
R38	$I5_{1a}$ + 2a. ⇄ $I14_{het}$	4.0	1.0615E+10	32.1	2.6126E-10
R39	$I13_{het}$ ⇄ $I14_{het}$ + 4-CNPy	4.0	1.0615E+10	9.9	8.1803E+05
R40	$I13_{hom2a}$ ⇄ $I14_{hom2a}$ + 4-CNPy	9.8	9.2444E+05	4.0	1.0615E+10
R41	$I13_{hom1a}$ ⇄ $I14_{hom1a}$ + 4-CNPy	4.0	1.0615E+10	6.0	4.6057E+08
R50	$I6_{2a}$ + Mn ⇄ $I5_{2a}$ + MnI_2	4.0	1.0615E+10	17.7	2.7872E+00
R51	$I6_{1a}$ + Mn ⇄ $I5_{1a}$ + MnI_2	4.0	1.0615E+10	20.7	2.1602E-02
R56	$I7_{het}$ + Mn ⇄ $I14_{het}$ + MnI_2	4.0	1.0615E+10	25.4	1.1847E-05
R57	$I7_{hom2a}$ + Mn ⇄ $I14_{hom2a}$ + MnI_2	4.0	1.0615E+10	16.3	2.5897E+01
R58	$I7_{hom1a}$ + Mn ⇄ $I14_{hom1a}$ + MnI_2	4.0	1.0615E+10	25.0	2.3816E-05

Diffusion controlled process
Redox process
Transition state controlled process

The results obtained with the microkinetic analysis for the expanded cross-electrophile model are shown in Figure 2 (see computational details section for the parameters employed). Once again, the results obtained strongly disagree with the experimental yields. In this case, we can observe lower yields in comparison to the previous model: all products are obtained in yields under 1%. This situation arises due to a high concentration of the Ni^{II} species **I13** and **I14** which are not productive or present a high barrier for the reductive elimination, leading to a catalyst blockage. Besides, this situation is enhanced due to the straightforward formation of these species, either by radical trapping or through the reduction of Ni^{III}-I to the analogous Ni^{II} species.

Nevertheless, we can observe some differences in comparison with the previous model. The most notorious is the change on the selectivity observed. Whereas in the classic cross electrophile variant the **2a** homocoupling product

was obtained in 8% yield (Figure 1), here no conversion is observed within 24h. This is because the reductive elimination, which was difficult from the Ni^{III} species, is completely prohibitive from the Ni^{II} species, with a barrier of 45.4 kcal/mol. Therefore, although both oxidative additions are selective towards the **2a**, the extremely disfavored reductive elimination impedes the formation of the **2a** homocoupling product. Conversely, the reductive eliminations to form the **1a** homocoupling and the heterocoupling products are productive, however, the concentration of **1a** radical is extremely low, a fact that hampers the formation of the reductive elimination precursors and makes the products highly inaccessible.

The inclusion of alternative reaction paths did not improve the agreement with experimental results. The reaction is still not productive within the experimental time and the selectivity points towards the formation of the **1a** homocoupling product. These results indicate that we must further refine the model to get a proper description of the system.

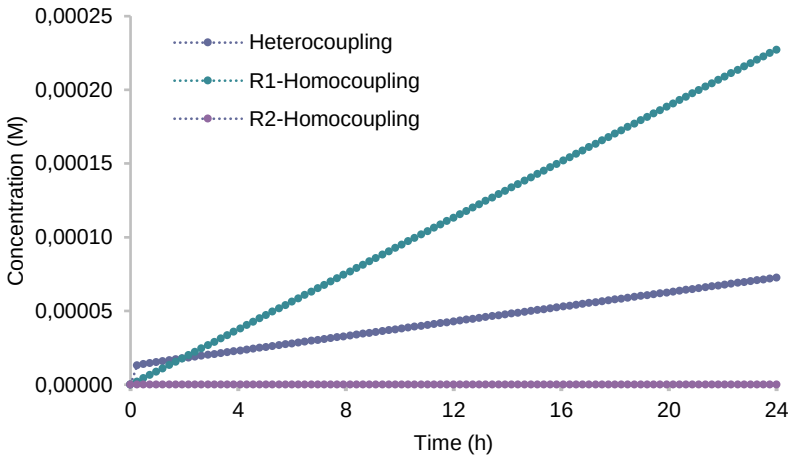

Figure 2. Predicted evolution of the concentration of the different products within 24h of reaction time for the expanded classic cross electrophile mechanism model.

Substrate radical trapping mechanism

At this stage, we set our attention to the formation of the organic radical species and their reactivity. As explained in the previous section, after the halide abstraction the nickel centre can either trap the radical species or be reduced by manganese. The presence of the reductant in superstoichiometric amounts can drive the reaction towards the reduction recovering the nickel species prior to the halide abstraction. This reactivity leads to two catalytic cycles devoted to the radical formation: the first oxidative addition leads to a Ni^0-Ni^I cycle (Scheme 23, Path A) and the second to a Ni^I-Ni^{II} cycle (Scheme 23, Path B). Both processes yield organic radicals which due to their high instability can be easily trapped by any species in the reaction media. Although nickel is known for its affinity towards radical species, it exists in low concentration in the reaction medium. Thus, we explored the possibility of a substrate radical trap (Scheme 23).

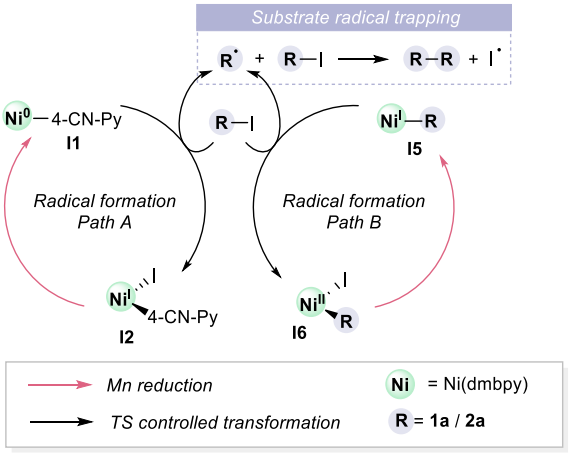

Scheme 23. Catalytic cycles for the radical formation arising from the presence of reductant and the subsequent radical trapping by the substrates yielding the coupling product. Two possible pathways for the radical formation, one for each oxidative addition event: Ni^0-Ni^I (Path A) or Ni^I-Ni^{II} (Path B).

The substrate radical trapping occurs through a S_N2 alike transition state (**TS_{SRT}**), which releases an iodine radical that is rapidly trapped by the manganese (Scheme 24, 3D structure). There are four possible scenarios: (i) halide abstraction of **1a** and trapping of the radical with another **1a** substrate; leading to the **1a** homocoupling, (ii) halide abstraction of **1a** and trapping of the radical with a **2a** substrate; leading to the heterocoupling, (iii) halide abstraction of **2a** and trapping of the radical with another **2a** substrate; leading to the **2a** homocoupling and (iv) halide abstraction of **2a** and trapping of the radical with a **1a** substrate; leading to the heterocupling.

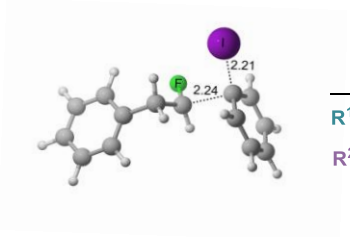

	$R^{1}\cdot$	$R^{2}\cdot$
R^{1}–I (**1a**)	12.6	15.5
R^{2}–I (**2a**)	32.6	40.9

Scheme 24. Gibbs free energies (kcal/mol) for the substrate radical trapping transition state (TS_{SRT}) and 3D structure of the TS_{SRT}. R^1 stands for the radical formed from 1a and R^2 the radical formed from 2a.

Both reactions with the aryl iodide (**1a**), proceed through an affordable barrier of 12.6 and 15.5 kcal/mol for the **1a** and **2a** radicals, respectively. However, the analogous process with 1-fluroro-1-iodoethylbenzene (**2a**) is completely prohibitive for both **1a** and **2a** radicals. Although the barriers obtained for the SRT process points out the preferential formation of the **1a** homocoupling product, we decided to apply a microkinetic analysis. This microkinetic model includes all the reactions discussed in this chapter: the barriers and kinetic constants for both direct and reverse reactions are shown in Table 2, Table 3 and Table 4.

Table 4. Chemical reactions included (apart from those in the previous section; extended cross-electrophile mechanism variant) in the substrate radical trapping mechanism model. Barriers (kcal/mol) and kinetic constants (s^{-1}) of both direct and reverse reaction.

Label	Chemical reaction	Direct		Reverse	
		Barrier	Kinetic constant	Barrier	Kinetic constant
R78	1a + 2a. ⇄ p-hetero	17.4	5.0209E+00	44.9	2.8477E-19
R79	2a + 2a. ⇄ p-homo	40.9	1.9360E-16	66.8	1.4119E-34
R80	1a + 1a. ⇄ p-homo*	14.5	4.9080E+02	55.5	1.1006E-26
R81	2a + 1a. ⇄ p-hetero	34.5	5.1897E-12	73.5	2.9327E-39

The results obtained with the microkinetic analysis for the substrate radical trapping model are shown in Figure 3 (see computational details section for the parameters employed). Unexpectedly, although the most favourable SRT reaction would lead to the **1a** homocoupling product ($\Delta\Delta G^{\ddagger}$ = 2.9 kcal/mol), the model predicts a selective formation (80%) of the heterocoupling product. By contrast, only 10% and <1% yield is obtained for **1a** homocoupling and **2a** homocoupling products, respectively. This result is in very good agreement with experiment, and we consider that this is thus the valid mechanism.

This counterintuitive result owes to the radical distribution. Since both halide abstractions are selective towards **2a**, the concentration of **2a** radical is significantly higher than the concentration of **1a** radical. This allows the **2a** radicals to react with **1a** substrate obtaining the desired cross-coupling product.

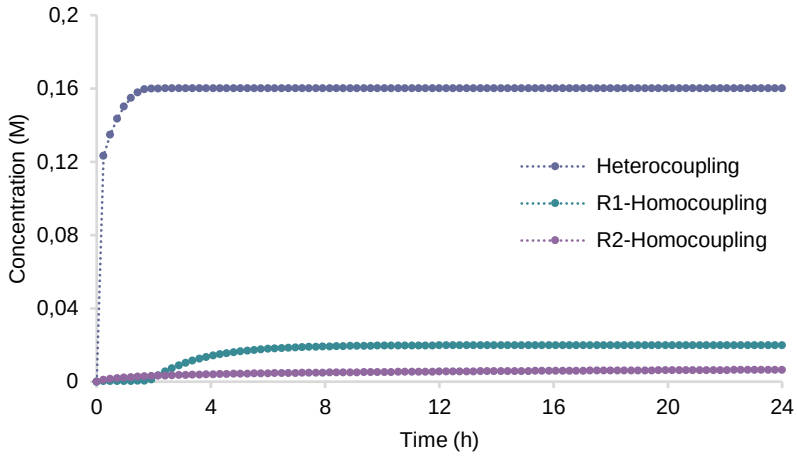

Figure 3. Predicted evolution of the concentration of the different products within 24h of reaction time for the substrate radical trapping model.

6. Summary

The complete scenario for the reductive coupling of aryl halides with monofluoroalkyl halides has been fully characterized and confirmed to reproduce experimental results through the application of microkinetic models. Three variations of the mechanism have been explored, each of them including more steps than the previous one: (i) conventional cross-electrophile mechanism, (ii) extended cross electrophile mechanism, including extra radical trappings and reduction steps and (iii) substrate radical trapping. The overall mechanism results in a highly complex scenario with numerous side reactions and deactivations of the catalyst. A simplified picture of the transformation is shown in Scheme 25. Notice that, some steps involving radical trappings and formation of off-cycle species, have been omitted for the sake of clarity.

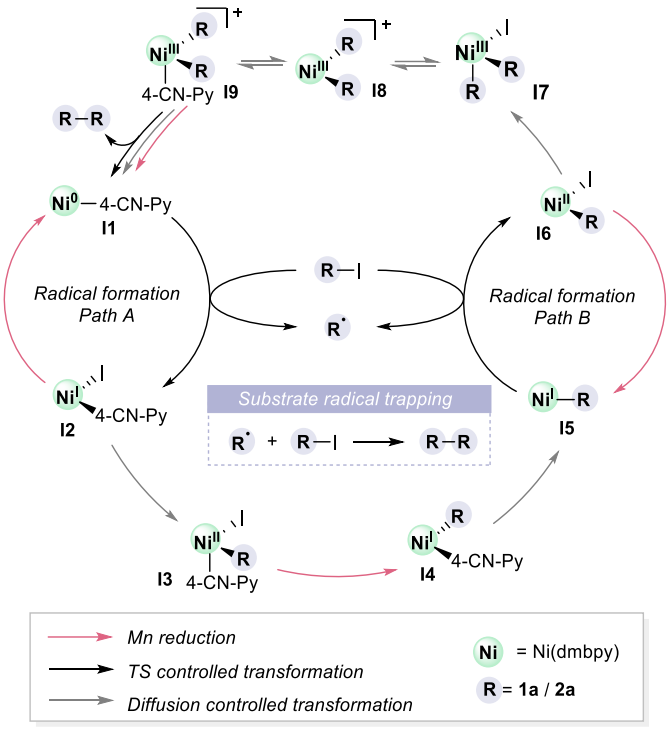

Scheme 25. Simplified picture of the reductive coupling of aryl halides with monofluoroalkyl halides mechanism.

Our investigation shows that the conventional reductive coupling mechanism would yield only the monofluoroalkyl halide homocoupling product, contrary to the experimental results. The inclusion of extra radical trapping and reduction steps makes things worse, as it brings down yield further down, as it mostly provides a higher rate of catalyst poisoning. In this expanded mechanism, the Ni^{III} precursor is reduced to the analogous Ni^{II} species, a process that hinders the reductive elimination.

Remarkably, the conundrum is solved by the consideration of one-electron catalytic cycles yielding organic radicals (Scheme 25, Path A/B) which can then react with substrate molecules in a metal-free step, which we have labeled as substrate radical trapping reaction. The highly reactive radicals formed in the cycle react with a substrate molecule yielding the coupling product. This

substrate radical trapping is governing the cross-selectivity of the system: the oxidative addition is selective towards the formation of the Csp^3 radical which selectively reacts with the Csp^2 substrate achieving the desired heterocoupling product. To the best of our knowledge this is the first time that this alternative substrate radical trapping mechanism is proposed for reductive couplings, and we expect that it will play a role in other similar systems.

This study emerges as a great example of the evolution of the computational methodologies: it highlights the need of a microkinetic modeling to properly validate the computational results by reproducing the experimental findings in terms of evolution of concentrations through time.

UNIVERSITAT ROVIRA I VIRGILI
BEYOND CONVENTIONAL DFT CATALYSIS: MECHANOCHEMISTRY AND SOLID REDUCTANTS
Bruna Sánchez Pladevall

Chapter III. "Amine as leaving group in C-C coupling under reductive conditions"

UNIVERSITAT ROVIRA I VIRGILI
BEYOND CONVENTIONAL DFT CATALYSIS: MECHANOCHEMISTRY AND SOLID REDUCTANTS
Bruna Sánchez Pladevall

1. Introduction

The C-N bond is among the most abundant chemical bonds in organic chemistry and biochemistry. Molecules presenting this structural motif present interesting and diverse biological activities.[1] Specifically, amines play an important role in biology since they are involved in the creation of amino acids, the building blocks of proteins, which are essential for life. In addition, due to the high biological activity of amines, this functional group is present in myriads of pharmaceutical agents.[2] Therefore, it is understandable that many efforts have been devoted to the development of transformations involving the formation or cleavage of these C-N bonds.

Transition metal catalysis has emerged as a powerful tool to forge C-N bonds in organic synthetic chemistry with methodologies such as Buchwald-Hartwig amination,[3] Ullmann coupling[4] or Chan-Lam coupling.[5] These bond formation strategies have been widely explored, and account for several generations of catalysts achieving greater reaction scope and milder conditions.[6] In contrast, the inert nature of the C-N bonds,[7] especially when compared with other

1 (a) Olyaei, A.; Sadeghpour, M.; Khalaj, M. *RSC Advances*. **2020**, 10(51), 30265–30281. (b) Kerru, N.; Gummidi, L.; Maddila, S.; Gangu, K. K.; Jonnalagadda, S. B. *Molecules*, **2020**, 25(8), 1909-1957. (c) Jiang, C.; Huang, H.; Kang, X.; Yang, L.; Xi, Z.; Sun, H.; Pluth, M. D.; Yi, L. *Chemical Society Reviews*, **2021**, 50(13), 7436-7495.

2 McMurry, J. (2011). Organic Chemistry with Biological Applications (2), Cengage Learning.

3 Forero-Cortés, P. A.; Haydl, A. M. *Organic Process Research and Development*, 2019, 23(8), 1478–1483.

4 Khan, F.; Dlugosch, M.; Liu, X.; Banwell, M. G. *Accounts of Chemical Research*, **2018**, 51(8), 1784–1795.

5 Chen, J. Q.; Li, J. H.; Dong, Z. B. *Advanced Synthesis and Catalysis*, **2020**, 362(16), 3311–3331.

6 Bariwal, J.; Van Der Eycken, E. *Chemical Society Reviews*, **2013**, 42(24), 9283–9303.

7 Blanksby, S. J.; Ellison, G. B. *Acc. Chem. Res.*, **2003**, 36, 255−263.

common organic bonds, makes the selective cleavage of this bond an extremely challenging transformation (Scheme 1).

The rapid development of organometallic chemistry has led to impressive progress in the area of transition metal catalysed cleavage of inert bonds, in particular C-C,[8] C-O[9] and C-H[10] activation. Still, the cleavage of C-N bonds is far less explored and remains in a development stage. This transformation is particularly interesting because, in principle, it could give rise to two coupled catalytic cycles (Scheme 1) in which both C-[M] and N-[M] species are generated, i.e., two types of activated nucleophiles can be obtained. Then, each nucleophile could react with a coupling partner to form other C-R and N-R bonds. Therefore, in comparison to other C-X bond activation methods the use of a C-N activation approach enables high atom economy transformations becoming a powerful method for the construction of functionalized complex molecules.

C-N bond activation reactions are far from reaching the desired full atom economy. Still, over the last years, several progresses have been done on the development of novel and practical methodologies to achieve C-N bond cleavage. Most of the studies present N-containing compounds acting as C synthons.[11] In some others, albeit far less common, the N-containing

8 (a) Jun, C. *Chem. Soc. Rev.* **2004**, 33, 610–618. (b) To, C. T.; Chan, K. S *European Journal of Organic Chemistry*, **2019**, 39, 6581–6591.

9 Yamamoto, A. *Adv. Organomet. Chem.*, **1992**, 34, 111-147.

10 Gandeepan, P.; Müller, T.; Zell, D.; Cera, G.; Warratz, S.; Ackermann, L. *Chemical Reviews*, **2019**, 119(4), 2192–2452.

11 (a) Weires, N.A.; Baker, E.L.; Garg, N.K. *Nat. Chem*., **2016**, 8 75–79. (b) Cong, X.; Fan, F.; Ma, P.; Luo, M.; Chen, H.; Zeng, X. *J. Am, Chem. Soc.*, **2017**, 139, 15182–15190. (c) Jiang, X.; Zhang, M.M.; Xiong, W.; Lu, L.Q.; Xiao, W.J.; *Angew. Chem. Int. Ed*., **2019**, 58, 2402–2406. (d) Chen, Q.; Gao, F.; Tang, H.; Yao, M.; Zhao, Q.; Shi, Y.; Dang, Y.; Cao, C. *ACS Catal.*, **2019**, 9, 3730–3736.

compounds act as N synthons.[12] Finally, some studies use both the C and N containing moieties, reaching the optimal atom economy. However, the types of target products that can be obtained are very limited.[13]

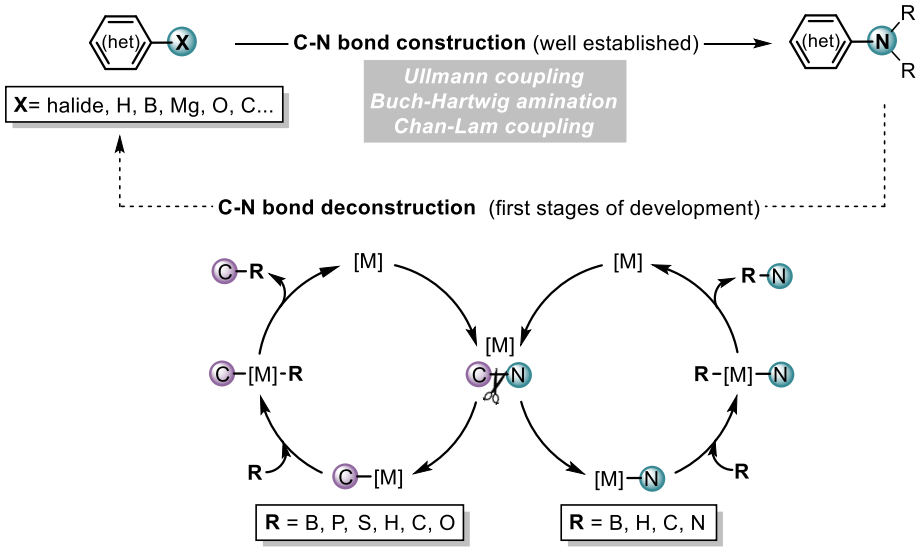

Scheme 1. Construction and deconstruction of C-N bonds with a selection of the currently available C-N bond formation strategies (top) and schematic representation of a full atom economy catalytic cycle (bottom).

The improvement of these atom-economy processes and the expansion of the scope remains a promising field which has received the attention of many research groups in the last decade, undergoing an exponential growth and a fast

12 (a) Li, B.; Xu, H.; Wang, H.; Wang, B. *ACS Catal*., **2016**, 6, 3856–3862. (b) Hu, F.; Lalancette, R.; Szostak, M.; *Angew. Chem. Int. Ed.*, **2016**, 55, 5062–5066. (c) He, Y.; Zheng, Z.; Liu, Q.; Song, G.; Sun, N.; Chai, X. *J. Org. Chem*., **2018**, 83, 12514–12526. (d) Li, Z.; Liu, L.; Xu, K.; Huang, T.; Li, X.; Song, B.; Chen, T. *Org. Lett.*, **2020**, 22, 5517–5521.

13 (a) Liu, Y.; Xie, Y.; Wang, H.; Huang, H. *J. Am. Chem. Soc*., **2016**, 138, 4314–4317. (b) Han, D.; He, Q.; Fan, R. *Nat. Commun.*, **2018**, 9, 3423. (c) Hao, W.; Wu, X.; Sun, J.Z.; Siu, J.C.; MacMillan, S.N.; Lin, S. *J. Am. Chem. Soc.*, **2017**, 139, 12141–12144.

development.[14] In this context, the improvement of the mechanistic understanding aided the design of more efficient transformations. The transition metal catalysed C-N bond cleavage reaction pathways can be divided into three main types: (1) *via* oxidative addition (of the C-N bond) with low valent transition metals (2) *via* β-N elimination, (3) *via* C-H bond cleavage triggered C-N bond activation (Scheme 2). [15]

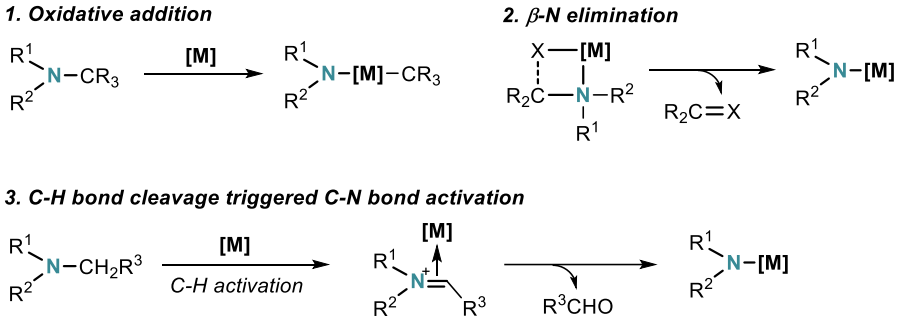

Scheme 2. Main pathways for the transition metal catalysed C-N activation.

Focusing on the oxidative addition pathway, the most common reactions where we find this type of activation are cross-coupling reactions. Although metal-catalysed cross-coupling is a well-established field with large history, during the last decades many research groups have focused on the expansion of its frontiers. One of these promising fields involves the use of new classes of electrophiles, such as those containing strong C-N bonds.

It is worth mentioning here that N-containing compounds present significant differences in reactivity depending on the nature of the bond. In fact, according to the literature, C-N bonds are divided into (Scheme 3): activated or high

14 Liu, J.; Yang, Y.; Ouyang, K.; Zhang, W.-X. *Green Synthesis and Catalysis*, **2021**, 2(2), 87–122.

15 Ouyang, K.; Hao, W.; Zhang, W. X.; Xi, Z. *Chemical Reviews* **2015**, 115(21), 12045–12090.

polarized bonds (ammonium salts, diazonium salts, triazoles, etc) and unactivated or poorly polarized bonds (amines, amides, hydrazines, etc).

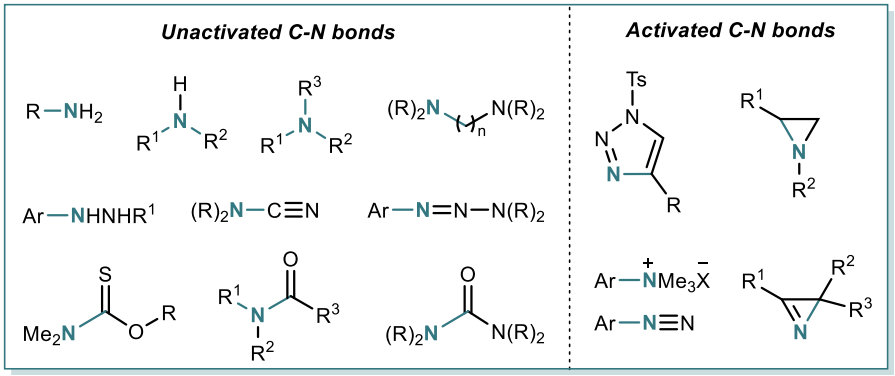

Scheme 3. Examples of simple N-containing compounds divided between unactivated (left) and activated (right) C-N bonds.

The performance of a site selective transformation is much more challenging for unactivated compounds; therefore, specific strategies must be employed to promote the coupling. This is the case of aromatic amines, which are N-containing compounds of particular interest since they are cheap, stable, and easily available; characteristics that set them as an attractive feedstock for the preparation of functionalised molecules. One of the reasons for the challenging cleavage of C-N bonds in aromatic amines is its high dissociation energy. To overcome this problem, when aromatic amines are employed in cross-coupling, the transformation is usually accompanied by a pre-activation, in which the amine is converted into a more reactive compound such as diazonium salts,[16]

16 a) Wu, G. J.; Deng, Y. F.; Wu, C. Q.; Zhang, Y.; Wang, J. B., *Angew. Chem. Int. Ed*., **2014**, 53, 10510–10514; b) Wu, G. J.; Deng, Y. F.; Wu, C. Q.; Wang, X.; Zhang, Y.; Wang, J. B., *Eur. J. Org. Chem.*, **2014**, 21, 4477–4481; c) Ghosh, I.; Marzo, L.; Das, A.; Shaikh, R.; König, B., *Acc. Chem. Res*., **2016**, 49, 1566–1577.

ammonium salts[17,18] or pyridinium salts[19,20] (Scheme 4, a). Although this is the most common pre-activation mode, it has been proved that the conversion of amines to other unactivated compounds that present weaker bonds (such as amides) can also promote the transformation.[21] Another inherent challenge that we face upon the disconnection of C(aryl)-N bonds is the achievement of a site selective transformation. The use of directing groups (DG) is a well-established methodology to deal with selectivity issues; the DG coordinates to the metal holding it into close proximity and driving the reaction towards the cleavage of the inert bond at the *ortho*-position (Scheme 4, b).[22]

---

17 For a comprehensive review see: Wang, Z. X.; Yang, B. *Organic and Biomolecular Chemistry*, **2020**, 18(6), 1057–1072.

18 a) Maity, P.; Shacklady-McAtee, D. M.; Yap, G. P. A.; Sirianni, E. R.; Watson, M. P., *J. Am. Chem. Soc.*, **2013**, 135, 280–285. b) Moragas, T.; Gaydou, M.; Martin, R., *Angew. Chem. Int. Ed*., **2016**, 55, 5053–5057. c) Wang, T.; Yang, S. W.; Xu, S. L.; Han, C. Y.; Guo, G.; Zhao, J. F., *RSC Adv.* **2017**, 7, 15805–15808; d) Liao, L. L.; Cao, G. M.; Ye, J. H.; Sun, G. Q.; Zhou, W. J.; Gui, Y. Y.; Yan, S. S.; Shen, G.; Yu, D. G., *J. Am. Chem. Soc.*, **2018**, 140, 17338–17342.

19 For a comprehensive review see: Li, Y. N.; Xiao, F.; Guo, Y.; Zeng, Y. F. *European Journal of Organic Chemistry*, **2021**, 2021(8), 1215–1228.

20 (a) Ociepa, M.; Turkowska, J.; Gryko, D., *ACS Catal*. **2018**, 8, 11362–11367. (b) Yue, H. F.; Zhu, C.; Shen, L.; Geng, Q. Y.; Hock, K. J.; Yuan, T. T.; Cavallo, L. G.; Rueping, M., *Chem. Sci.* **2019**, 10, 4430–4435. (c) Montero, R. M.; Yatham, V. R.; Yin, H. F.; Davies, J.; Martin, R., *Org. Lett.*, **2019**, 21, 2947–2951. (d) Plunkett, S.; Basch, C. H.; Santana, S. O.; Watson, M. P., *J. Am. Chem. Soc.*, **2019**, 141, 2257–2262.

21 (a) Shi, S.; Meng, G.; Szostak, M., *Angew. Chem. Int. Ed*., **2016**, 55, 6959−6963. (b) Zhang, Z.; Zheng, D.; Wan, Y.; Zhang, G.; Bi, J.; Liu, Q.; Liu, T.; Shi, L., *Journal of Organic Chemistry*, **2018**, 83(3), 1369–1376. (c) Liu, C.; Li, G.; Shi, S.; Meng, G.; Lalancette, R.; Szostak, R.; Szostak, M., *ACS Catal.* **2018**, 8, 9131−9139. (d) Zhang, Z. B.; Ji, C. L.; Yang, C.; Chen, J.; Hong, X.; Xia, J. B. *Org. Lett*., **2019**, 21, 1226−1231.

22 (a) Koreeda, T.; Kochi, T.; Kakiuchi, F. *J. Am. Chem. Soc*. **2009**, 131, 7238. (b) Y. Zhao, V. Snieckus, *J. Am. Chem. Soc.*, **2014**, 136, 11224–11227 (c) H. Kondo, N. Akiba, T. Kochi, F. Kakiuchi, *Angew. Chem. Int. Ed.*, 2015, 54, 9293–9297. (d) X. Cong, F. Fan, P. Ma, M. Luo, H. Chen, X. Zeng, *J. Am. Chem. Soc*., **2017**, 139, 15182–15190 (e) P.

Up to date, limited works have achieved the direct and selective cleavage of C(aryl)-N bonds without the use of any pre-activation or directing groups (Scheme 4, c), and they entail the use of harsh reaction conditions.[23] Besides, the development of reactions with full atom economy it is still in his infancy. A lot of work is still left to be done in such promising field, and the deep understanding of these disconnection strategies will assist the development of new routes for the preparation of synthetically challenging scaffolds as well as the optimization of the existing synthetic routs and the achievement of higher atom economy processes.[24]

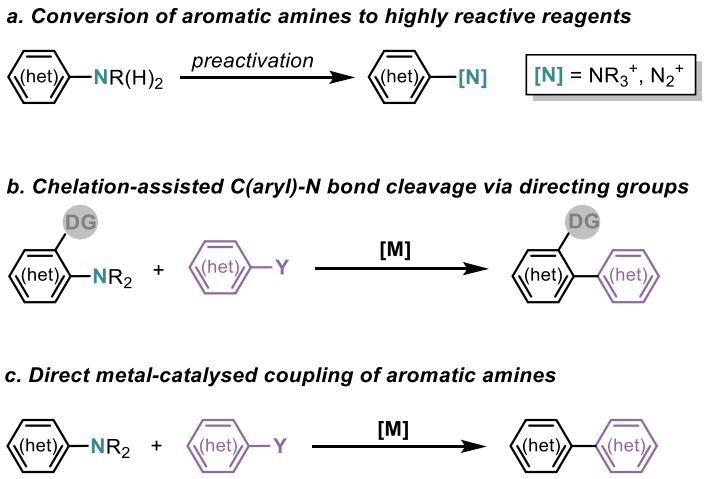

Scheme 4. Current methods for the transition metal catalysed C(aryl)-N bond cleavage.

Nareddy, F. Jordan, M. Szostak, *ACS Catal.*, **2017**, 7, 5721–5745. (f) Q. Zhao, J. Zhang, M. Szostak, *ACS Catal*. **2019**, 9 8171–8177.

23 (a) Cao, Z.-C; Xie, S.-J.; Fang, H.; Shi, Z.-J. *J. Am. Chem. Soc.*, **2018**, 140, 13575–13579. (b) Xu, J.; Zhao, F.; Yuan, Y.; Wu, X. *Org. Lett.* **2020**, 22, 2756−2760.

24 Bahou, K. A.; Bower, J. F.; Garc, J. *ACS Catal.*, **2020**, 10, 21, 12738–12759.

2. Experimental overview

In 2018, Cao *et al.* reported the first direct Suzuki-Miyaura coupling of non-activated dimethyl aryl amines (Scheme 5).[25] This challenging transformation is achieved within 36h at 136ºC and involves slight modifications to the classic Suzuki-Miyaura methodology: (i) proceeds in the absence of base and (ii) reductive conditions (presence of Mg) are required to accomplish a successful transformation. To understand the implications of these distinctive characteristics on the reaction pathway, the authors performed several mechanistic experiments.

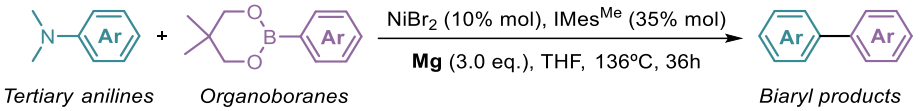

Scheme 5. Ni-catalysed and Mg-facilitated cross-coupling of dimethyl aryl amines with arylboronic esters reported by Cao *et al.*[25]

The exhaustive mechanistic study by Cao *et al.* has been used as basis for the current chapter, where we provide a comprehensive computational study of this Ni-catalysed cross-coupling of dimethyl aryl amines with arylboronic esters. We aim to contribute to the mechanistic understanding of the reaction as well as disclosing the role of magnesium, which remains unclear in the experimental publication. To assist the discussion of the computational results, in this section we introduce here the reader to the most important details of the experimental work.

The reaction conditions were optimized using N,N-dimethyl-2-naphthalene (**1a**) and phenylboronic acid neopentylglycol ester (**2a**) as coupling partners (Table 1). The selected reaction parameters were $NiBr_2$ (10%) as catalyst,

25 Cao, Z. C.; Xie, S. J.; Fang, H.; Shi, Z. J., *J. Am. Chem. Soc.*, **2018**, 140(42), 13575–13579.

$IMes^{Me}$ (35%) as ligand, magnesium (3 equiv.) as reductant and THF as solvent. These parameters, in combination with high temperature and long reaction times (136º and 36h) achieve 84% yield of the desired coupling product **3a** (entry 1). The crucial role of the catalyst, reductant and ligand were confirmed with control experiments (entries 2-4); high drops on conversion yields are observed when any of these species is excluded. Interestingly, the addition of CsF, (a base frequently employed in Suzuki-Miyaura couplings) shuts down the reaction, indicating possible deviations from the standard cross-coupling reaction pathway. The authors also performed a detailed study on the effect of diverse modifications on the carbene backbone and substituents (entries 6-9) which led to high conversion drops, going from 84% (with $IMes^{Me}$) to 0% (with IPr or SIMes). Finally, the alteration of the selected organoboron reagent, and solvent (entries 10-12) also led to a decrease on the reaction yields, however, these results are less relevant for the computational investigation and will not be further discussed.

Table 1. Optimization of reaction conditions in the experimental work by Cao *et al.* [a]

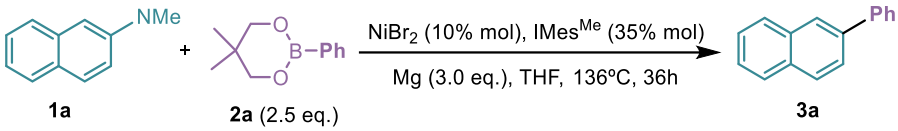

entry	deviation from stand. conditions	**3a** Yield (%)
1	none	84
2	without $NiBr_2$	0
3	without $IMes^{Me}$	0
4	without Mg	<5
5	CsF (2.0 equiv.) was added	0
6	IMes instead of $IMes^{Me}$	14
7	SIMes instead of $IMes^{Me}$	<5
8	IPr instead of $IMes^{Me}$	0
9	SIMes instead of $IMes^{Me}$	0
10	PhBpin instead of 2a	16
11	$(PhBO)_3$ instead of 2a	<5
12	PhMe instead of THF	46

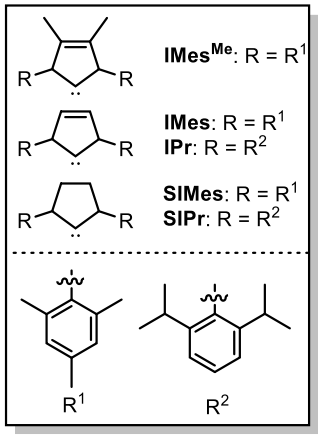

[a] NMR yields reported using CH_2Br_2 as internal standard. Standard conditions.

With the optimal reaction conditions in hand, they investigated the scope; herein we present a small selection of the main experimental results (Scheme 6). First of all, the authors modified the substrates by arylation with different alkyl substituents (products 4 and 5), as well as with a collection of functional groups (products 6 and 7). All these modifications led, to the desired coupling product in good yields. Then, the reactivity of other N,N-dimethyl amines was investigated, achieving moderate yields for most of the couplings (products 9-11), except when the *ortho*-position was substituted (product 8), where only traces were obtained. Finally, different arylboronates were studied and proved to be suitable nucleophiles, both with aryl and alkyl substituents (products 12-

15). As well as with the N,N-dimethyl amines, the *ortho*-substitution led to failure of the coupling. The inhibition by *ortho* substitution is likely due to steric hindrance.

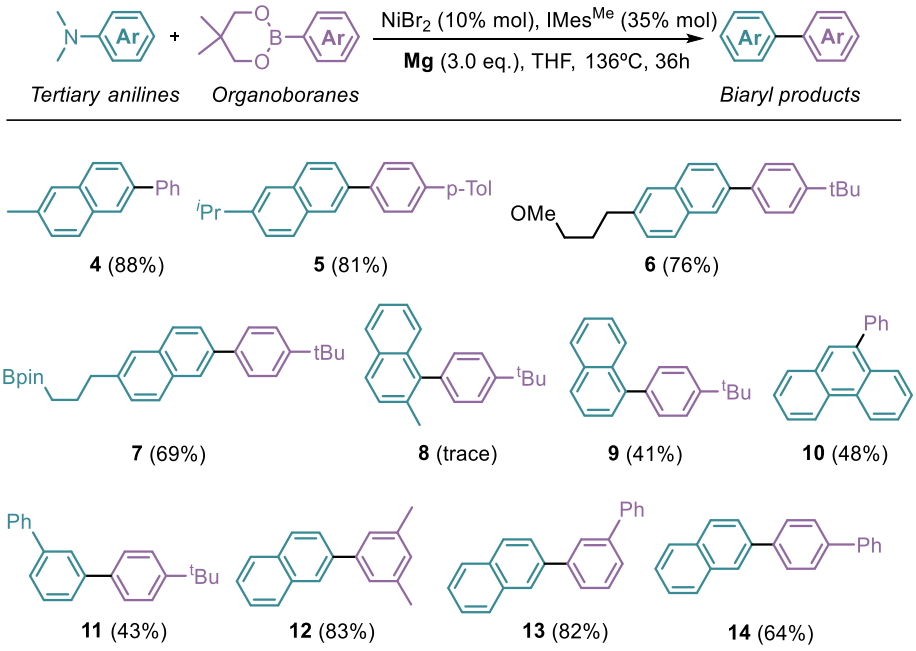

Scheme 6. Selected examples of the substrate scope of the Suzuky-Miyaura coupling reported by Cao *et al.*

After evaluating the substrate scope, the authors investigated the effect of the modification of the reductant (Table 2) and observed the unique role of magnesium: when the metal was substituted by other reductants, the desired product was not observed (entries 2-7). If magnesium were participating only in the reduction of the nickel salt, it should be possible to replace it by another metal with higher reduction potential (such as sodium, entry 2). This counterintuitive result points to a non-innocent role of magnesium in the reaction mechanism.

Table 2. Examination of different metals or reductants in the experimental work by Cao *et al.* [a]

Entry	Metals or reductants	Loading (equiv.)	SRP	3a yield (%)
1	Mg	3.0	-2.37	84
2	Na	6.0	-2.71	0
3	Mn	3.0	-1.19	0
4	Zn	3.0	-0.76	0
5	Al	3.0	-1.66	0
6	Sn	3.0	-0.14	0
7	Cp_2Co	6.0	-1.33	0

Intrigued by the seemingly special role played by magnesium, the authors conducted several additional mechanistic studies. They started searching the identity of the active species. Since both Ni^0/Ni^{II} and Ni^I/Ni^{III} catalytic cycles are plausible, three potential active species; $Ni(IMes^{Me})_2$, $Ni(IMes^{Me})_2Br$, $Ni(IMes^{Me})_2Br_2$, were synthetized and tested as catalysts (Table 3). Once more, no product **3a** was observed in absence of magnesium (entries 3-5). Conversely, variations on yields were obtained depending on the active species employed: while the yield for both $Ni(IMes^{Me})_2Br$ and $Ni(IMes^{Me})_2Br_2$ was greater than 80%, when $Ni(IMes^{Me})_2$ was used the conversion suffered a considerable drop to 53% (entries 6-8). Cao *et. al.* propose two possible explanations aligned with the previous observations: (i) the $MgBr_2$ generated in situ might act as a promoter for the coupling and (ii) the transformation could occur through a Ni(I)/Ni(III) catalytic cycle instead of the classic Ni(0)/Ni(II) pathway. Both options were further explored by the authors by means of mechanistic experiments.

Table 3. Experiments for a mechanistic study.[a]

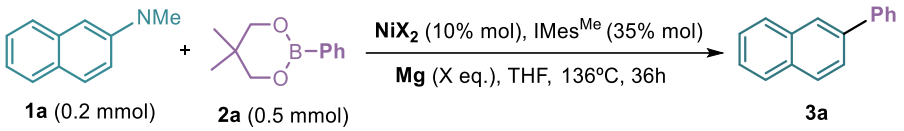

1a (0.2 mmol) **2a** (0.5 mmol) **3a**

entry	Ni source employed	Mg loading (equiv.)	**3a** yield (%)
1	$NiBr_2$	3.0	84
2	$NiBr_2$	--	<5
3[a]	$Ni(IMes^{Me})_2$	--	<5
4[a]	$Ni(IMes^{Me})_2Br$	--	<5
5[a]	$Ni(IMes^{Me})_2Br_2$	--	<5
6[a]	$Ni(IMes^{Me})_2$	3.0	53
7[a]	$Ni(IMes^{Me})_2Br$	3.0	86
8[a]	$Ni(IMes^{Me})_2Br_2$	3.0	83

[a] when X =$IMes^{Me}$ the amount of $IMes^{Me}$ employed is reduced to 15%. NMR yield

$MgBr_2$ and other Lewis acids had been previously used to promote the efficiency of cross-coupling transformations, achieving a lower energy pathway by facilitating oxidative addition, transmetalation or reductive elimination steps.[26] To explore the effect in their system, Cao *et. al.* used catalytic amounts of $MgBr_2$ as additive. Remarkably, the addition of the salt leads to a dramatic decrease on the reaction yield indicating the inefficiency of the salt as facilitator for the coupling (Table 4). In view of this, the possibility of a Ni(I)/Ni(III) catalytic cycle was explored. To this end, electro paramagnetic resonance (EPR) measurements were conducted for the $NiBr_2$ reduction process as well as in the reaction mixture, and signals of unpaired

26 (a) Duez, S.; Steib, A. K.; Manolikakes, S. M.; Knochel, P., *Angew. Chem. Int. Ed.* **2011**, 50, 7686 –7690 (b) Yang, Z.-K.; Wang, C.; Uchiyama, M., *Synlett*, **2017**, 28, 2565–2568 (c) Erdelmeier, I.; Bülow, G.; Woo, C.-W.; Decker, J.; Raabe, G.; Gais, H.-J., *Chem. Eur. J.* **2019**, 25, 8371-8386.

electrons were observed in both cases. These signals strongly support the presence of Ni(I) species in the sample.

Table 4. Experiments for the mechanistic study[a]

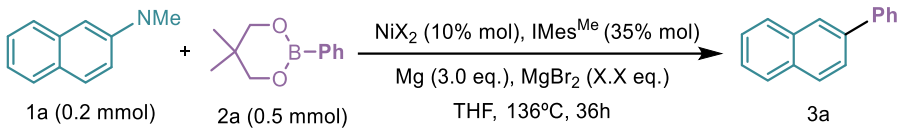

entry	Ni source employed	$MgBr_2$ loading (equiv.)	**3a** yield (%)
1	$NiBr_2$	--	84
2	$NiBr_2$	1.0	<10
3[a]	$Ni(IMes^{Me})_2$	--	53
4[a]	$Ni(IMes^{Me})_2$	0.1	<5

[a] when Ni(IMesMe)2 is employed, the amount$IMes^{Me}$ in the media is reduced to 15%.

With all these experimental information in hand, the authors proposed a magnesium facilitated Ni(I)/Ni(III) catalytic cycle (Scheme 7). First the $NiBr_2$ salt is reduced to achieve the active specie $Ni(IMes^{Me})_2Br$. Then, the reaction evolves akin to a common Suzuky-Miyaura coupling, going through oxidative addition, transmetalation and finally the reductive elimination which releases the biaryl product recovering the active species. The magnesium would act as a facilitator for one or more of these processes, yet the authors could not identify in which step(s) the reductant was participating.

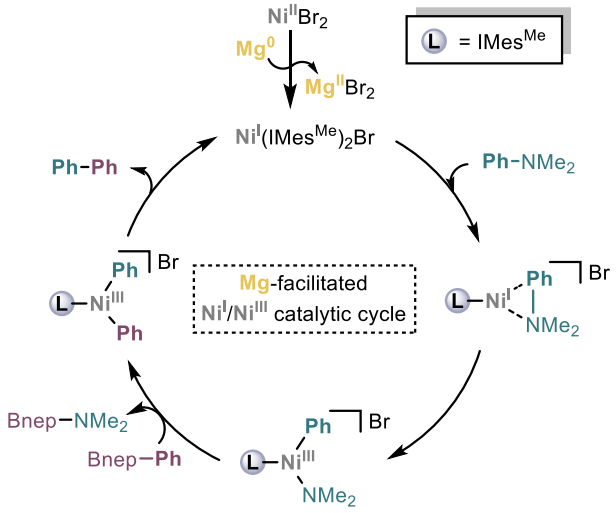

Scheme 7. Catalytic cycle for the Ni-catalysed and Mg-facilitated cross-coupling of dimethyl aryl amines with arylboronic esters proposed by Cao *et al.*

3. Objectives

The field of cross-coupling reactions has experienced an enormous advancement during the last decades. Nowadays, one of the central challenges of the field involves the development of disconnection strategies to enable cross-coupling transformations with highly inert substrates. While there have appeared several interesting works on the topic, there lacks a general approach to achieve these challenging cleavage procedures. Naturally, to extend the usage of these cutting-edge strategies it is crucial to understand its underlaying mechanisms, an effort that is hindered by the intrinsic complexity of the reaction pathways.

This is the case of the pioneering investigation by Cao *et al.* on the cleavage of N-(aryl) bonds in absence of activation and directional groups; their work followed a Suzuki-Miyaura template with the introduction of magnesium as reductant. The strategy has not been applied to other reactions, in part due to

the poor understanding of the mechanism. In particular, the lack of understanding of the obscure and unique role of magnesium, appears as a significant obstacle.

Herein, we aim to revel the reaction mechanism, for this Ni-catalysed and Mg-facilitated cross-coupling of dimethyl aryl amines with arylboronic esters. We will pay specific attention to the role of magnesium and to the individual properties that makes this metal a great fit for this transformation.

4. Computational details

The results and discussion section of this chapter has been divided in two main sections: mechanistic investigation and unique properties of Mg. Each section has been studied at its own level of theory; therefore the computational details will be specified separately.

In the mechanistic investigation section, all calculations were carried out using Gaussian09 (Rev. D.01)[27] package at the B3LYP[28] level of theory, including

27 Gaussian 09, Revision D.01, M. J. Frisch, G. W. Trucks, H. B. Schlegel, G. E. Scuseria, M. A. Robb, J. R. Cheeseman, G. Scalmani, V. Barone, G. A. Petersson, H. Nakatsuji, X. Li, M. Caricato, A. Marenich, J. Bloino, B. G. Janesko, R. Gomperts, B. Mennucci, H. P. Hratchian, J. V. Ortiz, A. F. Izmaylov, J. L. Sonnenberg, D. Williams-Young, F. Ding, F. Lipparini, F. Egidi, J. Goings, B. Peng, A. Petrone, T. Henderson, D. Ranasinghe, V. G. Zakrzewski, J. Gao, N. Rega, G. Zheng, W. Liang, M. Hada, M. Ehara, K. Toyota, R. Fukuda, J. Hasegawa, M. Ishida, T. Nakajima, Y. Honda, O. Kitao, H. Nakai, T. Vreven, K. Throssell, J. A. Montgomery, Jr., J. E. Peralta, F. Ogliaro, M. Bearpark, J. J. Heyd, E. Brothers, K. N. Kudin, V. N. Staroverov, T. Keith, R. Kobayashi, J. Normand, K. Raghavachari, A. Rendell, J. C. Burant, S. S. Iyengar, J. Tomasi, M. Cossi, J. M. Millam, M. Klene, C. Adamo, R. Cammi, J. W. Ochterski, R. L. Martin, K. Morokuma, O. Farkas, J. B. Foresman, and D. J. Fox, Gaussian, Inc., Wallingford CT, 2016.

28 A. D. Becke, J. Chem. Phys. 1993, 98, 5648–5652.

Grimme empirical dispersion.[29] The standard 6-31G(d)[30] basis set was employed for all C, H, N, B, Br and Mg atoms and the LANL2DZ[31] basis set, along with its associated ECP was employed for Ni. To minimize the basis set superposition error (BSSE), the potential energies were further refined with 6-311+G(d,p)[32] single-point calculations for all atoms, except for Ni, in which LANL2TZ[33] and its associated ECP was employed.

A relaxed cluster model was introduced to represent solid magnesium. The cluster was frozen along the mechanism, optimizing only the organometallic part. This implies the appearance of small imaginary frequencies in most of the intermediates, thus a cut off at 100 was applied in frequency calculations. Further details on the magnesium cluster are discussed on the results and discussion.

The unique properties of Mg section was carried out during the short stay in the group of Prof. Clémence Corminboeuf. As this was a posterior work, we used the newest Gaussian16 (Rev. D.01)[34] package. The functional was

29 S. Grimme, J. Antony, S. Ehrlich, H. Krieg, J. Chem. Phys. 2010, 132 (15), 154104-19.

30 (a) W. J. Hehre, R. Ditchfield, J. A. Pople, J. Chem. Phys. 1972, 56 (11), 2255-2257. (b) P. C. Hariharan, J.A. Pople, Theor. Chim. Acta 1973, 28, 213-222. (c) M. M. Francl, W. J. Pietro, W. J. Hehre, J. S. Binkley, M. S. Gordon, D. J. DeFrees, J. A. Pople, J. Chem. Phys. 1982, 77(7), 3654-3665.

31 P. J. Hay, W.R. Wadt, J. Chem. Phys. 1985, 82, 270-283.

32 a) R. Krishnan, J. S. Binkley, R. Seeger, J. A. Pople, J. Chem. Phys. 1980, 72, 650-654. b) A. D. McLean, G. S. Chandler, J. Chem. Phys. 1980, 72, 5639-5648.

33 L.E. Roy, P.J. Hay, R.L. Martin, J. Chem. Theory Comput. 2008, 4, 1029-1031.

34 Gaussian 16, Revision D.01, M. J. Frisch, G. W. Trucks, H. B. Schlegel, G. E. Scuseria, M. A. Robb, J. R. Cheeseman, G. Scalmani, V. Barone, G. A. Petersson, H. Nakatsuji, X. Li, M. Caricato, A. Marenich, J. Bloino, B. G. Janesko, R. Gomperts, B. Mennucci, H. P. Hratchian, J. V. Ortiz, A. F. Izmaylov, J. L. Sonnenberg, D. Williams-Young, F. Ding, F. Lipparini, F. Egidi, J. Goings, B. Peng, A. Petrone, T. Henderson, D. Ranasinghe, V. G. Zakrzewski, J. Gao, N. Rega, G. Zheng, W. Liang, M. Hada, M. Ehara, K. Toyota, R. Fukuda, J. Hasegawa, M. Ishida, T. Nakajima, Y. Honda, O. Kitao, H. Nakai, T. Vreven,

maintained (B3LYP including Grimme empirical dispersion), as well as the 6-31G(d) basis set for all C, H, N, B, Br atoms and the LANL2DZ basis set, along with its associated ECP was employed for Ni. The base was modified on the calculation of the different metallic clusters since the standard 6-31G(d) Pople basis set was not available for all the metals included in the study. The LANL2DZ basis set, along with its associated ECP was employed for Li, Be, Na, Mg, K, Ca, Rb, Sr, Cs, Ba, Pd, Pt, Cu, Ag, Hg, Zn, Al, Si, Sn, W and Pb. It is noteworthy that, as in the previous section, the relaxed cluster model was introduced for all the metals and was frozen along the mechanism, optimizing only the organometallic part and a cut off of 100 was implemented to remove the small imaginary frequencies arising from the frozen cluster. The solvent was also implemented implicitly trough an SMD methodology and tetrahydrofuran was selected as solvent (ε =7.4257).

For all optimizations (in both sections), vibrational frequency calculations were computed to establish the nature of all stationary points (zero imaginary frequencies for minima and one for transition states). Solvation was implemented implicitly through an SMD[35] methodology and tetrahydrofuran was selected as solvent (ε =7.4257). All the reported energies are free energies in solution calculated at 298 K and 1 atm in kcal/mol. A data set collection of all computational data is available in the ioChem-BD repository.

K. Throssell, J. A. Montgomery, Jr., J. E. Peralta, F. Ogliaro, M. Bearpark, J. J. Heyd, E. Brothers, K. N. Kudin, V. N. Staroverov, T. Keith, R. Kobayashi, J. Normand, K. Raghavachari, A. Rendell, J. C. Burant, S. S. Iyengar, J. Tomasi, M. Cossi, J. M. Millam, M. Klene, C. Adamo, R. Cammi, J. W. Ochterski, R. L. Martin, K. Morokuma, O. Farkas, J. B. Foresman, and D. J. Fox, Gaussian, Inc., Wallingford CT, 2016.

35 A. V. Marenich, C. J. Cramer, D. G. Truhlar, J. Phys. Chem. B, 113, no. 18, pp. 6378–6396, 2009.

5. Results and discussion

Mechanistic investigation

As mentioned in the computational details, this study has been done using a simplified model of the reaction reported by Cao *et al.* In our model, both aryl groups are phenyl (Scheme 8).

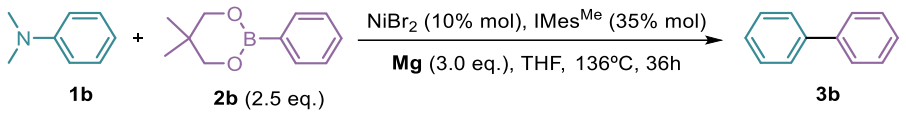

Scheme 8. Simplified model for the Ni-catalysed and Mg-facilitated cross-coupling of dimethyl aryl amines with arylboronic esters reported by Cao *et al.* used in the computational study.

Reduction of the $NiBr_2$ precursor

The first step of this transformation involves the reaction of solid magnesium with the nickel (II) salt. This reduces the nickel center (either by one or two units), leading to the corresponding Ni^0 or Ni^I active species (Scheme 9). The involvement of a solid metal in the process requires the application of a thermodynamic cycle to estimate its energy from DFT calculations.[36] This methodology allows the theoretical calculation of standard reduction potential (SRP), necessary for the estimation of the thermodynamic parameters of this reduction steps (see *Theoretical Background*).

Both Ni^0 and Ni^I species are formed in an exothermic manner. The process involves free energy changes of -4.7 and -14.0 kcal/mol, respectively. This result showcases the reductive power of magnesium, sufficient to achieve both potentially active species (**I1** and **I1bis**). The one electron reduction is favored

36 Funes-Ardoiz, I.; Maseras, F., *ChemPhysChem*, **2019**, 20(1), 159–162.

by 9.3 kcal/mol, but the eventual role of Ni^{I} in the cycle will depend on its ulterior activity.

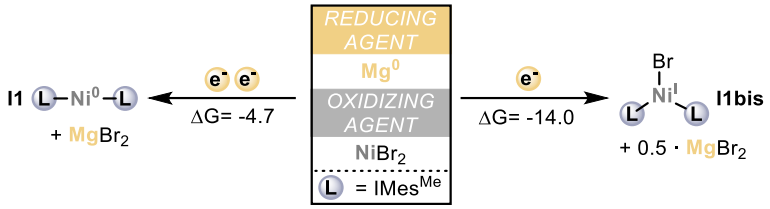

Scheme 9. Redox reaction between the magnesium and the nickel salt to form the potential active species **I1** and **I1x**.

Mechanism in the absence of magnesium

Ni(0)-Ni(II) vs. Ni(I)-Ni(III) oxidative addition

As explained in the experimental overview section, the results obtained by Cao *et al.* in the mechanistic investigations suggest that the coupling reaction follows a Ni^{I}/Ni^{III} pathway. This conclusion seems counterintuitive as the inert nature of the C–N bonds makes their cleavage a challenging transformation. Thus, the oxidative addition would presumably be the rate determining step of the transformation in which case, a Ni^{0}/Ni^{II} catalytic cycle, would facilitate the process in comparison to the analogous Ni^{I}/Ni^{III} pathway, due to the higher presence of electron density in a Ni^{0} centre. With these ideas in mind and considering that both Ni^{0} and Ni^{I} species could be present in the reaction media, we decided to investigate the oxidative addition step for both Ni^{0}/Ni^{II} and Ni^{I}/Ni^{III} catalytic cycles (Scheme 10).

The high bulkiness of the $IMes^{Me}$ ligands blocks the approach of the amine to the nickel complex. Thus, the reaction starts with the decoordination of one ligand, followed by the coordination of the amine and the subsequent oxidative addition. The Ni^{0}/Ni^{II} catalytic cycle (Scheme 10, left), involves a highly endergonic ligand exchange which yields a substitution intermediate (**$I3_x$**) lying 25.4 kcal/mol above reactants. **$I3_x$** evolves towards the addition, with a barrier of 10.4 kcal/mol (**$TS_{I3x-I4x}$**). Despite the barrier being relatively low, the high

energy precursor makes the oxidative addition process kinetically prohibitive, with an overall barrier of 35.8 kcal/mol. **$TS_{I3x-I4x}$** yields the oxidative addition product, **$I4_x$** found at 14.4 kcal/mol.

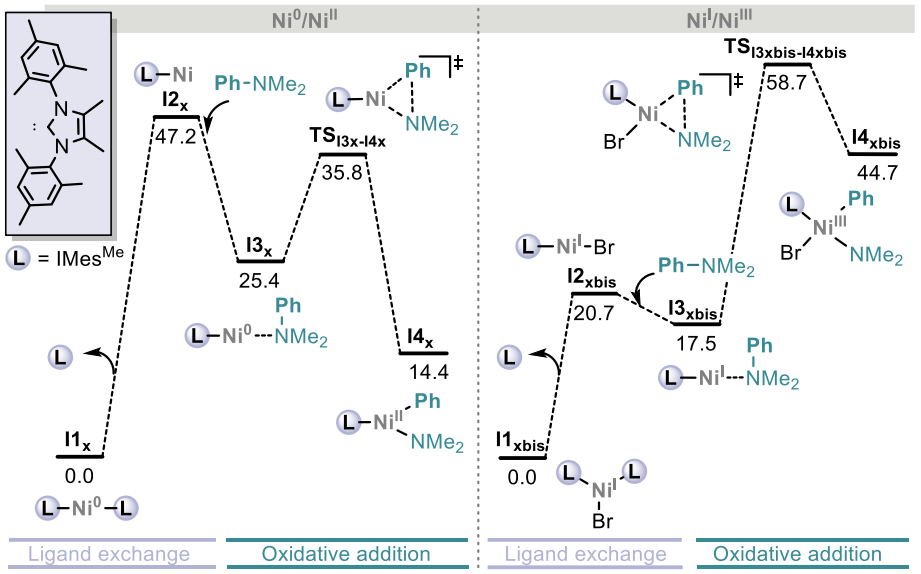

Scheme 10. Ligand exchange and oxidative addition steps for the Ni^0/Ni^{II} (left) and the Ni^I/Ni^{III} (right) catalytic cycles.

The alternative Ni^I/Ni^{III} catalytic cycle (Scheme 10, right), involves a lower energy ligand exchange which leads to the substituted product, **$I3_{xbis}$** found at 17.5 kcal/mol. This is, 8 kcal/mol below the analogous Ni^{II} intermediate (**$I3_x$**). Still, the oxidative addition step is completely prohibitive, with **$TS_{I3xbis-I4xbis}$** found at 41.2 kcal/mol above **$I3_{xbis}$** and yields a high energy oxidative addition product, **$I4_{xbis}$** laying at 44.7 kcal/mol above reactants. The highly unstable intermediate **$I4_{xbis}$** points that a Ni^{III} specie will not be accessible.

These findings confirmed our suspicion: the cleavage of the C(aryl)-N bond cannot be achieved through a Ni^I/Ni^{III} pathway. Thus, we propose the presence of a Ni^0/Ni^{II} catalytic cycle, in which the oxidative addition is promoted by the

presence of magnesium. With this hypothesis in mind, we investigated the full mechanism for the Ni^0/Ni^{II} catalytic cycle in the absence of magnesium.

Complete mechanism in the absence of magnesium

The general picture of the mechanism in the absence of magnesium is shown in Scheme 11. The reaction begins as described in the previous section: first, one of the $IMes^{Me}$ ligands is exchanged by an amine reagent yielding intermediate **$I3_x$**, found at 25.6 kcal/mol. Then, the oxidative addition takes place, through the kinetically prohibitive (35.8 kcal/mol) transition state, **$TS_{I3x-I4x}$** which yields the Ni^{II} specie **$I4_x$** found 14.4 kcal/mol above reactants. As mentioned above, we assume here that this step will be facilitated by magnesium.

From **$I4_x$** the reaction proceeds with the organoboron activation, a process which is commonly accomplished through the presence of a base in the reaction media. However, as introduced in the experimental overview, the base is not required in this transformation. Indeed, the reaction is driven by the presence of the amine which substitutes the role of base in the reaction media. The amine reacts with the boron, through a barrier of 29.0 kcal/mol (**$TS_{I4x-I5x}$**) yielding the B-quaternized species **$I5_x$**, that can then proceed with the transmetalation.

From intermediate **$I5_x$**, the transmetalation takes place through a four membered ring transition state (**$TS_{I5x-I6x}$**). The highly strained conformation together with the steric hindrance provided by the ligand induces a high energy event (37.3 kcal/mol). Once more, we face a kinetically prohibitive step, which should be promoted by the reductant.

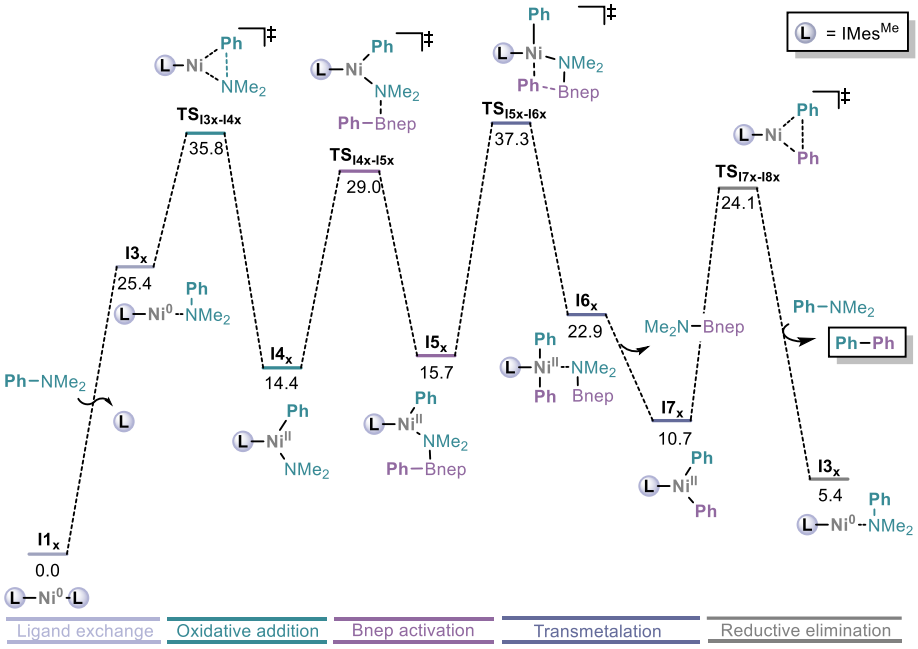

Scheme 11. Mechanism for the cross-coupling of dimethyl aryl amines with aryl boronic esters under reductive conditions, without the presence of magnesium as facilitator.

The transmetalation product, **I6$_x$**, releases the boronamine in a thermodynamically favorable step of 12.2 kcal/mol, yielding **I7$_x$**, which is prone to perform the reductive elimination. Surprisingly, the reductive elimination transition state (**TS$_{I7x-I8x}$**) features the lowest energy barrier of the mechanism (24.1 kcal/mol), highlighting that it is not necessary to access a Ni^{III} specie to enable the reductive elimination. Finally, the cross-coupling product is released, and another amine moiety is coordinated, recovering the **I3$_x$** intermediate which can restart the catalytic cycle.

It is noteworthy that the overall reaction is endergonic by 5.4 kcal/mol, this is because the decoordination of the ligand is highly disfavored. Thus, from intermediate **I8x**, the amine and the ligand will compete for the replacement of

the product and since the ligand presents an stronger coordination to the metal center, it will hamper the restart of the catalytic cycle.

Magnesium as facilitator

The presence of magnesium has been omitted in the previous section to obtain a preliminary idea of the reaction mechanism. Still, the experimental studies demonstrated that the metal was acting as a promoter for the transformation, boasting a dual role; the reduction of the nickel salt and the assistance of one or more reaction steps. Moreover, this fact was verified due to the high activation barriers found in out calculations for the mechanism in absence of magnesium. In the current section we explored the mechanism were the magnesium acts as facilitator. We must recall that the participation of $MgBr_2$ was already discarded in the experimental work. Thus, we envisaged that Mg^0 could be the promoter of the reaction. The introduction of Mg^0 in the calculation is not trivial; the proper reproduction of a solid by computational means would imply the use of heterogeneous catalysis methods (plane waves). However, the dimensions of our system *i.e.* the huge organic ligand, would require enormous computation times, hence, precluding the practical application of this methodology.

Cluster of magnesium atoms

At this stage, we were inspired by the work of Panteleev *et al.*[37] where magnesium clusters were used to reproduce the activation energies in a Grignard reaction. The authors claim that in systems with small nuclearity the metal lattice parameters used for the surface models have completely different structures. Thus, the utilization of a relaxed cluster concept appears to be appropriate to determine the thermodynamic parameters of this type of systems.

37 Panteleev, S. V.; Belyaev, S. N.; Ignatov, S. K. *J. Theor. Comput. Chem.*, **2018**, 17(7), 1850044.

We consider that their reasoning can be extended to the current system since the use of powder magnesium implies the presence of small nuclearity clusters, and thus, the magnesium metal crystal lattice will be highly diverse.

The application of relaxed cluster models with small nuclearity implies an ineluctable dependence on the cluster size. In their work, Panteleev *et al.* show the alteration of Grignard activation energies with variances in the cluster sizes. This complicates the selection of the appropriate cluster dimension as it will directly influence the cluster properties. In particular, the authors analyze the influence of Mg_n (n=2-20) clusters in two different mechanisms in the Grignard reaction (radical and molecular). Smaller clusters (n < 10) facilitate the radical mechanism while bigger clusters (n > 18) favor the molecular process. The Mg_{10} cluster is approximately settled in the transition between mechanisms. Besides, clusters of 10 atoms are in the limit of those clusters considered as models of active surface defects, which will likely be present in powder magnesium. This together with the acquisition of a plateau in the desorption energy around a nuclearity of 10 brought us to select a Mg_{10} cluster as model to describe our surface (Figure 1).

Figure 1. 3D structure of the optimized Mg_{10} metal cluster**.**

The structure for the selected magnesium cluster was extracted from Panteleev *et al.* article and optimized at our level of theory (B3LYP-D3/6-31+G*). The resulting cluster structure was used along the mechanism maintaining the

magnesium atoms freeze and optimizing the organometallic system. This strategy has been implemented to avoid unrealistic relaxations arising from the complex homogeneous mechanism e.g. leaking of Mg atoms from the surface. We are aware that the use of a freeze cluster as model will have an impact on the thermodynamic parameters of our calculations, nevertheless, we believe it is the best approximation of the real system that can be done with the current methods. In addition, the potential error arising on the optimization of the magnesium cluster will be systematic along the mechanism, allowing us to eliminate part of the introduced error. We are aware that the use of this methodology implies lower accuracy in comparison to common DFT calculations, still we believe it is sufficient to understand the mechanistic picture.

Mechanism with magnesium

Once we had defined the computational model we proceeded with the calculation of the Mg-facilitated mechanism. For the sake of comparison, we have included the mechanism in absence of magnesium in grey to all the schemes in this section. This is to facilitate the understanding to the reader, presenting a more general picture of the overall scenario.

The first steps of the computed mechanism are depicted in Scheme 12. Similarly to what happened in the mechanism in absence of magnesium, the reaction starts from the active species $Ni(IMes^{Me})_2$. First, Mg^0 displaces one of the $IMes^{Me}$ ligands forming the nearly isoenergetic intermediate **I2**, lying at -0.3 kcal/mol. Then, the amine moiety is coordinated to the metal centre leading to the precursor of the oxidative addition, **I3**, found at 15.0 kcal/mol. This represents a stabilization of 10.4 kcal/mol in comparison with the equivalent intermediate in the mechanism in absence of magnesium (**I3x**). Intermediate **I3** evolves towards the oxidative addition ($\mathbf{TS_{I3\text{-}I4}}$), through a high energy point of 30.8 kcal/mol above reactants, which is high but feasible under the reaction conditions (36h at 136ºC). At this stage of the mechanism, we observe the first

effect of the magnesium in the reaction path; it enables the challenging C-N bond cleavage thanks to a decrease of 5.3 kcal/mol in the barrier. The main contribution of the presence of magnesium to this step seems to be the facilitation of the departure of the $IMes^{Me}$ ligand.

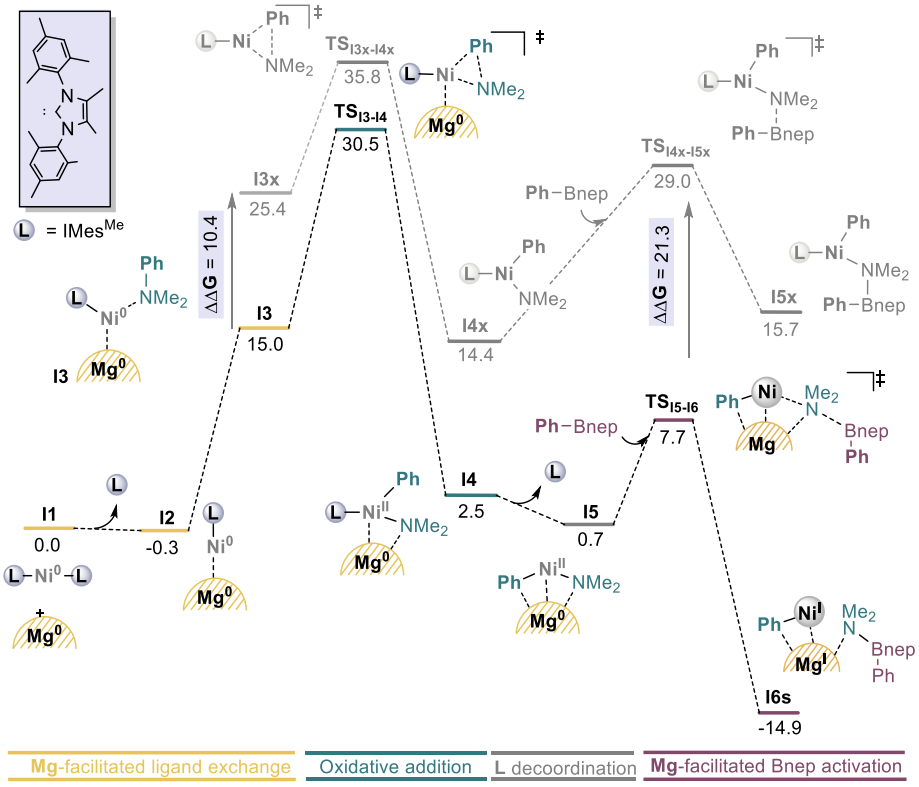

Scheme 12. Gibbs free energy profile for the Mg-facilitated ligand exchange and oxidative addition steps. Mechanism in absence of magnesium in grey. Energies in kcal/mol.

The oxidative addition yields **I4**, found at 2.5 kcal/mol relative to the initial reactants. Once again, the magnesium procures a lower energy pathway, the analogous intermediate **I4x**, lied 14.4 kcal/mol above reactants. At this point, the organoboron reagent should enter to the system. However, the highly hindered environment of the nickel blocks its approximation. Instead, the

second $IMes^{Me}$ ligand is released in an exergonic step of -1.8 kcal/mol leading to the formation of intermediate **I5**. This step was prohibitively high in the mechanism without magnesium because it implies the formation of a high energy di-coordinated species.

The decoordination of the second ligand provides a significantly decreased steric hindrance on the nickel center which enables the approximation of the arylboronic ester. Then, the amine activates the organoboron reagent by quaternizing it through a low barrier process of 7.0 kcal/mol (**TS_{I5-I6}**) and evolves towards the highly stable intermediate **I6s**, found -14.6 kcal/mol. This process takes place on the open shell singlet surface and implies the decoordination of the amine from the Ni centre with the simultaneous formation of a σ-bond between Ni and Mg centers (Figure 2. Division of the system and analysis of the electron distribution between magnesium and nickel.). The later takes the role of co-catalyst, allowing the reaction to proceed through a Ni^{I}-Mg^{I} intermediate.

	e⁻ distribution A Ni^0 - Mg^{II}	***e⁻ distribution B*** Ni^{I} - Mg^{I}
Ni region C/M	0 / 1	-1 / 2
Mg region C/M	0 / 1	+1 / 2
Free energy	Free energy	Free energy

* **C/M** stands for: **Charge** / **Multiplicity**

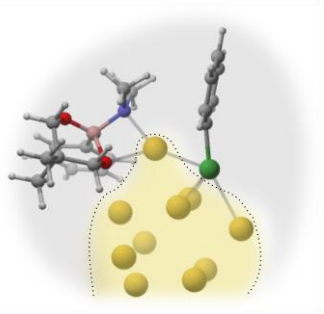

Figure 2. Division of the system and analysis of the electron distribution between magnesium and nickel.

The transfer of one electron from the magnesium moiety has been confirmed through the analysis of the electron distribution of the system. To this end, the intermediate has been divided in two fragments: one including the magnesium cluster (orange part in Figure 2) and the other with the nickel together with the

organic part (grey part in Figure 2). As shown in the table of Figure, each fragment has been computed in two electron distributions. On one side, the electron distribution **A**, with a charge of 0 and multiplicity of 1 for both fragments, corresponding to the Ni^{II}-Mg^{0} specie. On the other side, the electron distribution **B**, which presents a multiplicity of 2 for both fragments and charges of -1 and +1 for Ni and Mg fragments, respectively. The energy difference between these two electron distributions sets the Ni^{I}-Mg^{I} system 36.0 kcal/mol more stable than the analogous Ni^{II}-Mg^{0}, supporting the presence of a single electron transfer (SET) event. This modification of the reaction mechanism demonstrates the presence of a bimetallic pathway where the Mg acts as co-catalyst and decreases the organoboron activation (**TS_{I5-I6}**) by 21.3 kcal/mol.

From the highly stable **I6s** intermediate the system evolves towards the transmetalation, but first this species must undergo an endergonic spin crossing to reach the triplet state intermediate **I6t** (Scheme 13). This switch of the spin state, with a cost of 13.2 kcal/mol, is assumed to occur through a barrierless process since there are minimal changes in the 3D structure of the species, thus no MECP was calculated for the transition.

Once the system has evolved to the triplet state surface, the transmetalation proceeds through a transition state of 31.1 kcal/mol (**$TS_{I6t-I7t}$**). This has an energy 16.2 kcal/mol above reactants, but 31.1 kcal/mol above the previous lowest energy point, **I6s**. In **$TS_{I6t-I7t}$**, the boronamine side product is released. Interestingly, this step entails the direct participation of the reductant as the organoboron phenyl group is transferred to one magnesium atom instead of the nickel center. The transformation yields the transmetalation product **I7t**, laying at 1.9 kcal/mol, which presents one phenyl on the nickel center and another in the magnesium center. Thus, maintaining the Ni^{I}-Mg^{I} electron distribution of the overall system.

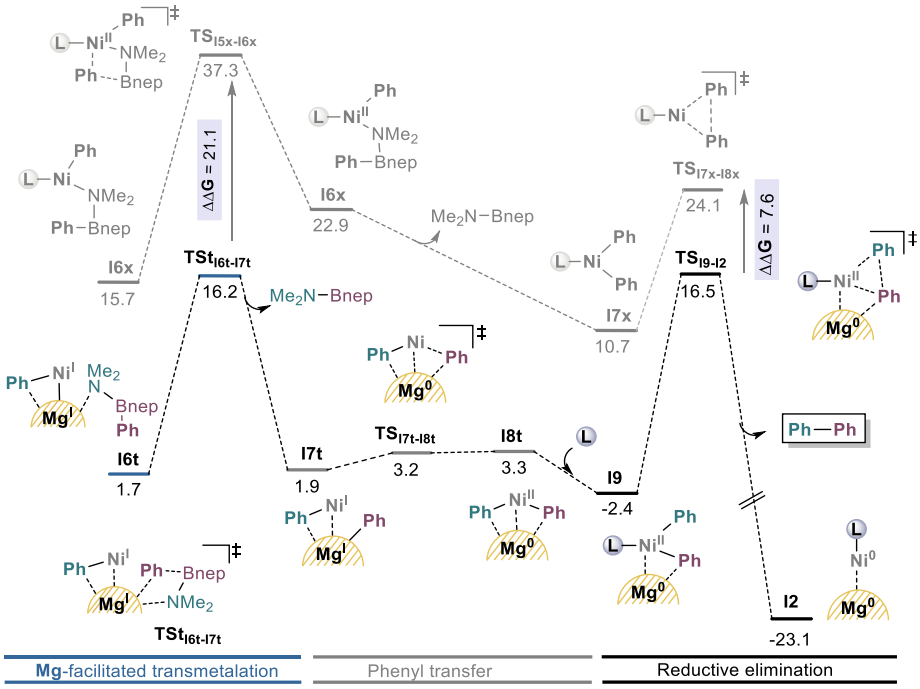

Scheme 13. Gibbs free energy profile for the Mg-facilitated transmetalation, phenyl transfer and reductive elimination steps. Mechanism in absence of magnesium in grey. Energies in kcal/mol.

It is worthwhile to compare here the mechanism without magnesium, where the transmetalation is a completely prohibitive process with an activation energy of 37.3 kcal/mol (**TS$_{I6x-I7x}$**). Thus, magnesium decreases the overall barrier by 6.2 kcal/mol, making the process kinetically affordable. This is attributed to the ability of magnesium to provide access to a transmetalation process on the triplet state surface within a Ni^{I}-Mg^{I} electronic distribution.

In the following step, the phenyl group on the magnesium cluster is transferred to the nickel center and the Ni^{II}-Mg^{0} electron distribution is recovered. The process takes place through a quasi-barrierless transition state (**TS$_{I7t-I8t}$**) of 1.3 kcal/mol which yields intermediate **I8t**, that as mentioned above, has both aryl groups in the nickel centre. Despite the recovery of a Ni^{II}-Mg^{0} electron

distribution, the two phenyl groups are disposed far in the space, hampering the reductive elimination. Thus, at this point, the $IMes^{Me}$ ligand is re-coordinated to the metal centre in an exergonic reaction of -4.9 kcal/mol, yielding **I9**, which has the proper conformation to proceed with the reductive elimination. From this point, the reductive elimination proceeds through $\mathbf{TS_{I9\text{-}I2}}$, with an overall barrier of 31.4 kcal/mol, releasing the product in an irreversible manner and recovering the active species **I2**.

It is noteworthy that the reductive elimination presents a higher activation energy compared to the mechanism without magnesium. This is, in part, due to the presence of the **I6s** intermediate which implies a well in the PES. However, if we compare the reductive eliminations from the precursors; **I9** for the mechanism with magnesium and **I7x** for the one without magnesium we also observe a higher barrier in the presence of magnesium. This is attributed to the coordination nature of the nickel centre on the reductive elimination processes. While **I7x** presents a tricoordinated nickel centre, in **I9** the nickel has a tetracoordinated nature. The different coordination modes imply substantial differences on the key orbital interactions for the reductive elimination process (Figure).

Hitherto we have disclosed the full mechanistic picture of the Ni-catalysed and Mg-facilitated cross-coupling of dimethyl aryl amines with arylboronic esters. The dual role of magnesium has been elucidated: (i) the magnesium reduces the nickel salt to achieve the active species and (ii) the solid magnesium acts as co-catalyst leading to a considerable decrease on the activation energies of the different reaction steps throughout the reaction pathway.

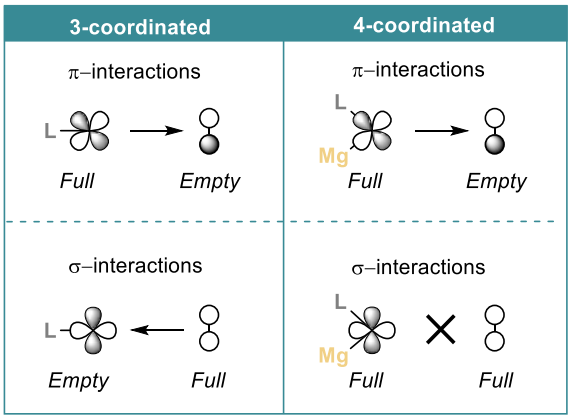

Figure 3. σ and π orbital interactions in the transition state for reductive elimination from tricoordinated complexes (left) and tetracoordinated complexes (right). [38]

Unique properties of Mg

With the full mechanistic cycle in hand and having elucidated the role of magnesium in the reaction mechanism, we wondered why the other reductants explored in the experimental studies were not capable to promote the transformation (see experimental overview). To this end, we employed the molecular volcano toolkit which, as explained in the theoretical background section, is a powerful tool to describe and predict catalytic trends by using simple descriptors.

This part of the project has been done during the short stay at the group of Prof. Clémence Corminboeuf, which was the first group to apply the concept of volcano plots (commonly employed in heterogeneous catalysis) in homogeneous systems.[39]

38 Pérez-Rodríguez, M.; Braga, A. A. C.; Garcia-Melchor, M.; Pérez-Temprano, M. H.; Casares, J. A.; Ujaque, G.; De Lera, A. R.; Álvarez, R.; Maseras, F.; Espinet, P. *J. Am. Chem. Soc.*, **2009**, 131(10), 3650–3657.

39 Busch, M.; Wodrich, M. D.; Corminboeuf, C. *Chemical Science*, **2015**, 6(12), 6754–6761.

Reductant metal clusters

To rationalize the unique properties of magnesium, we must compare it to different metals. Therefore, we have generated a volcano plot with diverse metallic surfaces, in which the nickel catalyst with the $IMes^{Me}$ ligand remains the same. To this end, we selected a set of metals to incorporate in the study; both with similar and highly different properties with respect to magnesium. This owes to the necessity of a diversity of data for the creation of proper linear scalar relationships (LSR) that represent all the chemical space.

The metals initially chosen were those colored in Figure , however, some of them (marked in red) had to be discarded due to optimization problems. It is worth mentioning that apart from the magnesium we have included other metals which were explored in the experimental work (Na, Al, Zn, Sn) and that were unable to catalyze the transformation. Those metals are used as reference as they should fall apart from the volcano plateau. In addition to the metals shown in Figure , we also incorporated three dopped clusters: (i) 6 Pt atoms and 4 Be atoms, (ii) 6 Pt atoms and 4 Si atoms and (iii) 6 Ba atoms and 4 Zn atoms. This has been done to complete the regions of the LSRs that were poorly represented. Overall, we have considered a set of 23 metallic clusters to build the volcano plot.

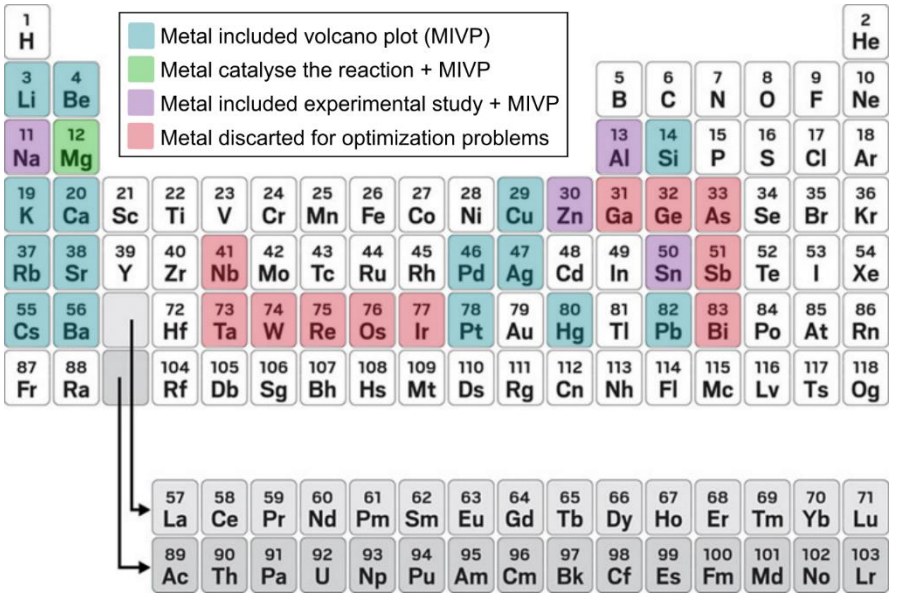

Figure 4. Collection of metals included for the construction of the volcano plot (turquoise), including magnesium (green), other reductants used in the experimental work (purple) and those discarded due to optimization problems (red).

Mechanistic elucidation for a set of selected metals

With the selected metals in hand, we proceeded with the calculation of the reaction mechanism. Notice that, as explained in the computational details section, the level of theory employed for the construction of the volcano differs from that in the mechanistic investigation. This is because the basis set used is not available for all the metals incorporated in the volcano plot.

The first problem encountered on the calculation of the reaction mechanisms with the selected set of metals is the creation of relaxed metal clusters. In the case of magnesium, we had taken the structures from a previous investigation by Panteleev *et al.*, however, this is not available for all the metals. Still, the use of a higher energy cluster will imply a systematic error in the calculations, leading to the same relative energies. Thus, for the sake of simplicity we have

followed a methodical routine in which the atoms of the magnesium cluster were substituted by the other metals and optimized at the desired level of theory.

The herein presented volcano plot has been created considering the thermodynamic picture of the mechanism and ignoring the kinetics aspects (Scheme **14** 14). This is due to the complex nature of the reaction mechanism, which would require high computation efforts to elucidate the transition states. Besides, we believe that the thermodynamic volcano will be able to reveal the main catalytic trends.

As mentioned in the previous subsection, some of the metals selected in the beginning had to be excluded due to optimization problems. Mainly those with easy access to diverse oxidation states and multiplicities which did not stick to the same mechanism elucidated for magnesium. It is important that all the systems included in the volcano proceed through the same mechanism, otherwise the LSRs will not be able to describe the system. In this context another problem arises: the **I7t** intermediate is not present in all reaction mechanisms. This is because the SET processes are not favorable for some of the metals, and in those cases both the organoboron activation and transmetalation steps occur through a Ni^{II}-Mg^{0} electron distribution. This is not a problem for the organoboron activation step, as the LSRs are consistent with different multiplicities and oxidation states, as long as the structure of the compound is the same.[40] However, those metals following a two-electron mechanism will bypass **I7t** going directly from **I6t** to **I8t**. To overcome this problem, we have excluded this intermediate in the reaction mechanism.

40 Wodrich, M. D.; Sawatlon, B.; Busch, M.; Corminboeuf, C. *ChemCatChem*, **2018**, 10(7), 1586–1591.

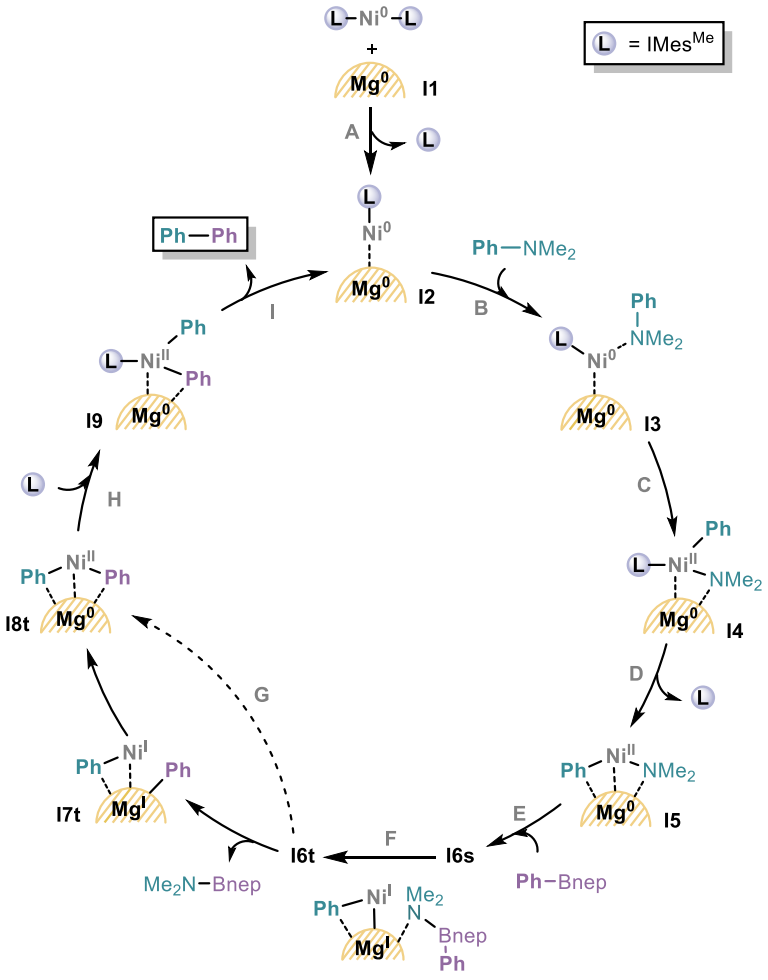

Scheme 14. Thermodynamic picture of the mechanism.

The reaction energies obtained for the mechanistic pathways for the set of 23 metallic clusters are shown in Table 5**Table 5**. We can observe large energy differences between the profiles, suggesting a strong effect of the metal properties on the reaction outcome. The specific mechanism for each metal will not be discussed on the manuscript, as the main goal of this investigation is to elucidate general trends, and this will be obtained upon the construction of the volcano plot. However, we selected the three mechanisms shown in Figure 5 (Mg, Cs and Al) as example and we will provide a brief discussion.

Table 5. Gibbs Free energies (kcal/mol) for all the computed intermediate with the set of metals included in the study.

Metal	I2	I3	I4	I5	I6s	I6t	I8t	i9
Ba	-66,1	-61,6	-85,5	-78,8	123,4	-142,0	-97,0	-99,4
Be	-15,1	-10,9	-20,8	-7,6	-28,6	-26,5	-	-2,8
Ca	-21,6	-16,4	-37,8	-26,9	-34,6	-40,3	-37,8	-48,8
Cs	30,0	23,2	21,7	0,7	0,8	-7,9	-18,6	-
K	29,1	27,1	23,6	14,3	32,0	7,2	4,8	14,9
Li	9,0	10,6	-1,9	-15,2	-20,7	-21,5	-13,6	-13,4
Na	23,6	22,1	13,6	25,3	39,9	17,9	9,3	27,8
Mg	-1,0	10,8	7,2	1,4	-15,4	-12,4	4,4	2,8
Rb	55,3	20,4	12,3	-2,0	-1,6	-9,2	-10,8	30,1
Sr	-17,8	-16,6	-32,3	-33,9	-31,8	-24,4	-42,4	63,0
Si	-19,7	-6,5	-4,7	47,6	57,9	56,9	-	18,7
Ag	15,7	-4,7	-1,8	32,2	37,8	36,4	20,0	4,5
Sn	-4,5	24,8	13,4	55,4	69,7	64,8	49,3	20,8
Al	-17,9	-4,2	10,2	41,1	10,9	15,8	11,4	3,7
Zn	-10,7	-8,5	-4,6	25,3	9,4	9,4	-0,6	-29,0
Cu	-7,8	-19,2	-16,4	0,6	0,4	-1,9	-1,5	-29,9
Hg	8,6	6,8	4,0	37,4	54,8	49,7	30,8	-1,7
Pb	-0,4	17,9	15,8	47,2	78,0	69,6	56,9	9,8
Pt	-49,8	-52,5	-58,6	13,2	7,6	-	-	-55,4
Pd	-25,9	-38,5	-43,1	1,4	17,7	6,8	-10,5	-51,1
Pt-Si	-34,8	-16,0	-30,9	16,7	-	14,1	-3,1	-45,1
Pt-Be	-17,1	-2,7	-34,3	22,3	70,8	20,1	38,2	-2,7
Ba-Zn	-14.6	-	-22.4	-22.8	-42.4	-42.9	-38.3	56.5

From a thermodynamic perspective, the ideal catalytic scenario would be composed by a series of equally exergonic reaction steps (Figure 5, A). This

would imply that under thermodynamic control, the reverse reactions are minimized, driving the system to the faster formation of the desired product. In this system, all the mechanisms are far from an ideal situation. This agrees with the challenging nature of the transformation, in which even the experimental used metal (Mg) needs 136ºC and 36h to yield the coupling product. Different phenomena are responsible of shifting the systems far from this ideal situation: the presence of energy wells in the case of Mg (for intermediates **I6s** and **I6t**), problems on the ligand exchange with the metallic cluster in the case of Cs (from **I1** to **I2**) and high laying intermediates for both Cs and Al pathways. However, no clear trends can be derived through the analysis of this or more mechanistic profiles. We need a unified picture to get a general vision of the scenario.

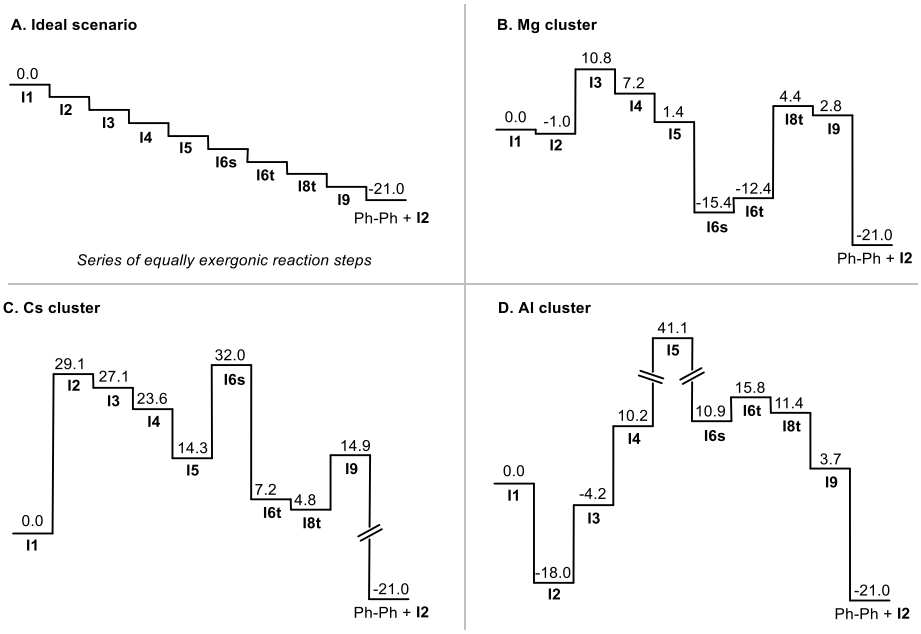

Figure 5. Ideal energy scenario for a catalytic cycle and selection of three metals (Mg, Cs, Al) mechanisms as example.

Linear scaling relationships

Once we have computed the mechanism with the different selected metals it is time to derive the LSRs. To build the scaling relationships, we proceeded with the identification of the optimal descriptor. In this work we have focused on energy-based descriptors, as they have been demonstrated to be a reliable descriptor to represent reaction mechanisms.

Unfortunately, we were unable to find a single descriptor that could reproduce the whole mechanistic profile. Instead, a combination of two descriptors; ΔG_{RRS}(**I3**) and ΔG_{RRS}(**I8t**) is required (Figure). This is due to the presence of two types of intermediates: those with the organic ligand (**I2**, **I3**, **I4** and **I9**), which will be described by ΔG_{RRS}(**I3**) and those with a naked nickel center (**I5**, **I6s**, **I6t** and **I8t**), represented by ΔG_{RRS}(**I8t**). All the intermediates present a good scaling with the corresponding descriptor, with the smaller correlation found for ΔG_{RRS}(**I9**) and ΔG_{RRS}(**I3**) (R^2=0.84). This is a reasonable value, since the methodology employed to perform the calculation does not have a high accuracy, a fact that can explain higher deviations on the scaling relations.

The correlations obtained for all the intermediates allow to reproduce their energy in terms of the corresponding descriptor, moreover, these mathematical relationships have direct chemical meaning. The slope of scaling relations has been found to follow the bond-order conservation principle. [41] Consider intermediate **I2**, which can be estimated through: ΔG_{RRS}(**I3**) - 3.0 kcal/mol, in this case, the unit slope indicates the similar bonding patterns between **I2** and **I3**. On the other hand, the *y*-intercept indicates the average energy difference between intermediates, this means, in the previous example, that **I2** lies 3.0 kcal/mol lower than **I3**. Generally, those scaling relations with large and

41 Wang, Y.; Montoya, J. H.; Tsai, C.; Ahlquist, M. S. G.; Nørskov, J. K.; Studt, F. *Catal. Lett.*, **2016**, 146(2), 304–308.

positive *y*-intercepts are associated to large thermodynamic barriers and can be used to identify potential problematic steps on the reaction mechanism. By contrast, large negative *y*-intercept are connected to favourable thermodynamic steps which can help to drive the reaction towards the completion.

A general comparison can only be made when a single descriptor is used for the whole system, as the reference will be preserved in all the scaling relations. In our case, we compare scaling relationships involving two different descriptors and we can clearly see a direct correlation between the *y*-intercept value and the descriptor used. The large negative *y*-intercept values are observed on the scaling relationships between ΔG_{RRS}(**I3**) and ΔG_{RRS}(**I4**) (-6.4 kcal/mol) and between ΔG_{RRS}(**I3**) and ΔG_{RRS}(**I9**) (-6.3 kcal/mol) and the large positive values are found on the scaling relationships between ΔG_{RRS}(**I8t**) and ΔG_{RRS}(**I5**) (9.4 kcal/mol) and between ΔG_{RRS}(**I8t**) and ΔG_{RRS}(**I6s**) (12.0 kcal/mol). These trends indicate that intermediate **I3** lies higher in energy with respect to **I8t**. In essence, the need of two different descriptors complicates the rationalization of the trends. The examination of the LSRs merely leads us to the same conclusions from the previous analysis of the specific reaction mechanisms for Mg, Al, and Cs (Figure 6): we are in front of a challenging transformation with large thermodynamic barriers.

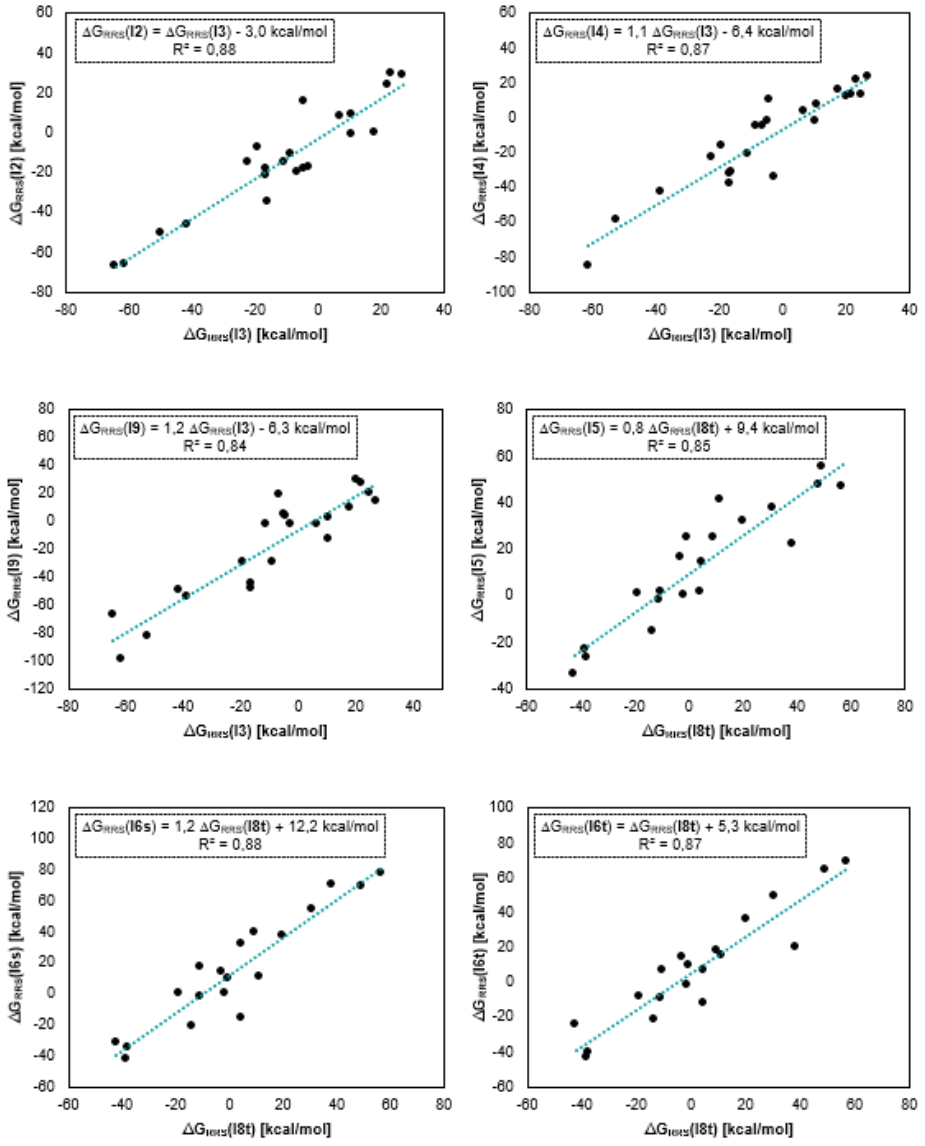

Figure 6. Scaling relations among the reaction intermediates. Two different descriptors have been employed; ΔG_{RRS}(**I3**) to represent **I2**, **I4** and **I9**, ΔG_{RRS}(**I8t**) to represent **I5**, **I6s** and **I6t**.

Construction of the volcano plot

At this point we have been able to confirm the presence of LSRs for all the intermediates in the catalytic cycle and we can now use them to derive the mathematical functions to represent the different reaction steps (labeled with letters in Scheme 14). This is done by subtracting the energy of the reactants from that of the products and then using the LSRs to express each reaction step as function of **I3** and **I8** intermediates. Upon solving the resulting equations, we obtain the mathematical description of the reaction steps (Equations 1-9). Notice that **I1** does not have any scaling relation, because it is taken as reference:

A (**I1→I2**): ΔG_{theo} (**A**) = ΔG_{RRS}(**I2**) - ΔG_{RRS}(**I1**) = ΔG_{RRS}(**I3**) - 3.03

B (**I2→I3**): ΔG_{theo} (**B**) = ΔG_{RRS}(**I3**) - ΔG_{RRS}(**I2**) = 0.01 ΔG_{RRS}(**I3**) + 3.03

C (**I3→I4**): ΔG_{theo} (**C**) = ΔG_{RRS}(**I4**) - ΔG_{RRS}(**I3**) = 0.08 ΔG_{RRS}(**I3**) - 6.39

D (**I4→I5**): ΔG_{theo} (**D**) = ΔG_{RRS}(**I5**) - ΔG_{RRS}(**I4**) = -1.08 ΔG_{RRS}(**I3**) + 0.83 ΔG_{RRS}(**I8t**) + 15.8

E (**I5→I6s**): ΔG_{theo} (**E**) = ΔG_{RRS}(**I6s**) - ΔG_{RRS}(**I5**) = 0.39 ΔG_{RRS}(**I8t**) + 2.75

F (**I6s→I6t**): ΔG_{theo} (**F**) = ΔG_{RRS}(**I6t**) - ΔG_{RRS}(**I6s**) = 0.17 ΔG_{RRS}(**I8t**) - 6.85

G (**I6t→I8t**): ΔG_{theo} (**G**) = ΔG_{RRS}(**I8t**) - ΔG_{RRS}(**I6t**) = 0.05 ΔG_{RRS}(**I8t**) - 5.32

H (**I8t→I9**): ΔG_{theo} (**H**) = ΔG_{RRS}(**I9**) - ΔG_{RRS}(**I8t**) = 1.23 ΔG_{RRS}(**I3**) - ΔG_{RRS}(**I8t**) - 6.28

I (**I9→I2**): ΔG_{theo} (**I**) = ΔG_{RRS}(**I2**) - ΔG_{RRS}(**I9**) = -0.23 ΔG_{RRS}(**I3**) -17.72

Equations 1-9 represent the energetics of all reaction steps involved in the transformation and are used to construct the volcano. The combination of two descriptors to express the system implies the construction of a 3D volcano plot where the *x* and *y* axis correspond to the ΔG_{RRS}(**I3**) and ΔG_{RRS}(**I8t**) descriptors and the *z* axis to the potential determining step, -ΔG(**pds**). Besides, the presence

of two descriptors implies that the reaction steps are represented as planes, leading to the complex picture shown in Figure 7.

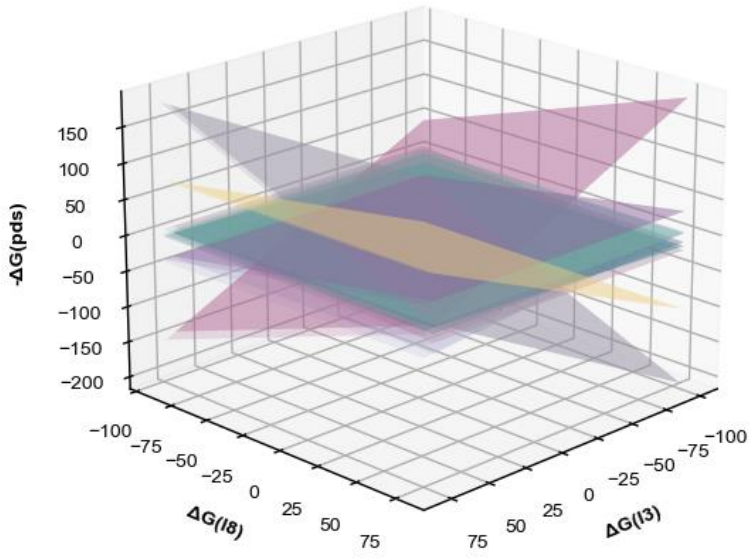

Figure 7. 3D plot obtained through the representation of LSRs of all the intermediates.

These planar surfaces are comparable the lines observed in one-dimensional volcanos, therefore, the lower laying planes (as the lower laying lines in one-dimensional volcanos died), represent the higher energy determining steps. Figure shows the relevant planes in our system, which delimitate three different regions of potential determining step (pds), corresponding to reactions **A** (yellow plane), **D** (violet plane) and **H** (purple plane).

With this picture in hand and the energetics of the different reaction mechanisms, we can locate the metals used for the construction of the volcano in the obtained plot. If we do so, the metals will not fall exactly in the planar surfaces, this is because we have employed the LSRs to represent the different reaction steps, including the computed reaction free energies in an indirect manner. The dispersion of the individual metals in the LSRs (Figure 8) is

translated into small deviations of the metal location with respect to the planar surface, *i.e.*, different positions in the *z* axis. Still, we can obtain the estimated -ΔG(**pds**) by projecting the metals to the correspondent plane and expect a higher catalytic activity from those falling in the top of the volcano. This is done by drawing a line perpendicular to the plane delimitated by the descriptors. The same process can be used to predict the catalytic activity of new metals, but in this case we would locate the catalyst in the plot just by using the two descriptors *i.e.*, *x* and *y* axis, and then we would project it (in the *z* axis) to the perpendicular plane that delimitate the pds.

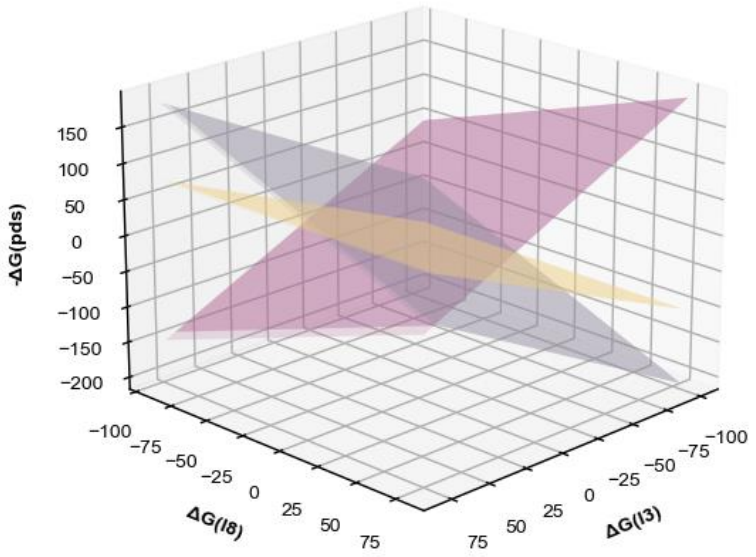

Figure 8. Relevant planes (those delimitating the pds) of the 3D plot obtained through the representation of LSRs of all the intermediates.

Even with the reduced number of planes, this representation composes a significantly complex picture of the system, therefore, before the inclusion of the metals, we will simplify the visualization. To get a more manageable picture of the volcano plot we need to reduce its dimensionality i.e., translate it into a 2D plot. This is done through the use of a color bar to represent the -ΔG(**pds**),

eventually obtaining a simple and general vision of the transformation (Figure 9).

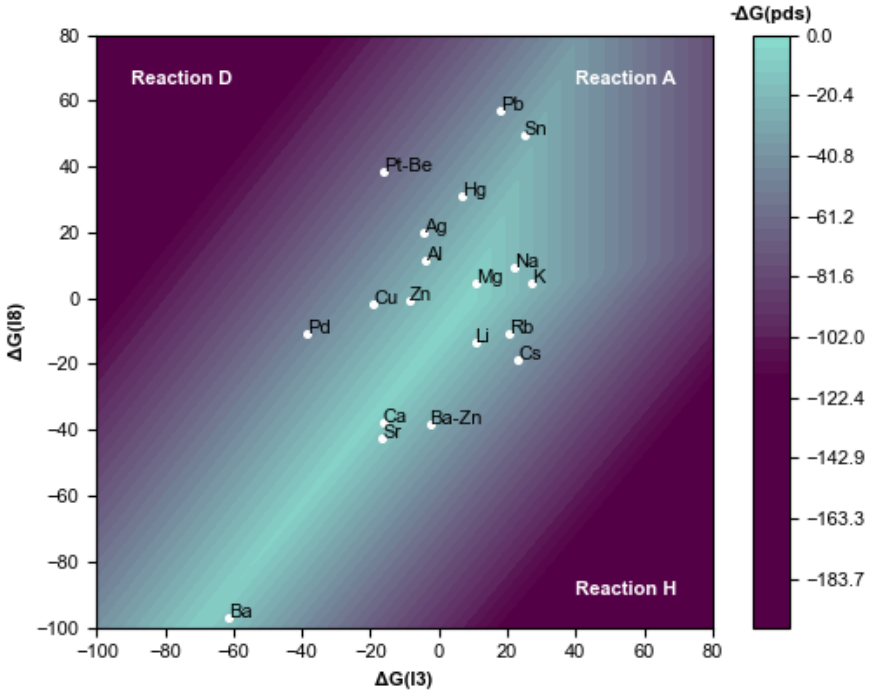

Figure 9. 2D volcano plot obtained through the representation of LSRs of all the intermediates. The plot is a simplification of the 3D by including the -ΔG(**pds**) in a colorbar.

Now, we can represent the metals as function of ΔG_{RRS}(**I3**) and ΔG_{RRS}(**I8t**) descriptors with the colour region of their position representing the value of the thermodynamical determining step. Notice that only 19 metals have been projected into the volcano plot (instead of the 23 metals used to create the LSRs), this is because for some of them (Be, Si, Pt, Pt-Si) it was not possible to compute the ΔG_{RRS}(**I8t**) descriptor. In this plot we can also observe the volcano shape: the light turquoise colour conforming the plateau of the volcano and the vertexes of the coloured triangles the intersection between the planes

which define the three regions that delimitate which reaction; **A**, **D** or **H** is the pds.

The first thing that draws the attention when we analyse the volcano plot is that Mg is the only metal that falls into the volcano plateau, this result agrees with the experimental data, where no other metals were able to promote the transformation. In fact, all the metals included in the experimental study and used to construct the volcano (Na, Zn, Al, Sn) fall far from the volcano plateau.

To understand the underlying reasons, we have to analyse the three regions of potential determining step reactions. But before it is worthwhile mentioning that if we compare the metals with the calculated energies for each intermediate, we can see that 6 out of the 19 metals included in the 2D representation fall in the wrong region (Table 6), i.e., different computed and predicted pds are obtained. This is attributed to two different situations: (i) it is the only metal with that specific determining step (such as Ba and Mg) fact that can be explained because the volcanos are a simplified visualization of the overall scenario and thus is not able to capture the exceptions and (ii) a wrong delimitation of the regions between **A** and **H** (Cs, Li, Rb) and **D** and **H** (Cs). In this case, the error is attributed to deviations on the LSRs, which combined with the high complexity of the 3D volcano can lead to small divergence on the predictions.

Table 6. Comparison of the metals for which the computed determining step (ds) does not agree with the predicted pds.

Metal	Computed pds	Predicted pds
Ba	E	H
Ca	D	H
Cs	A	H
Li	A	H
Mg	G	A
Rb	A	H

Once we have clarified this slight deviation it is time to focus on the important conclusions that can be extracted from the volcano. To this end, we examine the reactions involving the thermodynamically problematic steps (Scheme 15). All of them involve the coordination or decoordination of one of the ligands, indicating its critical role on the transformation. For reaction A, which involves the replacement of one of the ligands on the nickel centre by the metallic cluster, the system needs to present balanced interactions for the nickel centre with both the carbene ligand and the metal. In the case of an overly strong union between the ligand and the nickel, the metallic cluster will be unable to replace the ligand, impeding the reaction to proceed. For reaction D, we need a sufficiently strong interaction between the metal cluster and the nickel centre, which can compensate the decoordination of the second carbene upon the creation of a stronger interaction with the nickel. Otherwise, the ligand will not be decoordinated impeding the approach of the organoboron reagent. Finally, for reaction H, we have the opposite situation; when the interaction of the metallic cluster with the nickel is overly strong, the intermediate **I8t** becomes stable enough, and the re-coordination of the ligand becomes a hampered reaction which impedes the reductive elimination to proceed.

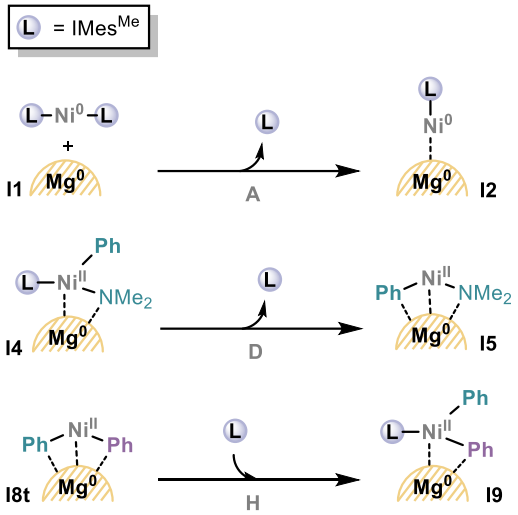

Scheme 15. Representation of the reactions involved in the potential determining steps on the volcano plot (A, D, H).

The combination of the optimal situation for reactions **A**, **D** and **H** is only found when magnesium is used to promote the transformation, converting the metal into the perfect choice. First, the ligand replacement in reaction **A** occurs through a quasi-isoenergetic step of -1.0 kcal/mol, indicating similar strengths on the interactions of the nickel with both the ligand and the magnesium cluster. Then, in reaction **D**, the second ligand is decoordinated in an exergonic manner (-5.9 kcal/mol). Lastly in reaction **H**, these balanced interactions contribute to the easy re-coordination of the ligand through a slightly thermodynamically favourable step of -1.6 kcal/mol. The construction of the 2D volcano plot has provided a general picture of the system, pointing out the key role of the ligand in the transformation. Now, we could use the volcano plot to predict the efficiency of other potential catalytic systems, not only by modifying the metal but also the ligands and identify other potential good catalysts.

Summary

The current computational study has enabled the understanding of the Ni-catalysed and Mg-facilitated combinatorial work for the Miyaura coupling of dimethyl aryl amines with arylboronic esters (Scheme 16). The mechanistic investigation shows the dual role of magnesium in the transformation; as a reductant of the $NiBr_2$ precursor to form $Ni(Mes^{Me})_2$ and as a co-catalyst in the whole transformation. First, the solid magnesium assists the decoordination of one ligand yielding the active specie **I2** in which the magnesium cluster interacts with the nickel centre. Then, the amine enters the system leading to the oxidative addition which yields the highly sterically hindered intermediate, **I4**. The system cannot evolve without the prior decoordination of the second ligand which enable the approach of the organoboron reagent. From this point, magnesium acts as an electron reservoir, enabling access to different nickel oxidation states. Both organoboron activation and transmetalation proceed *via* a SET procedure involving Ni^{I}-Mg^{I} intermediates. Finally, magnesium recovers the electron leading to a Ni^{II} intermediate that after the re-coordination of the ligand proceeds with the reductive elimination and releases the product.

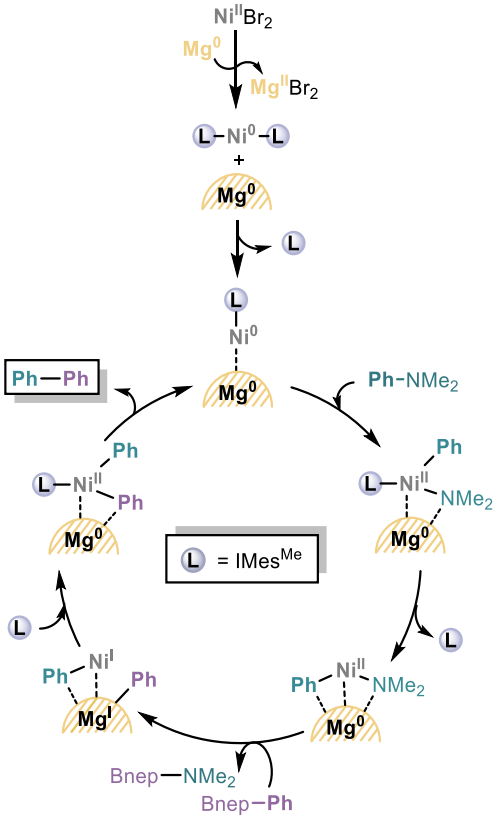

Scheme 16. Simplified catalytic cycle of the Ni-catalysed and Mg-facilitated Suzuky-Miyaura coupling of dimethyl aryl amines with arylboronic esters.

The construction of a 2D volcano plot has enabled to explain the reason behind magnesium being the perfect choice as reductant in the transformation. The co-catalyst has the perfectly balanced interactions with the nickel, which leads to the plausible coordination/decoordination of the ligand whenever is required. Our results highlight the importance of the in-depth understanding of Ni-catalysed transformations as well as its cooperation with other species such as magnesium since it may open a new playground in one-electron chemistry and set the basis for the development of novel reactivity. Besides, the combination of the mechanistic understanding with predictive tools such as the volcano plots will allow a more rapid development of the field.

General Conclusions

UNIVERSITAT ROVIRA I VIRGILI
BEYOND CONVENTIONAL DFT CATALYSIS: MECHANOCHEMISTRY AND SOLID REDUCTANTS
Bruna Sánchez Pladevall

Throughout this thesis, we have investigated three different families of systems located in the frontier between homogeneous and heterogeneous worlds. Our results demonstrate that methods emerging from computational homogeneous catalysis can be indeed applied to rationalise transformations induced through ball-milling techniques and reactions involving solid reductants. Moreover, we have demonstrated the importance of microkinetic modelling to provide a full understanding of these transformations. The following paragraphs outline the most relevant conclusions for each chapter.

In *Chapter I* we have developed a methodology to model ball milling reactions through the combination of standard DFT tools and microkinetic modelling. The key considerations of our strategy are: (*i*) the use of a specific dielectric environment computed through the mixture of all the species in the reaction media, (*ii*) the introduction of a mechanochemical concentration, which is approximated from the density of the reagents, and (*iii*) the consideration of local jar effects associated to temperature gradients originated in the milling jar during the reaction.

In *Chapter II* we have elucidated the full mechanistic picture of the Ni-catalysed reductive coupling of aryl halides with monofluoroalkyl halides and demonstrated the imperative need of microkinetic modelling to critically analyse the computed reaction profile. Indeed, its application is central to the determination of the origin of selectivity which is associated to metal-free steps of substrate radical trapping, in a mechanism very different from classical cross-coupling.

In *Chapter III* we have revealed the reaction mechanism for the Ni-catalysed and Mg-facilitated cross-coupling of dimethyl aryl amines with arylboronic esters and clarified the specific role of the reductant in the transformation. The magnesium is shown to play multiple roles: (i) it reduces the nickel catalyst to form the active species, (ii) it enables a facile coordination/decoordination of

the ligand due to perfectly balanced interactions with the nickel centre, (iii) it assists the oxidative addition process and (iv) it facilitates the transmetalation step enabling a single electron pathway through Ni(I) species.

UNIVERSITAT ROVIRA I VIRGILI
BEYOND CONVENTIONAL DFT CATALYSIS: MECHANOCHEMISTRY AND SOLID REDUCTANTS
Bruna Sánchez Pladevall

UNIVERSITAT ROVIRA I VIRGILI
BEYOND CONVENTIONAL DFT CATALYSIS: MECHANOCHEMISTRY AND SOLID REDUCTANTS
Bruna Sánchez Pladevall

UNIVERSITAT ROVIRA I VIRGILI
BEYOND CONVENTIONAL DFT CATALYSIS: MECHANOCHEMISTRY AND SOLID REDUCTANTS
Bruna Sánchez Pladevall

UNIVERSITAT ROVIRA I VIRGILI
BEYOND CONVENTIONAL DFT CATALYSIS: MECHANOCHEMISTRY AND SOLID REDUCTANTS
Bruna Sánchez Pladevall

UNIVERSITAT
ROVIRA i VIRGILI